Signal Approximation using the Bilinear Transform

by

Archana Venkataraman

Submitted to the Department of Electrical Engineering and Computer Science
in partial fulfillment of the requirements for the degree of

Masters of Engineering in Electrical Engineering and Computer Science

at the

MASSACHUSETTS INSTITUTE OF TECHNOLOGY

August 2007

© Archana Venkataraman, MMVII. All rights reserved.

The author hereby grants to MIT permission to reproduce and distribute publicly
paper and electronic copies of this thesis document in whole or in part.

Author . . . .
Department of Electrical Engineering and Computer Science
August 10, 2007

Certified by . . . .
Alan V. Oppenheim
MacVicar Faculty Fellow, Ford Professor of Engineering
Department of Electrical Engineering and Computer Science
Thesis Supervisor

Accepted by . . . .
Arthur C. Smith
Professor of Electrical Engineering
Chairman, Department Committee on Graduate Theses

Signal Approximation using the Bilinear Transform

by

Archana Venkataraman

Abstract

This thesis explores the approximation properties of a unique basis expansion. The expansion implements a nonlinear frequency warping between a continuous-time signal and its discrete-time representation according to the bilinear transform. Since there is a one-to-one mapping between the continuous-time and discrete-time frequency axes, the bilinear representation avoids any frequency aliasing distortions.

We devote the first portion of this thesis to some theoretical properties of the bilinear representation, including the analysis and synthesis networks as well as bounds on the basis functions. These properties are crucial when we further analyze the bilinear approximation performance. We also consider a modified version of the bilinear representation in which the continuous-time signal is segmented using a short-duration window. This segmentation procedure affords greater time resolution and, in certain cases, improves the overall approximation quality.

In the second portion of this thesis, we evaluate the approximation performance of the bilinear representation in two different applications. The first is approximating instrumental music. We compare the bilinear representation to a discrete cosine transform based approximation technique. The second application is computing the inner product of two continuous-time signals for a binary detection problem. In this case, we compare the bilinear representation with Nyquist sampling.

Thesis Supervisor: Alan V. Oppenheim
Title: MacVicar Faculty Fellow, Ford Professor of Engineering
Department of Electrical Engineering and Computer Science

Acknowledgments

I am greatly indebted to my research advisor, Professor Alan Oppenheim. His devotion to and concern for students is unparalleled by anyone else I have come across. He has continually pushed me to achieve my full potential, but at the same time, he has remained a friendly and supportive mentor. His comments and ideas have helped to expand and enrich my thesis work, and his patience and encouragement have made my first year in graduate school an extremely positive one.

I would also like to thank Professor Vivek Goyal, head of the Signal Transformation and Information Representation group at MIT. Not only was his class (Wavelets, Approximation and Compression) instrumental in shaping my final MEng thesis, but his friendly one-on-one discussions have been invaluable to my research work and experience.

I would like to acknowledge past and present members of the Digital Signal Processing Group (DSPG): Tom Baran, Petros Boufounos, Sourav Dey, Zahi Karam, Al Kharbouch, Jon Paul Kitchens, Joonsung Lee, Charlie Rohrs, Melanie Rudoy, Joe Sikora, Eric Strattman, Dennis Wei and Matthew Willsey. Over the past two years, these individuals have sustained an exciting, collaborative and friendly research environment in which I could continually challenge myself and broaden my horizons. I would especially like to thank Tom and Sourav for their insightful conversations, Melanie for always being there when I needed someone to chat with, Zahi for keeping my temper well-honed while somehow managing to make me smile, and lastly, Eric for running the DSPG office smoothly and efficiently.

A special thanks to Austin Che, who has been my personal LaTex guru for the the past three months. Without his help this document would have been infinitely more daunting and tedious to compile. Thank you, also, for being my shoulder to lean on through all the hard times here at MIT.

Finally, to my family: thank you for your love and support all these years. You were the ones who first nurtured my curiosity and desire to learn. Your encouragement has played a major role in all of my successes. At the same time, you have stood besides me through all the turmoil and trials of my life thus far. Words cannot adequately express all that I owe you, and I hope that one day, I can repay at least a fraction of all you have done for me.

To my family

Contents

List of Figures

List of Tables

Chapter 1

Introduction

Recent technological advancements have allowed for a rapid growth in the speed and capabilities of digital processors. These improvements have made it easier, and often more efficient, to perform many signal processing operations in the digital domain. However, much of the valuable real-world information encountered remains analog or continuous-time in nature.

1.1 Signal Representation Using Basis Expansions

We can circumvent the above dilemma by representing a continuous-time (CT) signal $f(t)$ using a basis expansion as follows:

$$f(t) = \sum_{n=-\infty}^{\infty} f[n]\psi_n(t) \tag{1.1}$$

The set of functions $\{\psi_n(t)\}_{n=-\infty}^{\infty}$ is a countable set of basis functions and the coefficients $f[n]$ are the expansion coefficients with respect to a chosen basis.

Since the basis functions are known *a priori*, the CT signal $f(t)$ is completely specified by the discrete-time (DT) sequence of expansion coefficients $f[n]$. Therefore, it can now be manipulated using DT operations.

We assume that the reader is familiar with the following concepts related to basis expansions, as they will be referenced throughout the remainder of this thesis:

We refer to analysis as the process of computing the expansion coefficients from the original continuous-time signal and the given set of basis functions. Similarly, we refer

to synthesis as the process of reconstructing a continuous-time signal from its expansion coefficients according to Equation (1.1).

Additionally, we define the standard inner product, in continuous and discrete time, as

$$\langle f, g \rangle_c \;=\; \int_{-\infty}^{\infty} f(t)g(t)dt \tag{1.2}$$

$$\langle f, g \rangle_d \;=\; \sum_{n=-\infty}^{\infty} f[n]g[n] \tag{1.3}$$

We consider two signals to be orthogonal if their standard inner product is zero, and we shall denote the signal energy as the standard inner product of a signal with itself.

In the following subsections we introduce two commonly-used types of basis expansions; specifically the orthonormal and the biorthogonal signal representations. We assume that all signals and all sequences have finite energy and are real-valued.

1.1.1 Properties of an Orthonormal Signal Representation

In an orthonormal expansion, the set of basis functions $\{\lambda_n(t)\}_{n=-\infty}^{\infty}$ are chosen to satisfy the condition

$$\langle \lambda_n, \lambda_m \rangle_c = \begin{cases} 1, & n = m \\ 0, & \text{otherwise} \end{cases} \tag{1.4}$$

In particular, Equation (1.4) indicates that the basis functions are mutually orthogonal to each other and have unit energy.

One advantage of an orthonormal representation is that the expansion coefficients can be obtained via an inner product with the respective basis function. Mathematically, if $f(t) = \sum_m f[m]\lambda_m(t)$, then it follows from Equation (1.4) that

$$\langle f, \lambda_n \rangle_c = \sum_m f[m]\langle \lambda_m, \lambda_n \rangle_c = f[n] \tag{1.5}$$

An orthonormal representation will also preserve the standard inner product between continuous time and discrete time. Namely, if $f(t) = \sum_n f[n]\lambda_n(t)$ and $g(t) = \sum_n g[n]\lambda_n(t)$, then we have

$$\langle f, g \rangle_c = \langle f, g \rangle_d \tag{1.6}$$

The above property is extremely useful in our consideration of matched filtering applications

16

since we can compute the inner product of two CT signals as the inner product of their expansion coefficient sequences.

1.1.2 Properties of a Biorthogonal Signal Representation

In a biorthogonal expansion, the continuous-time signal is represented as

$$f(t) = \sum_{n=-\infty}^{\infty} f[n]\phi_n(t) \tag{1.7}$$

For convenience, we refer to the set of functions $\{\phi_n(t)\}_{n=-\infty}^{\infty}$ as the primal basis. Once again $f[n]$ is the associated sequence of expansion coefficients.

The difference here is that we no longer constrain the primal basis functions $\phi_n(t)$ to be orthogonal. Instead, we define a dual basis $\{h_n(t)\}_{n=-\infty}^{\infty}$, which satisfies the condition:

$$\langle h_n(t), \phi_m(t) \rangle = \begin{cases} 1, & n = m \\ 0, & \text{otherwise} \end{cases} \tag{1.8}$$

The combined set of functions $\{\phi_n(t), h_n(t)\}_{n=-\infty}^{\infty}$ now constitutes a biorthogonal signal representation.

There are some key differences between an orthonormal and a biorthogonal expansion, which will have direct implications on the applications we consider. First, since the basis functions $\phi_n(t)$ are not necessarily orthogonal, the expansion coefficients $f[n]$ cannot be computed according to Equation (1.5). Rather, we use an inner product with the dual basis functions $h_n(t)$. Mathematically, if $f(t) = \sum_m f[m]\phi_m(t)$, then

$$\langle f, h_n \rangle_c = \sum_m f[m]\langle \phi_m, h_n \rangle_c = f[n] \tag{1.9}$$

A potential problem with a biorthogonal representation is that it may be extremely difficult to find and/or manipulate the dual basis.

A second consequence of the basis functions not being orthonormal is that the standard inner product of two CT signals is no longer equal to the standard inner product of their DT expansion coefficient sequences. Depending on the specific representation, it may be fairly complicated to compute the expression in Equation (1.2).

Although these differences add a degree of complexity to implementing a biorthogonal

expansion, relaxing the orthonormality constraint allows for a much broader class of signal representations. This opens the door to other desirable properties, which cannot be achieved using an orthonormal expansion.

1.2 The Necessity for Signal Approximation

One major drawback to using a basis expansion given in Equation (1.1) is that most typical CT signals will have an infinite number of non-zero expansion coefficients. However, due to practical limitations such as processing time and hardware capability, we are restricted to only a finite number of DT values.

If the basis functions remain unchanged, it is necessary to find a suitable approximation to the original signal of the form

$$\hat{f}(t) = \sum_{n \in I_M} \hat{f}[n] \psi_n(t) \tag{1.10}$$

In Equation (1.10) I_M represents a finite set of indices and $\hat{f}[n]$ is the modified expansion coefficient sequence.

Unlike the case of perfect representation in Equation (1.1), the quality of the approximation $\hat{f}(t)$ is heavily dependent on the original signal, the set of basis functions, and the particular application.

1.3 Signal Representation using the Bilinear Transform

This thesis is devoted to a specific basis expansion which maps the continuous-time S-plane onto the discrete-time Z-plane according to the bilinear transform relationship shown in Equation (1.11)

$$z = \frac{a + s}{a - s} \tag{1.11}$$

By substituting $z = e^{j\Omega}$ and $s = j\omega$ into Equation (1.11), we see that the $j\omega$-axis (continuous time) is mapped onto the unit circle (discrete time). Furthermore, the CT and DT frequency variables (lowercase ω and uppercase Ω respectively) are related through the inverse tangent warping

$$\Omega = 2 \tan^{-1} \left(\frac{\omega}{a} \right) \tag{1.12}$$

Effectively, the bilinear transform maps the entire range of continuous-time frequencies onto the entire range of unique discrete-time frequencies. Since there is a one-to-one relationship between the CT and DT frequency axes, this representation avoids frequency aliasing distortions.

As we shall see, there exists both an orthonormal and a biorthogonal signal representation which achieve the desired frequency warping of Equation (1.12). In the remainder of this thesis, we characterize the theoretical properties of these bilinear representations, focusing on their relevance to signal approximation. We then evaluate the bilinear approximation performance in an audio approximation and a binary detection application.

1.4   Thesis Organization

In Chapter 2 we introduce the orthonormal and the biorthogonal bilinear signal representations. We present the basis functions as well as the analysis and synthesis networks based on a cascade of first-order analog systems. Chapter 3 examines important theoretical properties of each representation, including a signal-space characterization and bounds on the various basis functions. These are useful when analyzing the approximation properties.

In Chapter 4 we summarize the approximations used to simulate CT processing in MATLAB, including limitations to both the analysis and the synthesis methods. Chapter 5 explores the bilinear approximation properties, including how they depend on the parameter a in Equations (1.11) and (1.12) as well as characteristics of signals which are well-approximated using the bilinear basis functions.

Chapter 6 introduces the Windowed Bilinear Representations in which the original CT signal is segmented using a short-duration window. This representation affords greater time resolution and, in certain cases, improves the overall approximation performance.

Chapter 7 presents simulation results when the orthonormal bilinear representation is used to approximate instrumental music. A discrete cosine transform based representation is used as a comparison metric.

Chapters 8 and 9 focus on using the bilinear representations to compute the standard inner product of two CT signals for a binary detection problem. In Chapter 8 a theoretical analysis is done for each representation and Chapter 9 presents the simulation results. The bilinear expansions are compared with a Nyquist sampling based approach.

19

Chapter 2

The Bilinear Signal Representations

This chapter introduces background material for two signal representations which implement a bilinear frequency warping between continuous and discrete time. Section 2.1 is devoted to an orthonormal expansion while Section 2.2 focuses on the biorthogonal expansion. Although much of the material is drawn from [12] and [8], the relevant expressions and derivations are included for completeness.

2.1   The Orthonormal Bilinear Signal Representation

Let $F_c(s)$ represent the Laplace transform of the CT signal $f(t)$, and let $F_d(z)$ represent the Z-transform of its DT expansion coefficient sequence $f[n]$. By extrapolating from the ideas presented in [12] and [8], we consider the following frequency-domain relationship:

$$F_d(z) = \frac{\sqrt{2a}}{z+1} F_c \left(a \frac{z-1}{z+1} \right) \tag{2.1}$$

Since the CT variable s has been replaced by the expression $\left[a \left(\frac{z-1}{z+1} \right) \right]$, Equation (2.1) is consisted with the bilinear transform relationship of Equation (1.11).

We can represent the right-hand sides of Equations (1.2) and (1.3) in the Laplace transform and Z-transform domains, respectively. Then, by making the substitution of variables $s = a \left(\frac{z-1}{z+1} \right)$ into the Laplace transform version of Equation (1.2), it follows that a continuous-time to discrete-time relationship based on Equation (2.1) preserves the stan-

dard inner product between continuous and discrete time. This implies that the resulting expansion is an orthonormal signal representation.

2.1.1 The Orthonormal Basis Functions

Similar to the technique employed in [12], the basis functions $\lambda_n(t)$ can be obtained by substituting Equation (2.1) into the inverse Z-transform of $F_d(z)$. Mathematically, this is shown below:

$$
\begin{aligned}
f[n] &= \frac{1}{2\pi j} \oint_{|z|=1} F_d(z) z^n \frac{dz}{z} \\
&= \frac{1}{2\pi j} \oint_{|z|=1} \frac{\sqrt{2a}}{z+1} F_c\left(a\frac{z-1}{z+1}\right) z^n \frac{dz}{z} \\
&= \frac{1}{2\pi j} \int_{-j\infty}^{j\infty} F_c(s) \frac{\sqrt{2a}}{a+s}\left(\frac{a+s}{a-s}\right)^n ds
\end{aligned}
\tag{2.2}
$$

Using the relationship $\int_{-\infty}^{\infty} f(t)g(t)dt = \frac{1}{2\pi j}\int_{-j\infty}^{j\infty} F_c(s)G_c(-s)ds$, we can identify the Laplace transform of the basis functions as

$$
\Lambda_n(s) = \frac{\sqrt{2a}}{a-s}\left(\frac{a-s}{a+s}\right)^n
\tag{2.3}
$$

As given in [12], the time-domain expression for $\lambda_n(t)$ is

$$
\lambda_n(t) = \begin{cases} \sqrt{2a}(-1)^{n-1}e^{-at}L_{n-1}(2at)u(t), & \text{for } n \geq 1 \\ \sqrt{2a}(-1)^{-n}e^{at}L_{-n}(-2at)u(-t), & \text{for } n \leq 0 \end{cases}
\tag{2.4}
$$

where $L_n(x)$ is a zero-order Laguerre polynomial.

Note that Equation (2.4) is parameterized by both the index value n and the value of the parameter a. Figures (2-1) and (2-2) illustrate the relationship between the basis function behavior and each of the above variables.

2.1.2 Analysis and Synthesis Networks for the Orthonormal Expansion

For simplicity, in this section we present the analysis and synthesis networks appropriate for causal continuous-time signals. Similar networks for anti-causal signals are derived in Appendix B.

According to Equation (2.4), the basis functions are anti-causal for $n \leq 0$. This implies
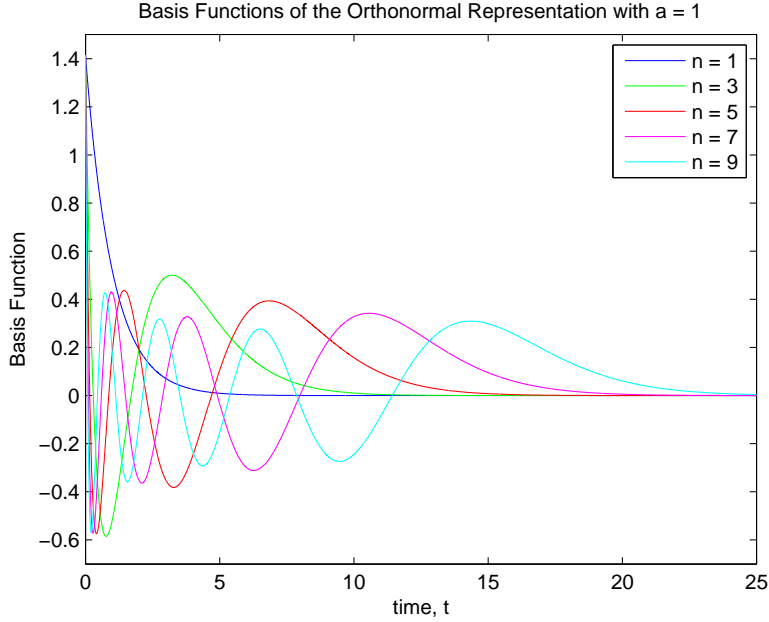
Figure 2-1: $\lambda_n(t)$ for different index values using $a = 1$

that $\langle f, \lambda_n \rangle_c = f[n] = 0 \ \forall n \leq 0$. Thus, for causal $f(t)$, we will use only the positive-indexed basis functions $\lambda_n(t)$.

We can construct an analysis and a synthesis network for this representation by exploiting a recursive relationship satisfied by the Laplace transforms $\Lambda_n(s)$. Specifically, $\Lambda_n(s)$ can be expressed in terms of $\Lambda_{n-1}(s)$ according to

$$\Lambda_n(s) = \left[\frac{a-s}{a+s} \right] \Lambda_{n-1}(s), \quad \text{for } n \geq 2 \tag{2.5}$$

where

$$\Lambda_1(s) = \frac{\sqrt{2a}}{a+s} \tag{2.6}$$

Since $f[n]$ is obtained via the inner product $\langle f, \lambda_n \rangle_c$, the bilinear coefficients can be computed using a cascade of first-order analog filters. The analysis network, similar to the one first presented in [8], is depicted in Figure (2-3). The expansion coefficients are obtained by sampling the output of each stage at time $t = 0$. Note that since a convolution is being used to compute an inner product, the input is the time-reversed signal $f(-t)$.

In addition, as seen from Equation (2.5), we can obtain successive basis functions by exciting the first-order cascade shown in Figure (2-3) with a Dirac delta function, $\delta(t)$.

23
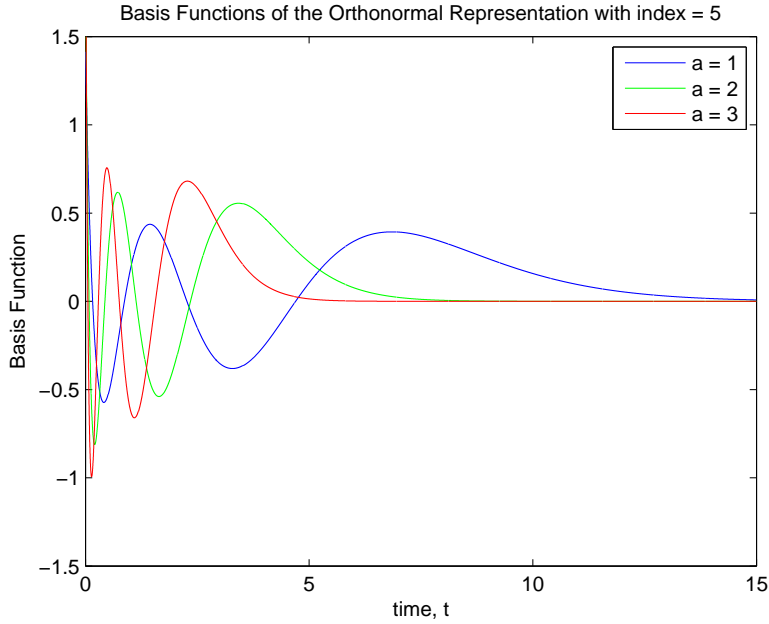
Figure 2-2: $\lambda_n(t)$ for different values of a using $n = 5$
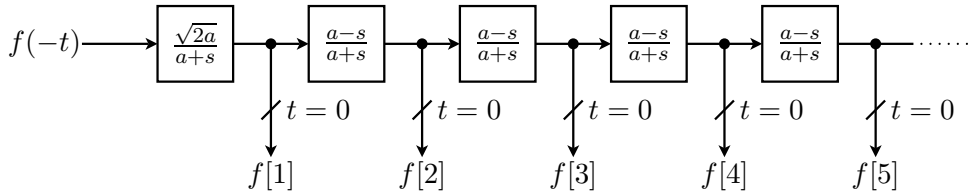
Figure 2-3: Orthonormal analysis network to compute the expansion coefficients.

To reconstruct a CT signal, the basis functions are scaled by the corresponding expansion coefficient, and the result is summed. This synthesis network, similar to the one first presented in [8], is shown in Figure (2-4).

2.2 The Biorthogonal Bilinear Signal Representation

Linear time-invariant (LTI) filtering in continuous time and linear shift-invariant (LSI) filtering in discrete time are cornerstones of many signal processing applications. By relaxing the orthonormality constraint, a biorthogonal bilinear expansion which maps a continuous-time LTI system onto a discrete-time LSI system was developed in [8]. This section provides an overview of the representation.
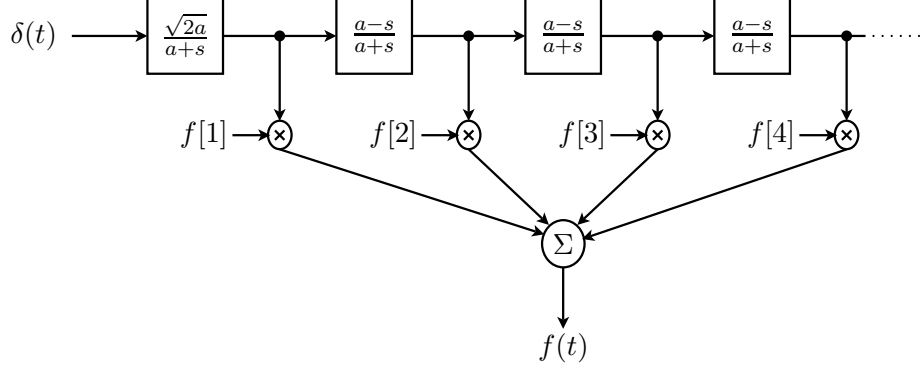
Figure 2-4: Orthonormal synthesis network to reconstruct a continuous-time signal from its bilinear expansion coefficients.

2.2.1 The Primal and Dual Basis Functions

It is shown in [8] that a necessary and sufficient condition to achieve the LTI→LSI mapping is that the Laplace transforms of the primal basis functions have the following form:

$$\Phi_n(s) = [\Phi_1(s)]^n \tag{2.7}$$

Moreover, the CT and DT complex frequency variables (s and z respectively) are related by the function $\Phi_1(s)$ as follows:

$$z^{-1} = \Phi_1(s) \tag{2.8}$$

Given the bilinear transform relationship in Equation (1.11), we identify the primal basis $\Phi_n(s) = \left(\frac{a-s}{a+s}\right)^n$. As given in [8], the time-domain expression for $\phi_n(t)$ is

$$\phi_n(t) = \begin{cases} 2a(-1)^{n-1}e^{-at}L_{n-1}^{(1)}(2at)u(t) + (-1)^n\delta(t), & \text{for } n > 0 \\ \delta(t), & \text{for } n = 0 \\ 2a(-1)^{n-1}e^{at}L_{-n-1}^{(1)}(-2at)u(-t) + (-1)^n\delta(t), & \text{for } n < 0 \end{cases} \tag{2.9}$$

where $L_{n-1}^{(1)}(x) = -\frac{d}{dx}L_n(x)$ is a first-order Laguerre polynomial.

We obtain the dual basis functions by noting that $\{\phi_n(t)\}_{n=-\infty}^{\infty}$ satisfies the following weighted orthogonality condition:

$$\int_{-\infty}^{\infty} t\phi_n(t)\phi_m(t)dt = \begin{cases} n, & n = m \\ 0, & \text{otherwise} \end{cases} \tag{2.10}$$

25

Thus for $n \neq 0$, the dual basis functions are $h_n(t) = \frac{1}{n} t \phi_n(t)$.

The impulse response $h_0(t)$ is derived in [8] by constraining the CT signal $f(t)$ to be causal and bounded. The dual basis functions are then given by the following rational Laplace transform expressions:

$$H_n(s) = \begin{cases} \frac{1}{a+s}, & \text{for } n = 0 \\ \frac{2a}{(a+s)^2} \left(\frac{a-s}{a+s} \right)^{n-1}, & \text{for } n > 0 \end{cases} \qquad (2.11)$$

Figures (2-5) and (2-6) show plots of the primal basis functions (minus the impulse at the origin) as the index and the value of a change, respectively. Figures (2-7) and (2-8) depict the same relationships for the dual basis functions.
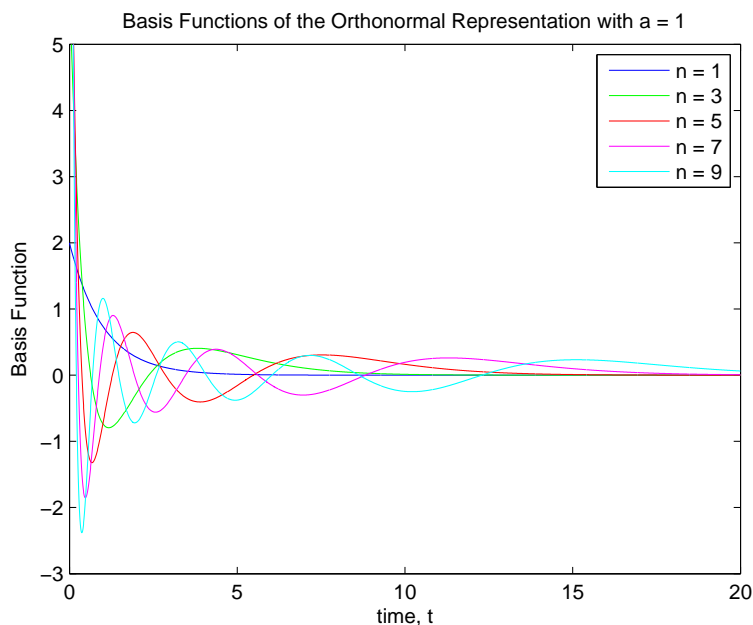
Figure 2-5: $\phi_n(t)$ for different index values using $a = 1$

2.2.2 Analysis and Synthesis Networks for the Biorthogonal Expansion

Once again we present the analysis and synthesis networks for causal continuous-time signals. The networks for anti-causal signals are derived in Appendix B.

From Equation (2.11), the dual basis functions satisfy a recursive relationship similar to Equation (2.5). Therefore, we can compute the sequence $f[n]$ using a cascade of first-order systems as shown in Figure (2-9). Again, the network input is the time-reversed signal

26
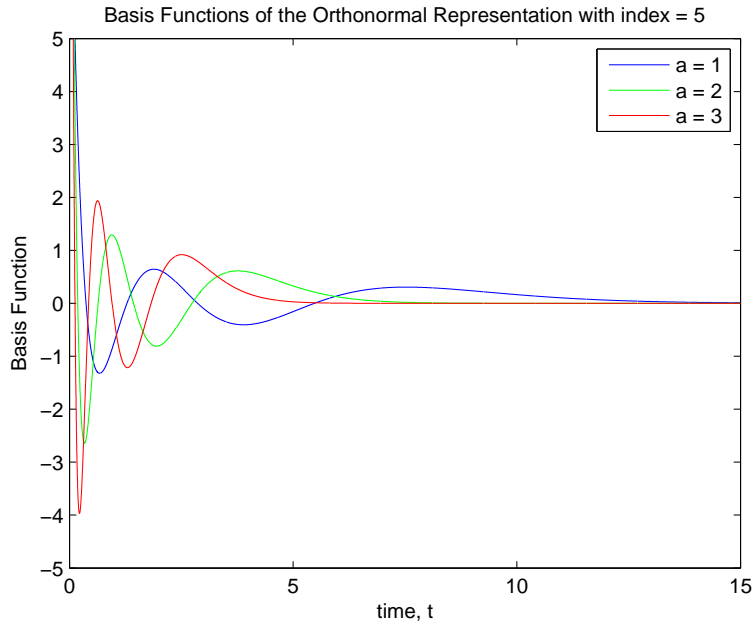
Figure 2-6: $\phi_n(t)$ for different values of a using $n = 5$

$f(-t)$, and the outputs along the chain are sampled at time $t = 0$ to obtain successive expansion coefficients.

We reconstruct the CT signal using the primal basis functions $\Phi_n(s)$. Since these functions also have a recursive structure, the synthesis network is similar to that of the orthonormal representation, as depicted in Figure (2-10).
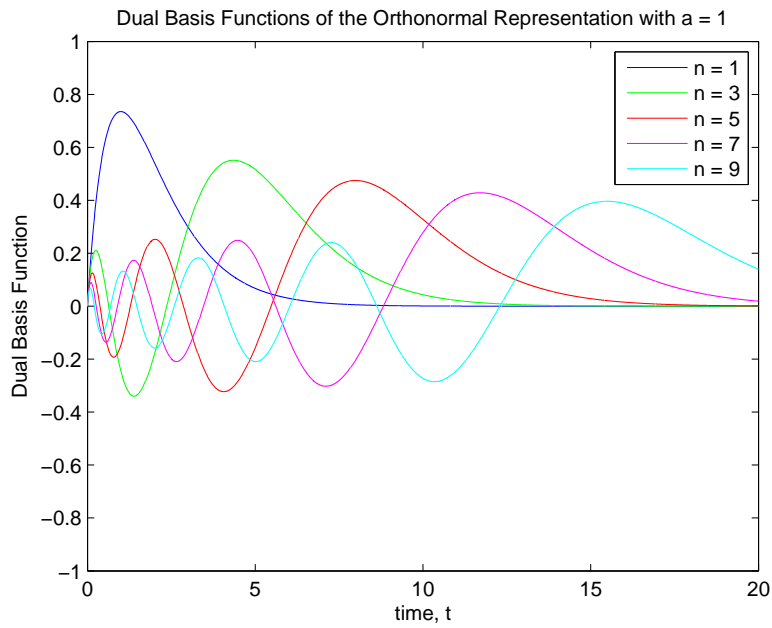
Figure 2-7: $h_n(t)$ for different index values using $a = 1$
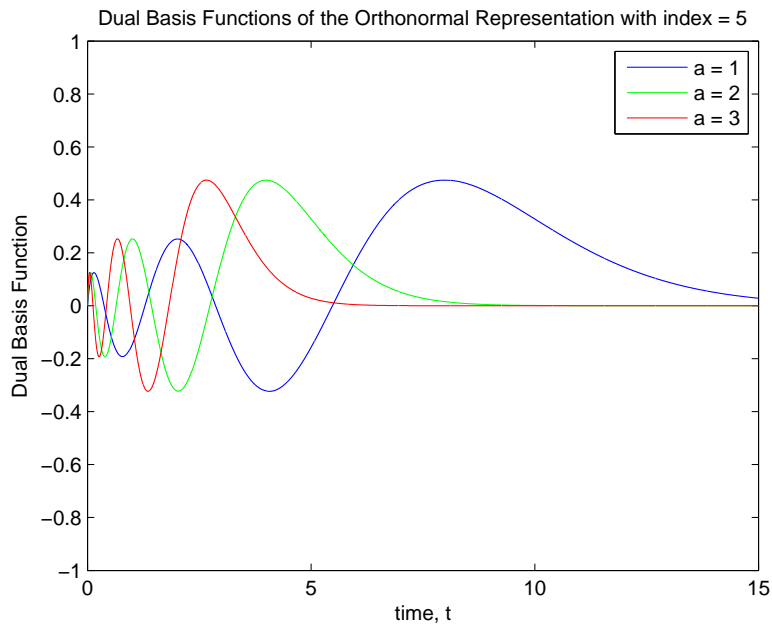
Figure 2-8: $h_n(t)$ for different values of a using $n = 5$

$f(-t) \longrightarrow \boxed{\frac{1}{a+s}} \longrightarrow \boxed{\frac{2a}{a+s}} \longrightarrow \boxed{\frac{a-s}{a+s}} \longrightarrow \boxed{\frac{a-s}{a+s}} \longrightarrow \boxed{\frac{a-s}{a+s}} \longrightarrow \cdots$

$t = 0 \qquad t = 0 \qquad t = 0 \qquad t = 0 \qquad t = 0$

$f[0] \qquad f[1] \qquad f[2] \qquad f[3] \qquad f[4]$
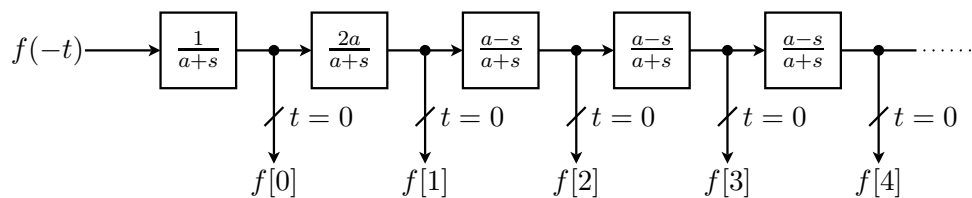
Figure 2-9: Biorthogonal analysis network to compute the bilinear expansion coefficients.

$\delta(t) \longrightarrow \boxed{1} \longrightarrow \boxed{\frac{a-s}{a+s}} \longrightarrow \boxed{\frac{a-s}{a+s}} \longrightarrow \boxed{\frac{a-s}{a+s}} \longrightarrow \cdots$

$f[0] \to \otimes \qquad f[1] \to \otimes \qquad f[2] \to \otimes \qquad f[3] \to \otimes$

Σ

$f(t)$
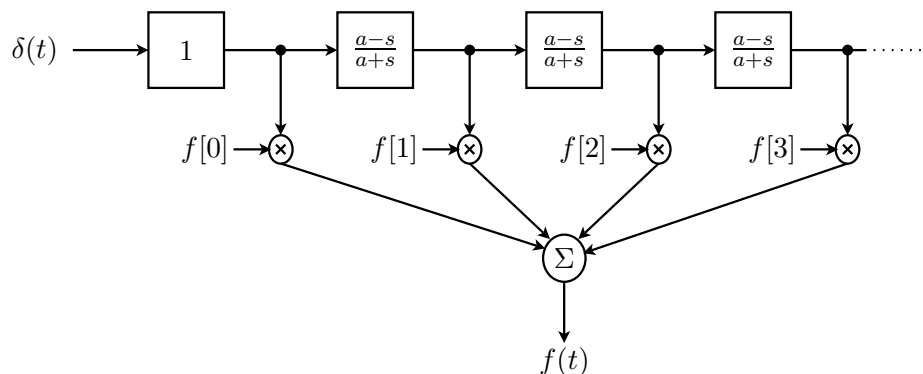
Figure 2-10: Biorthogonal synthesis network to reconstruct a continuous-time signal from its bilinear expansion coefficients.

Chapter 3

Properties of the Bilinear Signal Representations

In this chapter we derive some key properties of the two bilinear expansions. These will be useful in understanding the approximation behavior of these representations. Since this thesis concentrates on real-valued, causal and bounded CT signals, we specialize our analysis to the subset of orthonormal basis functions $\{\lambda_n(t)\}_{n=1}^{\infty}$ and the subset of primal/dual biorthogonal basis functions $\{\phi_n(t), h_n(t)\}_{n=0}^{\infty}$.

Section 3.1 focuses on properties of the orthonormal expansion, and Section 3.2 covers the biorthogonal expansion. Much of the information in this chapter is drawn from properties of the generalized Laguerre polynomials. These can be found in Appendix A. Finally, additional properties of the bilinear representations, including a preliminary noise analysis of the first-order cascades, can be found in Appendix B.

3.1 The Orthonormal Representation

In this section, we present two important properties of the orthonormal bilinear signal representation, specifically a characterization of the orthonormal signal space and bounds on the orthonormal basis functions, $\lambda_n(t)$.

3.1.1 Orthonormal Signal Space

As stated in Chapter 2, the orthonormal representation preserves the standard inner product between continuous and discrete time. This implies the following energy relationship:

$$\int_0^\infty f^2(t)dt = \sum_{n=1}^\infty f^2[n] \tag{3.1}$$

By considering the M-term approximation $\hat{f}_M(t) = \sum_{n=1}^M f[n]\lambda_n(t)$, it follows from Equation (3.1) that the energy of the error $e_M(t) = f(t) - \hat{f}_M(t)$ is

$$\begin{aligned}
\int_0^\infty e_M^2(t)dt &= \sum_{n=M+1}^\infty f^2[n] \\
&= \int_0^\infty f^2(t)dt - \sum_{n=1}^M f^2[n]
\end{aligned} \tag{3.2}$$

Since the first term in the right-hand side of Equation (3.2) is finite and $f^2[n]$ is always non-negative, as $M \to \infty$ the energy of the error goes to zero. Thus the set of orthonormal basis functions $\{\lambda_n(t)\}_{n=0}^\infty$ spans the space of causal, finite energy signals. We shall denote this signal space as $L_2(0,\infty)$.

3.1.2 Bounding the Basis Functions

From Equation (2.4) the expression for $\lambda_n(t)$, $n > 0$ is

$$\lambda_n(t) = \sqrt{2a}(-1)^{n-1}e^{-at}L_{n-1}(2at)u(t) \tag{3.3}$$

As developed in Appendix A, we can rewrite Equation (3.3) in terms of the normalized zero-order Laguerre polynomial with argument $x = 2at$.

$$\lambda_n(t) = \sqrt{2a}(-1)^{n-1}\zeta_{n-1}(2at) \tag{3.4}$$

By applying Equation (A.7) and using $\nu = 4(n-1) - 2 = 4n - 6$, we can bound the

normalized Laguerre polynomial $\zeta_{n-1}(2at)$ according to:

$$|\zeta_{n-1}(2at)| \leq C \begin{cases} 1, & 0 \leq t \leq \frac{1}{2a(4n-6)} \\ (2at(4n-6))^{-1/4}, & \frac{1}{2a(4n-6)} \leq t \leq \frac{2n-3}{2a} \\ (4n-6)^{-1/4}\left[(4n-6)^{1/3} + |4n-6-2at|\right]^{-1/4}, & \frac{2n-3}{2a} \leq t \leq 3\left(\frac{2n-3}{2a}\right) \\ e^{-\beta t}, & x \geq 3\left(\frac{2n-3}{2a}\right) \end{cases}$$

(3.5)

Combining Equations (3.4) with Equation (3.5), the orthonormal basis functions are bounded by a similar expression with a different constant factor in front. Specifically

$$|\lambda_n(t)| \leq D \begin{cases} 1, & 0 \leq t \leq \frac{1}{2a(4n-6)} \\ (2at(4n-6))^{-1/4}, & \frac{1}{2a(4n-6)} \leq t \leq \frac{2n-3}{2a} \\ (4n-6)^{-1/4}\left[(4n-6)^{1/3} + |4n-6-2at|\right]^{-1/4}, & \frac{2n-3}{2a} \leq t \leq 3\left(\frac{2n-3}{2a}\right) \\ e^{-\beta t}, & t \geq 3\left(\frac{2n-3}{2a}\right) \end{cases}$$

(3.6)

Although cumbersome, Equation (3.6) will play a role in Chapter 5 when we analyze the approximation behavior of the bilinear representations.

3.2   The Biorthogonal Representation

In a parallel fashion to Section 3.1, we now explore important properties of the biorthogonal bilinear representation.

3.2.1   Weighted Energy Relationship

As stated previously, the biorthogonal signal representation does not preserve the standard inner product between continuous and discrete time. Consequently, instead of satisfying Equation (3.1), we have a weighted energy relationship between the CT signal and its DT expansion coefficients. By applying Equation (2.10), this can be written

$$\int_0^\infty t f^2(t)dt = \sum_{n=0}^\infty n f^2[n]$$

(3.7)

The weighting functions are given by t, in continuous time, and n, in discrete time. Equation (3.7) will be useful when characterizing the signal space of the primal basis functions.

3.2.2 Biorthogonal Signal Space

As discussed in Section 2.2, the primal basis functions are given in terms of the first-order Laguerre polynomials. From Appendix A, the polynomial set $\{L_n^{(1)}(x)\}_{n=0}^{\infty}$ forms a basis for causal functions $f(t)$ satisfying

$$\int_0^{\infty} |f(x)|^2 x e^{-x} dx < \infty \tag{3.8}$$

Let us now define $L_2(0, \infty; t)$ to be the space of functions $f(t)$ which satisfy

$$\int_0^{\infty} t|f(t)|^2 dt < \infty$$

It follows from Equations (2.9) and (3.8) that the set of primal basis functions $\{\phi_n(t)\}_{n=0}^{\infty}$ forms a basis for $L_2(0, \infty; t)$.

To see this, assume there exists $f(t) \in L_2(0, \infty; t)$ orthogonal to $\phi_n(t)$ $\forall n \geq 0$. This implies that all its expansion coefficients $f[n]$ are zero. Equivalently

$$\int_0^{\infty} e^{-at} f(t) dt \quad = \quad 0 \tag{3.9}$$

$$\int_0^{\infty} \frac{1}{n} t\phi_n(t) f(t) dt \quad = \quad 0 \text{ for } n \geq 0 \tag{3.10}$$

Notice that since $t \cdot \delta(t) = 0$, we do not need to consider the impulses in Equation (2.9).

Because $\{h_n(t)\}_{n=0}^{\infty}$ consists of polynomials weighted by a decaying exponential, there must be a linear combination which yields

$$\sum_{k=0}^{n} \alpha_n h_n(t) = e^{-at} t^n \ \forall n \geq 0 \tag{3.11}$$

From Equations (3.9) and (3.10), it follows that $\int_0^{\infty} e^{-at} t^n f(t) dt = 0 \ \forall n \geq 0$.

Now consider the Laplace transform $G(s) = \int_0^{\infty} e^{-st} e^{-at} t f(t) dt$. The magnitude of $G(s)$

can be bounded as follows:

$$
\begin{aligned}
|G(s)| &= \left| \int_0^\infty e^{-st} e^{-at} t f(t) dt \right| \\
&\leq \int_0^\infty e^{-\Re\{s\}t} e^{-at} t |f(t)| dt \\
&\leq \int_0^\infty \left(e^{-(\Re\{s\}+a)t} t^{1/2} \right) \left(t^{1/2} |f(t)| \right) dt \\
&\leq \left[\int_0^\infty e^{-2(\Re\{s\}+a)t} t \, dt \right]^{1/2} \left[\int_0^\infty t |f(t)|^2 dt \right]^{1/2}
\end{aligned}
\tag{3.12}
$$

where the final expression is obtained using the Cauchy-Schwartz inequality.

Since the second term in Equation (3.12) is finite, $G(s)$ is well-defined and analytic in the half-plane $\Re\{s\} > -a$. Thus, $G(s)$ can be represented in this region using a Taylor expansion about the point $s = 0$

$$
G(s) = \sum_{n=0}^\infty \left[\frac{d^n}{ds^n} G(s)|_{s=0} \right] \frac{s^n}{n!}
\tag{3.13}
$$

However, notice that

$$
\frac{d^n}{ds^n} G(s)|_{s=0} = (-1)^n \int_0^\infty e^{-at} t^{n+1} f(t) = 0 \ \forall n \geq 0
$$

Therefore, $G(s) = 0 \rightarrow f(t) = 0$

One way to verify the above signal space characterization is by considering the weighted energy of the error between the signal $f(t)$ and its M-term approximation as shown

$$
\begin{aligned}
\int_0^\infty t \cdot e_M^2(t) dt &= \sum_{n=M+1}^\infty n f^2[n] \\
&= \int_0^\infty t \cdot f^2(t) dt - \sum_{n=1}^M n f^2[n]
\end{aligned}
\tag{3.14}
$$

Once again, the first term in the right-hand side of Equation (3.14) is finite and $n f^2[n]$ is non-negative for $n \geq 0$. Thus, the bilinear representation should converge to the true CT signal in the sense that the weighted energy of the error goes to zero as $M \rightarrow \infty$.

Finally, we remark that although the biorthogonal bilinear representation does not span the entire space $L_2(0, \infty)$, most real-world analog signals are bounded with finite duration.

These signals lie within $L_2(0, \infty; t)$ and can therefore be represented using the biorthogonal bilinear expansion.

3.2.3 Computing Inner Products using the Biorthogonal Expansion

Although the standard inner product of two signals is not preserved, we can use the biorthogonal representation $f(t) = \sum_{n=0}^{\infty} f[n]\phi_n(t)$ to manipulate the CT inner product expression according to

$$
\begin{aligned}
\int_0^{\infty} f(t)g(t)dt &= \int_0^{\infty} \left(\sum_{n=0}^{\infty} f[n]\phi_n(t) \right) g(t)dt \\
&= \sum_{n=0}^{\infty} f[n] \left(\int_0^{\infty} g(t)\phi_n(t) \right)
\end{aligned}
\tag{3.15}
$$

The expression $\int_0^{\infty} g(t)\phi_n(t)$ in Equation (3.15) is a scalar coefficient. Therefore, the CT inner product of two signals can be expressed using the expansion coefficients $f[n]$ and a new set of coefficients which we refer to as $b_g[n]$ (the subscript denotes the corresponding CT signal). Essentially, the signal $g(t)$ is expanded with respect to the dual basis, $\{h_n(t)\}_{n=0}^{\infty}$, and the coefficients $b_g[n]$ are the expansion coefficients of this new representation.

Since the Laplace transforms of successive primal basis functions $\Phi_n(s) = \left(\frac{a-s}{a+s} \right)^n$ differ by an all-pass filter, the coefficient sequence $b_g[n]$ can be computed by sampling the outputs of a first-order cascade similar to the ones in Figures (2-3) and (2-9). This network is shown in Figure (3-1).
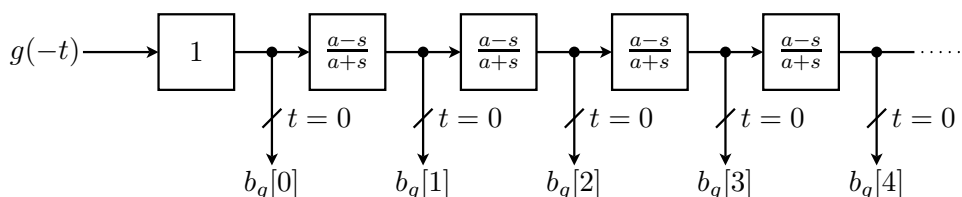
Figure 3-1: First-order cascade used to compute the coefficients $b_g[n]$ for the biorthogonal inner product.

3.2.4 Bounds on the Primal and Dual Basis Functions

Let $\phi_{b,n}(t)$ denote the bounded portion of the primal basis functions. For $n > 0$, we can express this quantity as follows:

$$\phi_{b,n}(t) = 2a(-1)^{n-1}e^{-at}L_{n-1}^{(1)}(2at)u(t) \tag{3.16}$$

From Chapter 2, the corresponding dual basis functions are $h_n(t) = \frac{1}{n}t\phi_{b,n}(t)$.

Using Equation (A.6) we can rewrite $\phi_{b,n}(t)$ and $h_n(t)$ in terms of the normalized first-order Laguerre polynomial with argument $x = 2at$.

$$\phi_{b,n}(t) = \sqrt{\frac{2an}{t}}(-1)^{n-1}\zeta_{n-1}^{(1)}(2at) \tag{3.17}$$

$$h_n(t) = \sqrt{\frac{2at}{n}}(-1)^{n-1}\zeta_{n-1}^{(1)}(2at) \tag{3.18}$$

By applying Equation (A.7) and using $\nu = 4(n-1)$, the normalized Laguerre polynomial $\zeta_{n-1}^{(1)}(2at)$ is bounded according to

$$|\zeta_{n-1}^{(1)}(2at)| \leq C \begin{cases} (8at(n-1))^{1/2}, & 0 \leq t \leq \frac{1}{8a(n-1)} \\ (8at(n-1))^{-1/4}, & \frac{1}{8a(n-1)} \leq t \leq \frac{n-1}{a} \\ (4n-4)^{-1/4}\left[(4n-4)^{1/3} + |4n-4-2at|\right]^{-1/4}, & \frac{n-1}{a} \leq t \leq 3\left(\frac{n-1}{a}\right) \\ e^{-\beta t}, & x \geq 3\left(\frac{n-1}{a}\right) \end{cases} \tag{3.19}$$

Combining Equations (3.19) with Equations (3.17) and (3.18), we have

$$|\phi_{b,n}(t)| \leq C \begin{cases} 4a\sqrt{\frac{n-1}{n}}, & 0 \leq t \leq \frac{1}{8a(n-1)} \\ \left(\frac{an^2}{2t^3(n-1)}\right)^{1/4}, & \frac{1}{8a(n-1)} \leq t \leq \frac{n-1}{a} \\ \left(\frac{a^2n^2}{t^2(n-1)}\right)^{1/4}\left[(4n-4)^{1/3} + |4n-4-2at|\right]^{-1/4}, & \frac{n-1}{a} \leq t \leq 3\left(\frac{n-1}{a}\right) \\ e^{-\beta t}\sqrt{\frac{2an}{t}}, & t \geq 3\left(\frac{n-1}{a}\right) \end{cases} \tag{3.20}$$

$$|h_n(t)| \leq C \begin{cases} 4at\sqrt{\frac{n-1}{n}}, & 0 \leq t \leq \frac{1}{8a(n-1)} \\ \left(\frac{at}{2n^2(n-1)}\right)^{1/4}, & \frac{1}{8a(n-1)} \leq t \leq \frac{n-1}{a} \\ \left(\frac{a^2t^2}{n^2(n-1)}\right)^{1/4} \left[(4n-4)^{1/3} + |4n-4-2at|\right]^{-1/4}, & \frac{n-1}{a} \leq t \leq 3\left(\frac{n-1}{a}\right) \\ e^{-\beta t}\sqrt{\frac{2at}{n}}, & t \geq 3\left(\frac{n-1}{a}\right) \end{cases}$$

$$(3.21)$$

Once again these bounds will be useful when analyzing the approximation properties of the bilinear representations.

Chapter 4

MATLAB Implementation of Bilinear Analysis and Synthesis

The bilinear representations are simulated numerically using MATLAB. Since MATLAB operates on discrete-time vectors rather than continuous-time signals, it is important to consider the analysis and synthesis network implementations. This chapter provides an overview of the techniques used to approximately implement these systems as well as some of the limitations.

4.1 The Analysis Network

In order to compute the bilinear expansion coefficients according to Figures (2-3) and (2-9), we use the trapezoidal rule for integration. This approximation allows us to represent a CT derivative using a DT first-difference operation.

For the two bilinear expansions, we implement this technique on a single-pole system with transfer function and input/output differential equation shown below:

$$H(s) = \frac{A}{a + s} \tag{4.1}$$

$$\frac{d}{dt}y(t) = \dot{y}(t) = Ax(t) - ay(t) \tag{4.2}$$

By integrating Equation (4.2) over an interval of length T and using the trapezoidal

rule for integration, specifically,

$$\int_{nT-T}^{nT} f(\tau)d\tau \approx \frac{T}{2}\left[f(nT) + f(nT - T)\right] \tag{4.3}$$

we can write the samples of the output signal, $y(nT)$ in terms of the input samples $x(nT)$ according to the expression

$$y(nT) \approx \frac{1}{1 + aT/2}\left\{\frac{AT}{2}\left[x(nT) + x(nT - T)\right] + \left[1 - aT/2\right]y(nT - T)\right\} \tag{4.4}$$

Thus, by transforming the differential equation of Equation (4.2) into an integral equation, we can approximate the sampled output of a first-order CT filter using only discrete-time operations. In addition, by decomposing the all-pass filters as

$$\frac{a - s}{a + s} = \frac{2a}{a + s} - 1 \tag{4.5}$$

Equation (4.4) can be used for all of the first-order systems in Figures (2-3) and (2-9).

4.2 The Synthesis Network

Ideally, we would like to reconstruct a CT signal from its bilinear expansion coefficients. This is necessary when analyzing both the bilinear approximation properties and the associated approximation errors. However, since MATLAB operates on DT vectors, all "continuous-time" signals must really be vectors of very finely-spaced time samples. Therefore, in evaluating the re-synthesis, we reconstruct samples of the bilinear expansion and compare it to samples of the original vector.

We obtain samples of the reconstructed signal by relying on the MATLAB function *impulse* to generate samples of $\lambda_n(t)$ and $\phi_n(t)$. However, since *impulse* cannot represent the Dirac delta functions in $\phi_n(t)$, the biorthogonal reconstruction is inaccurate at one point, namely $t = 0$.

4.3 Limitations of the Continuous Time Approximations

While convenient for numerical simulation, there are limitations to the approximations discussed above. These issues are somewhat different for the analysis and the synthesis

networks due to the techniques used in each case.

4.3.1 The Analysis Network

For the analysis network, the trapezoidal approximation seems empirically reasonable only when the CT signal is sampled above 10 times its Nyquist rate. This means that the vectors of sampled CT signals grow very rapidly in size as the signal duration increases, and large amounts of computation may be required to calculate the expansion coefficients.

Additionally, the trapezoidal rule for integration introduces errors into the bilinear coefficients. For comparison, the coefficients obtained when using symbolic integration to evaluate the inner products differ slightly from those obtained numerically using MATLAB. Although the accuracy may be improved by using a higher-order derivative approximation, it is unclear whether the additional improvement will justify the inevitable increase in computational complexity.

4.3.2 The Synthesis Network

The main limitation of the synthesis network is that MATLAB does not have enough dynamic range to represent the time samples of high-index basis functions. This can be seen by considering the form of the bilinear basis functions (minus the Dirac impulse in the biorthogonal case)

$$\lambda_n(t) \;\; = \;\; e^{-at} \sum_{k=0}^{n-1} \alpha_k (2at)^k \tag{4.6}$$

$$\phi_n(t) \;\; = \;\; e^{-at} \sum_{k=0}^{n-1} \beta_k (2at)^k \tag{4.7}$$

As the index increases, the value of the leading monomial terms in Equations (4.6) and (4.7) increase exponentially. At some point, these values cannot be represented in the given dynamic range. This means that the reconstructions of the basis functions and the CT signal will not be accurate. This effect is illustrated by plotting the basis function $\lambda_n(t)$ for two different indices.

As seen in Figure (4-1), the lower-index basis function (blue) is smooth and well-behaved. This is very similar to the behavior shown in Figures (2-1) and (2-2). Conversely, the high-index basis function (green) exhibits violent oscillations, which are uncharacteristic of

41
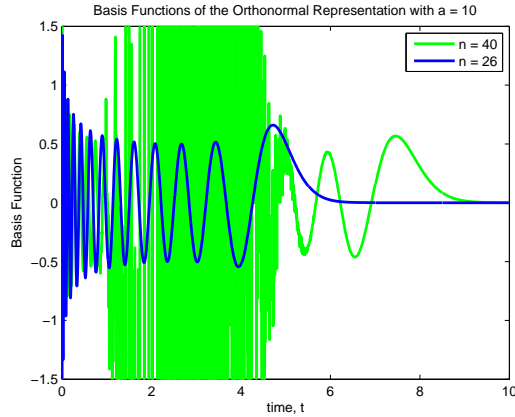
Figure 4-1: Orthonormal basis functions using $a = 10$

either a polynomial or a decaying exponential. The behavior suggests that the green curve is exceeding the allotted dynamic range, and is therefore being clipped.

While it may be possible to mitigate this effect by changing the order in which polynomials are evaluated and summed, the dynamic range will always be a fundamental limitation of using digital processing for polynomial sums.

Although comparatively less important, another problem with the synthesis network is that obtaining samples of the inverse transform is very computationally expensive. This becomes especially noticeable for high-order transfer functions.

Chapter 5

Approximation Properties of the Bilinear Representations

We introduced the technique of signal approximation in Chapter 1 and presented a brief argument as to why it is necessary in several real-world applications. Chapters 2 and 3 have focused on a specific expansion which implements a bilinear frequency warping relationship. For the remainder of this thesis, we turn our attention to the approximation properties of these bilinear basis functions.

In this chapter we study the approximation problem from a more theoretical perspective. We observe the approximation behavior for specific analytical signals and draw conclusions about signal characteristics which can be well-approximated with the bilinear functions. Chapter 6 examines an alternative representation in which the original CT signal is segmented using a short-duration window. The final three chapters are devoted to signal approximation applications.

Section 5.1 of this chapter introduces some basic concepts of signal approximation. In Section 5.2 we investigate the effect of the the the parameter a on the approximation performance. Sections 5.3 and 5.4 focus on classes of signals which are well-approximated using the bilinear basis functions, and Section 5.5 considers some general signal characteristics that impact the approximation performance. In Section 5.6 we summarize our findings as well as compare the orthonormal and biorthogonal representations.

5.1 Approximation of Signals

Equation (1.10) gives a general expression for the approximation $\hat{f}(t)$ in which the expansion coefficients may be modified based on the index set I_M. In this thesis, however, we consider only approximations for which the expansion coefficient sequence remains unchanged. Namely, the M-term approximation of $f(t) = \sum_{n=-\infty}^{\infty} f[n]\psi_n(t)$ is written

$$\hat{f}_M(t) = \sum_{n \in I_M} f[n]\psi_n(t) \tag{5.1}$$

where I_M denotes a set of M index values, and $f[n]$ is the original n^{th} expansion coefficient. The advantage of using Equation (5.1) is that we do not need to perform additional computations to obtain modified coefficients for the signal approximation. This method will be used for both the orthonormal and the biorthogonal representations.

The material in this section is drawn from Chapter 9 of Mallat [7]. Although much of the information has been developed for orthonormal signal representations, we make generalizations to the biorthogonal case.

5.1.1 Linear vs. Nonlinear Approximation

In this discussion, we consider both linear and nonlinear approximations, as defined below.

Linear Approximation refers to having a fixed index set I_M, irrespective of the CT signal being approximated. Given the bilinear analysis and synthesis networks shown in Chapter 2, a reasonable linear approximation scheme is to retain the first M terms of the expansion. This is because obtaining successive basis functions and/or expansion coefficients corresponds to adding first-order analog filters to the cascade. Therefore, selecting the first M terms minimizes the hardware requirements of the system.

Nonlinear Approximation refers to selecting the index set I_M based on the characteristics of $f(t)$. Because the indices vary from signal to signal, the approximation of $f_1(t)+f_2(t)$ does not necessarily equal the sum of individual approximations, $\hat{f}_1(t)+\hat{f}_2(t)$. However, nonlinear approximation always has the potential to perform better than linear approximation because the latter is a subset of the former.

5.1.2 Error Metrics

Given the original CT signal $f(t)$ and its M-term approximation $\hat{f}_M(t)$, we will consider the following error metrics:

$$\epsilon[M] \quad = \quad \int_0^\infty (f(t) - \hat{f}_M(t))^2 dt \tag{5.2}$$

$$\delta[M] \quad = \quad \int_0^\infty f^2(t)dt - \int_0^\infty \hat{f}^2(t)dt \tag{5.3}$$

$\epsilon[M]$ is the energy of the difference, also termed the reconstruction error, between the original and the approximated signals. In contrast, $\delta[M]$ is the difference in energy between the two signals. As discussed in Chapters 7-9, $\epsilon[M]$ is our chosen error metric when approximating audio signals whereas $\delta[M]$ is more significant in the binary detection problem.

For the orthonormal bilinear representation $f(t) = \sum_{n=1}^\infty f[n]\lambda_n(t)$, it is straightforward to show that

$$\epsilon[M] = \delta[M] = \sum_{n \notin I_M} f^2[n] \tag{5.4}$$

Therefore, to minimize $\epsilon[M]$ and $\delta[M]$ in this case, we should select the indices I_M corresponding to the largest coefficient magnitudes $|f[n]|$ in the expansion.

For the biorthogonal bilinear representation $f(t) = \sum_{n=0}^\infty f[n]\phi_n(t)$, there is no straightforward way of minimizing the quantity $\epsilon[M]$ short of computing the reconstruction error for every M-term subset of expansion coefficients. However, we suggest below a simple procedure to minimize the quantity $\delta[M]$.

With $b_f[n]$ denoting the sequence of secondary expansion coefficients from Figure (3-1), we define the inner product sequence as follows:

$$IP[n] = f[n]b_f[n], \text{ for } 0 \le n < \infty \tag{5.5}$$

Note that the signal energy is $\int_0^\infty f^2(t)dt = \sum_{n=0}^\infty IP[n]$.

By drawing from the orthonormal case, we obtain the nonlinear approximation set I_M by selecting the (same) indices of both $f[n]$ and $b_f[n]$ which correspond to the maximum values in $IP[n]$. While this may not be the theoretically optimal way to minimize Equation (5.3), it is a practical solution because we do not need to modify our coefficient sequences, and we do not need to combinatorially search over all possible M-term approximations.

One repercussion of the proposed method is that minimizing $\delta[M]$ is not equivalent to minimizing $\epsilon[M]$ in the biorthogonal case. Therefore, we may end up with a large reconstruction error using the set I_M from above. To avoid such a situation, we will consider only the orthonormal representation for audio approximation.

5.1.3 Qualitative Measure of Approximation Performance

We can combine the material presented in Chapter 9 of [7] with that of the previous section to determine a metric for evaluating the bilinear approximation performance. Throughout this section, we use $f_r[n]$ to denote the sequence of orthonormal expansion coefficients when sorted (in descending order) by absolute value, and $IP_r[n]$ to denote the sorted inner product coefficients from Equation (5.5).

Theorem 9.4 in [7] relates the decay of $|f_r[n]|$ with the decay of the M-term approximation error $\epsilon[M]$. It states that if $|f_r[n]| \leq Cn^{-s}$, then $\epsilon[M] \leq \frac{C^2}{2s-1}M^{(1-2s)}$. The author's main conclusion is that the orthonormal nonlinear approximation performance depends heavily on the decay of sorted expansion coefficients, with a faster decay corresponding to a smaller M-term error.

We can extend this reasoning to the biorthogonal case by considering the decay of $IP[n]$. Thus, we qualitatively compare the orthonormal and biorthogonal nonlinear approximation performances by observing how quickly the sequences $f_r^2[n]$ and $IP_r[n]$ decay.

Additionally, we can evaluate the M-term linear approximations by plotting the partial sum sequences

$$S_{ON}[M] \;\; = \;\; \sum_{n=1}^{M} f^2[n] \tag{5.6}$$

$$S_{BiO}[M] \;\; = \;\; \sum_{n=0}^{M-1} IP[n] \tag{5.7}$$

and by observing how quickly they approach the original signal energy.

5.2 Effect of the Parameter, a

Figures (2-2), (2-6) and (2-8) indicate that the basis function behavior depends on the parameter a. Predictably, this has a direct impact on the approximation performance of

both the orthonormal and the biorthogonal expansions. In this section we evaluate how the choice of a affects, in particular, the growth of partial sums $S_{ON}[M]$ and $S_{BiO}[M]$, as well as the decay of sorted coefficient $f_r^2[n]$ and $IP_r[n]$.

For simplicity, we analyze the bilinear approximations for the windowed sinusoid $f(t) \sim \sin(10t)$, for $0 \le t < 1$, when using different values of a, and generalize from this information. The signal $f(t)$ is normalized to have unit energy.

Figure (5-1) shows the orthonormal bilinear coefficients for $a = 1, 10, 100,$ and 1000 respectively. Figure (5-2) shows the corresponding sorted coefficients and partial sum sequence. The biorthogonal expansion exhibits a similar behavior.

(a) $a = 1$

(b) $a = 10$

(c) $a = 100$

(d) $a = 1000$
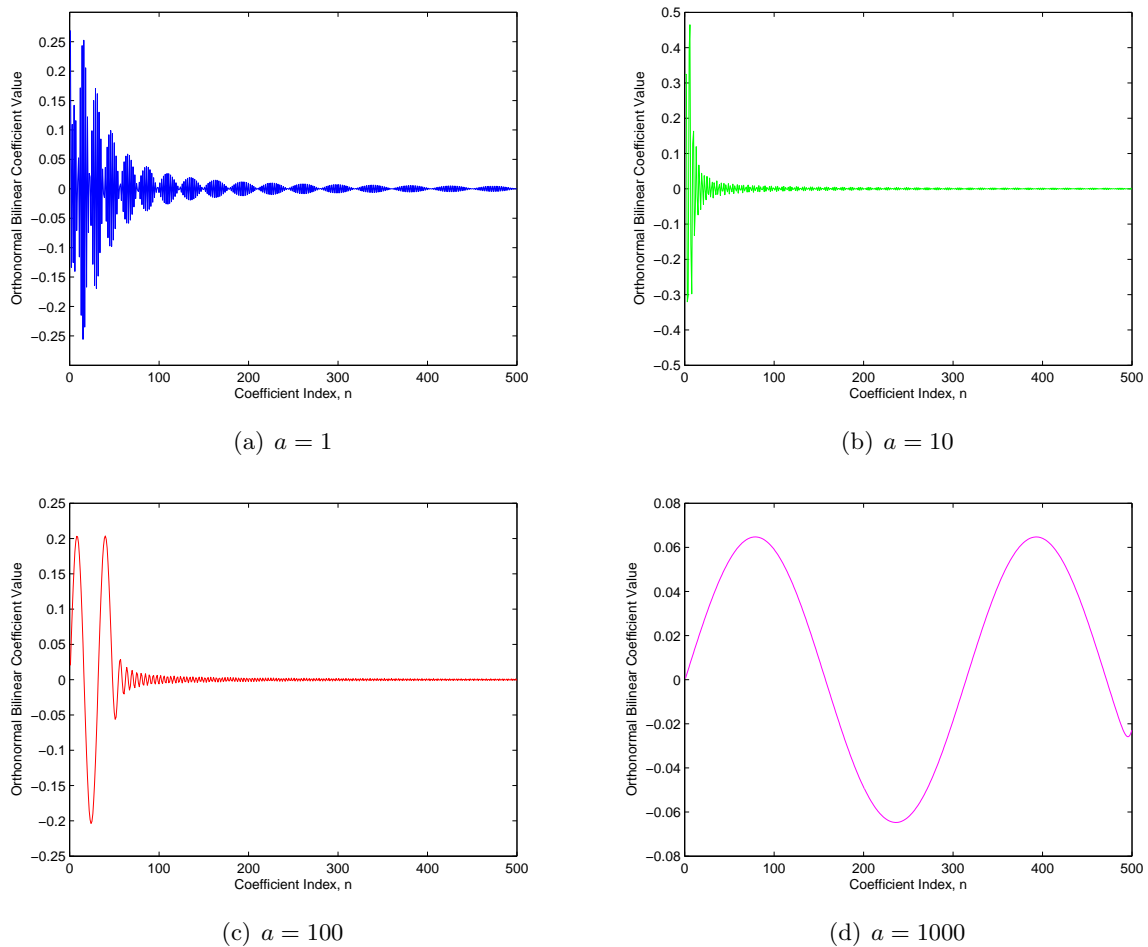
Figure 5-1: Orthonormal Bilinear Expansion Coefficients for $f(t) \sim \sin(10t)$

47
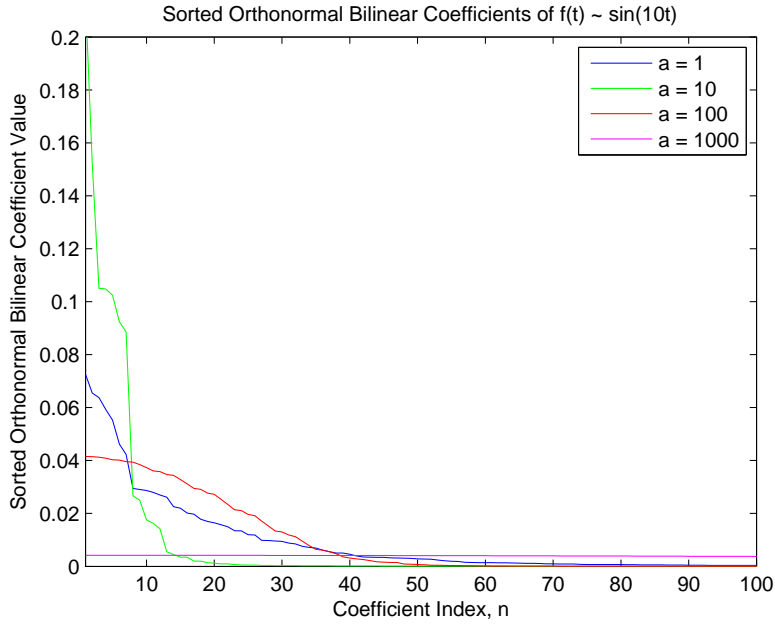
(a) Sorted Orthonormal Expansion Coefficients
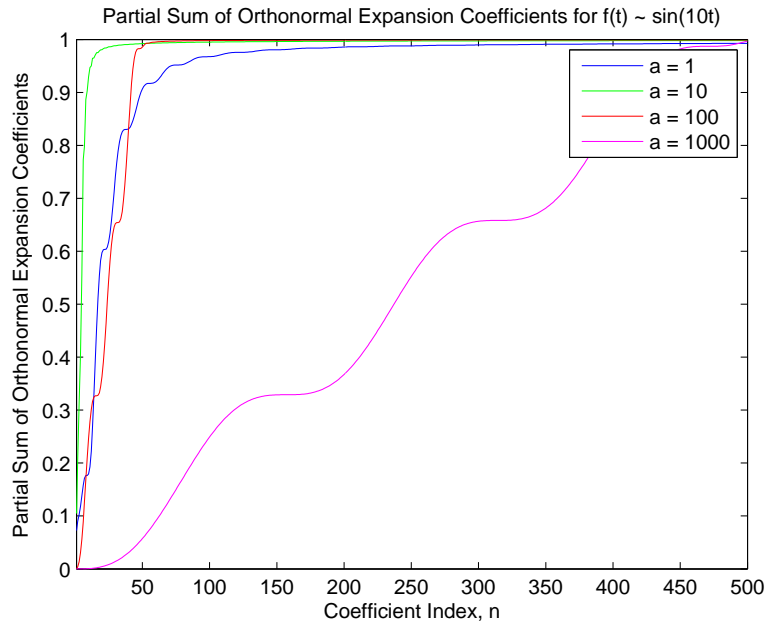
(b) Orthonormal Partial Sum Sequence

Figure 5-2: Metrics of Linear and Nonlinear Approximation Performance when using the Orthonormal Expansion for $f(t) \sim \sin(10t)$

As seen, both the fastest decay and the fastest growth in Figure (5-2) occur when $a = 10$, or the carrier frequency of the original signal $f(t)$. We can argue this result by looking at the group delay of the all-pass filters in the bilinear first-order cascades.

$$\tau_g(\omega) = \frac{d}{d\omega}\left[\angle \left(\frac{a - j\omega}{a + j\omega} \right) \right] = \frac{2a}{a^2 + \omega^2} \tag{5.8}$$

Consider a finite-duration signal whose energy is tightly concentrated around a center frequency of ω_o. For a narrow-band signal, the effect of an all-pass filter can be roughly approximated by a time delay of $\tau_g(\omega_o)$. However, since the signal has finite duration, successive delays of $\tau_g(\omega_o)$ will eventually shift the majority of its energy beyond the sampling time, $t = 0$. After this point, the remaining expansion coefficients are approximately zero.

Therefore, in order to minimize the number of significant DT coefficients, we should maximize the group delay, since this is equivalent to minimizing the number of stages before the signal has been shifted beyond the time $t = 0$. Equation (5.8) is maximized when $a = \omega_o$, meaning this value should yield the fastest coefficient decay.

Although many of the signals we would like to approximate may not be narrow-band, the above analysis suggests a reasonable way of initializing the value of a. Namely, we can employ the following 'maximin' strategy:

For a signal with frequency content effectively band-limited to ω_M, choose $a = \omega_M$.

Because the group delay in Equation (5.8) is monotonically decreasing in ω, we are guaranteed a group delay greater than or equal to $\tau_g(\omega_M)$ for all frequencies in the range of interest. Once the parameter a has been initialized, we may be able to adjust its value, based on the CT signal $f(t)$, to achieve better approximation performance.

5.3 Exact Representation of a Signal using a Finite Number of DT Expansion Coefficients

As developed in Chapter 2 the bilinear basis functions have Laplace transforms $\Lambda_n(s) = \frac{\sqrt{2a}}{a+s}\left(\frac{a-s}{a+s}\right)^{n-1}$ and $\Phi_n(s) = \left(\frac{a-s}{a+s}\right)^n$. From these expressions, it is easy to verify that signals which can be exactly represented using a finite number of expansion coefficients have rational Laplace transforms with all poles located at $s = -a$.

Consider M-term linear approximation discussed in Section 5.1. A CT signal within the span of the first M basis functions has a rational Laplace transform with at most M poles at $s = -a$ and at most $(M - 1)$ zeros elsewhere in the S-plane. In the time domain, this corresponds to functions of the form

$$f(t) = \left(\sum_{n=0}^{M-1} c_n t^n \right) e^{-at} u(t) \tag{5.9}$$

To illustrate the above property, Figure (5-3) shows the sorted orthonormal expansion coefficients and the sorted biorthogonal inner product coefficients for the functions $s_k(t) \sim t^k e^{-at}$ for $k = 1, \ldots, 5$. Each $s_k(t)$ is normalized to have unit energy. As seen, a function with a kth order monomial term has at most $k + 1$ non-zero (i.e. significant) coefficients.

If we are now allowed to select any M expansion coefficients, the set of exactly-represented signals is still restricted to rational Laplace transforms with all poles located at $s = -a$. However, there is now a constraint on the zero locations. Specifically, if I_M represents the set of retained indices, then we can only represent signals which are linear combinations of the I_M Laguerre polynomials weighted by a decaying exponential. Thus, we do not gain much more intuition by looking at a nonlinear approximation.

5.4 Deviating from an Exact Representation

We conjecture that a signal which has a rational Laplace transform with pole location(s) near the value $s = -a$ should be well-represented using a finite number of bilinear basis functions. However, the approximation performance should worsen as the poles move farther away from $s = -a$.

In this section, we use two methods of gradually altering the pole locations. First, we change the exponential decay of the signal. This is equivalent to sliding the poles along the real axis. Second, we modulate the signal with sinusoids of varying frequencies. This moves the (conjugate) poles perpendicular to the real axis.

Consider signals of the form $f_k(t) \sim t^3 e^{-kt}$, normalized to have unit energy. Figures (5-4) and (5-5) show the sorted bilinear coefficients and the partial sum sequences, respectively, as the exponential decay k is varied. A parameter value of $a = 50$ is used to compute all bilinear expansions.
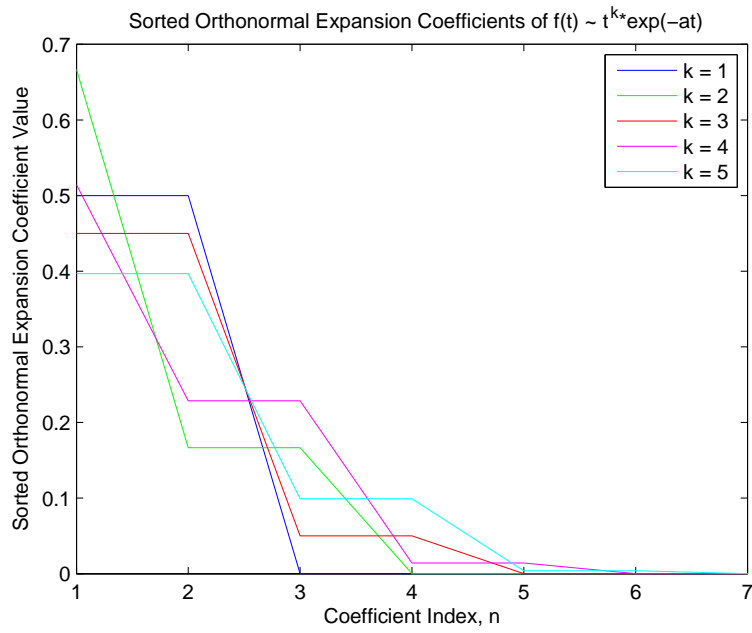
(a) Orthonormal Expansion Coefficients
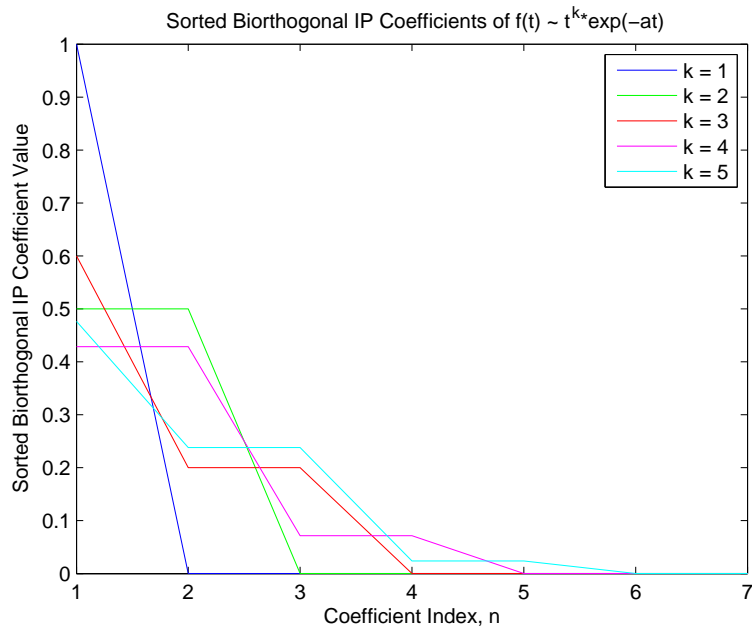
(b) Biorthogonal Inner Product Coefficients

Figure 5-3: Sorted Bilinear Coefficients for $f_k(t) \sim t^k e^{-at}$, $a = 20$
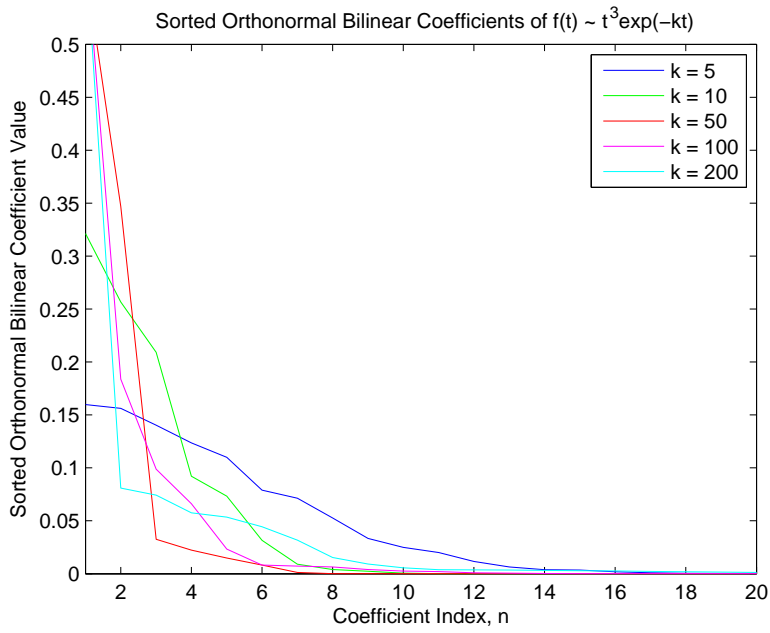
(a) Orthonormal Expansion Coefficients
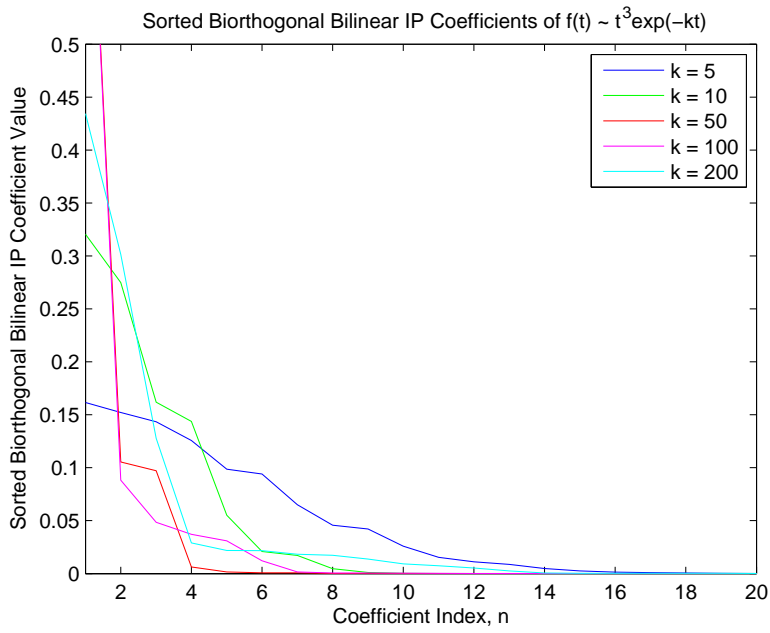
(b) Biorthogonal Inner Product Coefficients

Figure 5-4: Sorted Bilinear Coefficients for $f_k(t) \sim t^3 e^{-kt}$, $a = 20$
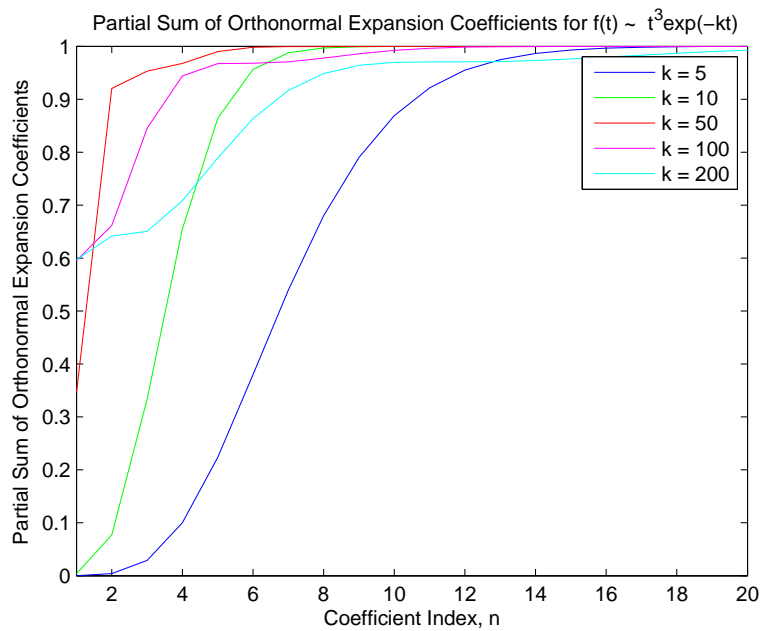
(a) Orthonormal Expansion Coefficients
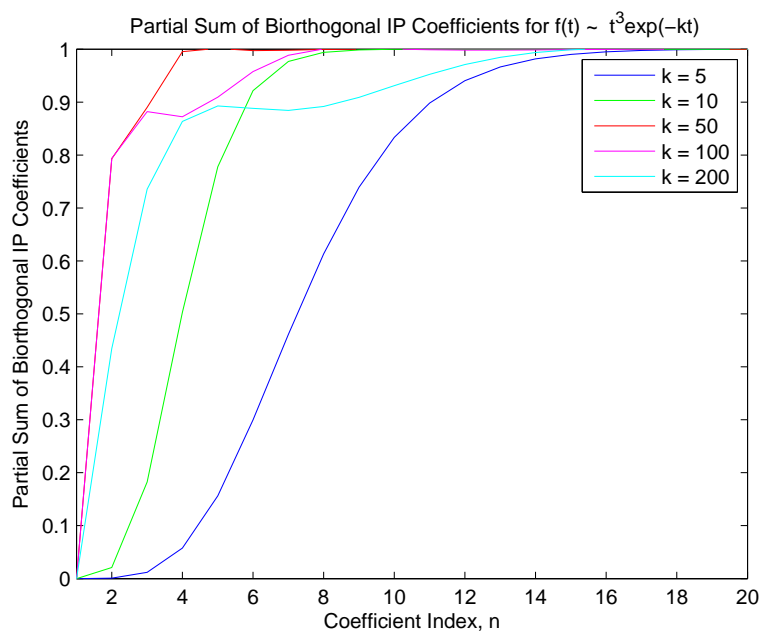
(b) Biorthogonal Inner Product Coefficients

Figure 5-5: Partial Sum Sequences for $f_k(t) \sim t^3 e^{-kt}$, $a = 20$

As seen, the best approximation performance occurs when $k = a = 50$, corresponding to the exact representation case. Notice, however, that the approximation performance is worse for $k < a$ than for $k > a$. This effect will be discussed further in Section 5.5.

Now consider signals of the form $f_k(t) \sim e^{-at} \sin(kt)$, once again, normalized to have unit energy. Figures (5-6) and (5-7) show the sorted bilinear coefficients and the partial sum sequences, respectively, as the carrier frequency k is varied. A parameter value of $a = 20$ is used to compute all bilinear expansions.

As seen, the approximation performance is best for $k = 5$ and worsens fairly rapidly for $k > 20$. This behavior ties back to the group delay argument from the previous section. As the modulating frequency increases, the corresponding group delay decreases $\sim \frac{1}{\omega^2}$. This implies that there should be more and more significant terms in the expansion as k increases.

5.5 Additional Signal Characteristics which Affect the Bilinear Approximation Performance

In the preceding section we investigated signals with rational Laplace transforms, focusing on how the pole location affects the approximation. In this section we look at more general signal properties which play a large role in the bilinear approximation performance. These include the energy distribution over time, isolated discontinuities, and the signal decay rate.

5.5.1 Distribution of Energy over Time

In Section 5.4 we observed that, relative to the value of a, the approximation performance is worse for slower exponential decays, than for faster ones. We can extend this observation to a more general class of signals by examining the energy distribution over time. To this end, consider signals of the following form:

$$f_n(t) \sim \begin{cases} sinc(10(t-n)), & 0 \le t < 1 \\ 0, & \text{otherwise} \end{cases} \qquad (5.10)$$

Again, the signal $f_n(t)$ has been normalized for unit energy. A windowed *sinc* pulse is chosen for this experiment because it does not have a rational Laplace transform, but it does have a large energy concentration around its main lobe.
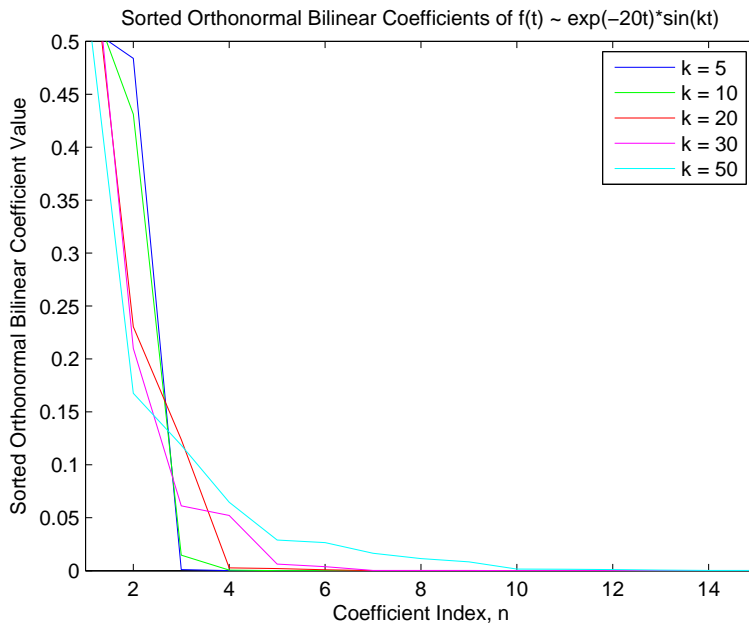
(a) Orthonormal Expansion Coefficients
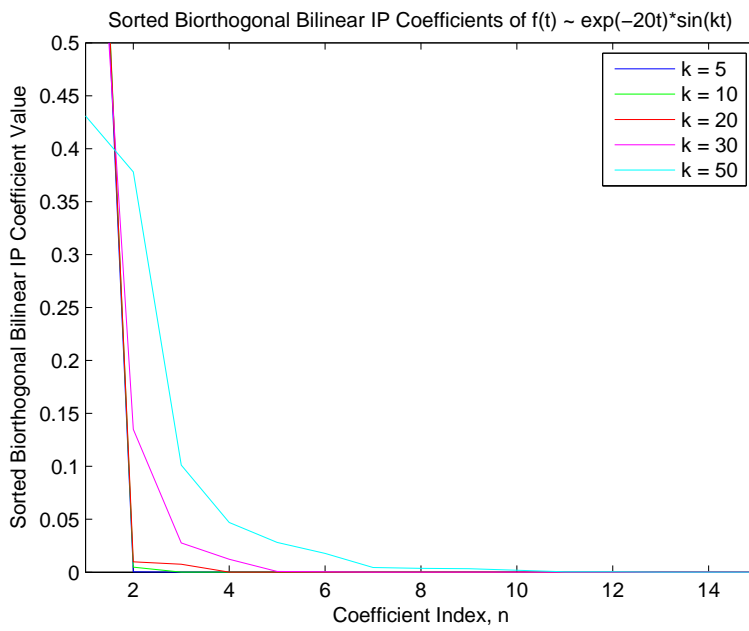
(b) Biorthogonal Inner Product Coefficients

Figure 5-6: Sorted Bilinear Coefficients for $f_k(t) \sim e^{-at}\sin(kt)$, $a = 20$
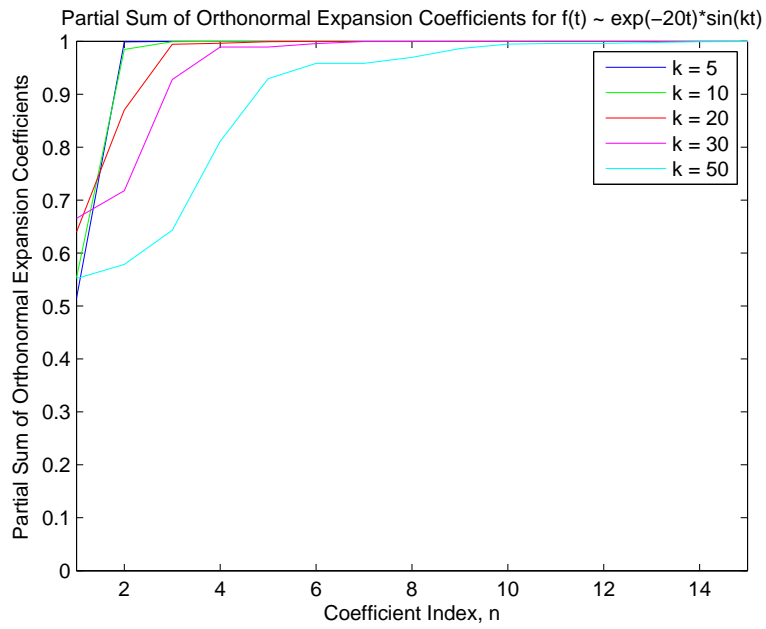
(a) Orthonormal Expansion Coefficients
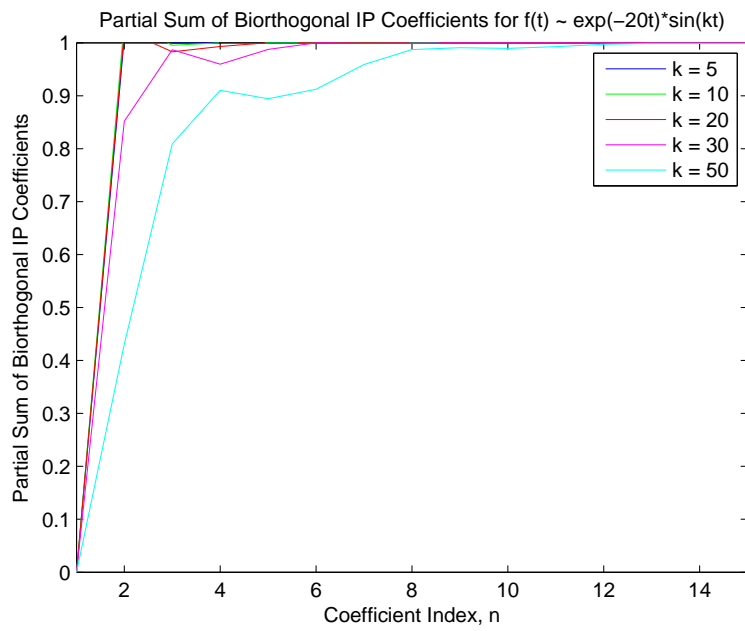
(b) Biorthogonal Inner Product Coefficients

Figure 5-7: Partial Sum Sequences for $f_k(t) \sim e^{-at}\sin(kt)$, $a = 20$

Figures (5-8) and (5-9) depict the sorted bilinear coefficients and the partial sum sequences, respectively. A value of $a = 10$ is used for all bilinear expansions.

Clearly, as the energy concentration moves farther from the time origin, the approximation performance worsens. We can justify this observation using the basis function bounds from Equations (3.6) and (3.20). If we assume that the exponentially decaying portion of the bounds is negligible and approximately zero, the time support of $\lambda_n(t)$ and $\phi_n(t)$ is a linearly-increasing function of the index n. The increasing time support is shown pictorially in Figures (2-1) and (2-5). Consequently, we require contributions from a greater number of basis functions in order to represent signal content at later times. This is also the reason why slowly-decaying exponentials require more expansion terms relative to quickly decaying exponentials in Section 5.4.

5.5.2   Isolated Discontinuities

A rectangular pulse is used to examine the effect of isolated discontinuities on the bilinear approximation and reconstruction. Mathematically,

$$f(t) \sim \begin{cases} 1, & 0 \leq t < 0.1 \\ 0, & \text{otherwise} \end{cases} \tag{5.11}$$

A value of $a = 68.2$ is used to compute the bilinear expansions, since this corresponds to the first zero-crossing in the frequency response.

Figure (5-11) shows the sorted bilinear coefficients and partial sum sequences for both representations. As seen, the partial sum sequences converge very slowly towards the original signal energy. This results in large reconstruction errors around the signal discontinuities at $t = 0, 0.1$ as shown in Figure (5-10).

The oscillatory behavior in Figure (5-10) can be attributed to the smooth nature of the bilinear functions, which cannot represent discontinuities very well. Furthermore, because the basis functions have increasing time support, the effect of a discontinuity is not localized to a small number of expansion coefficients.
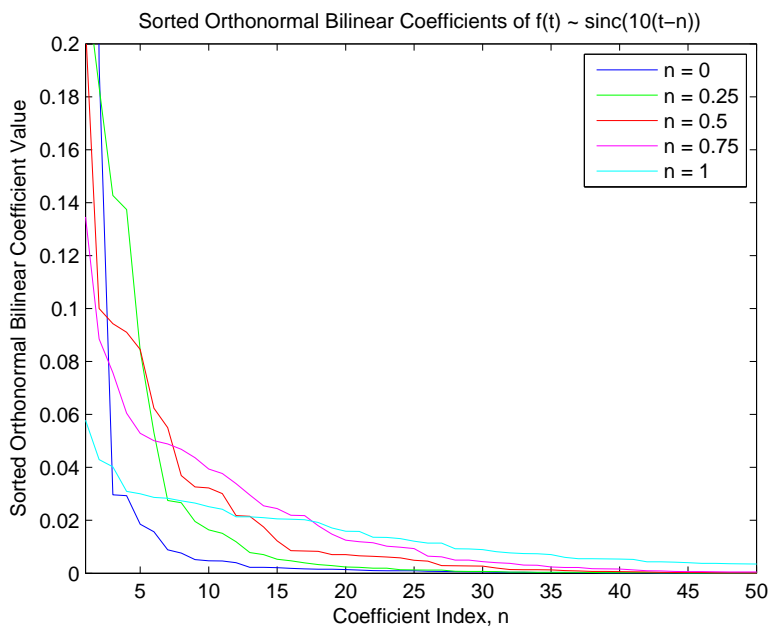
(a) Orthonormal Expansion Coefficients
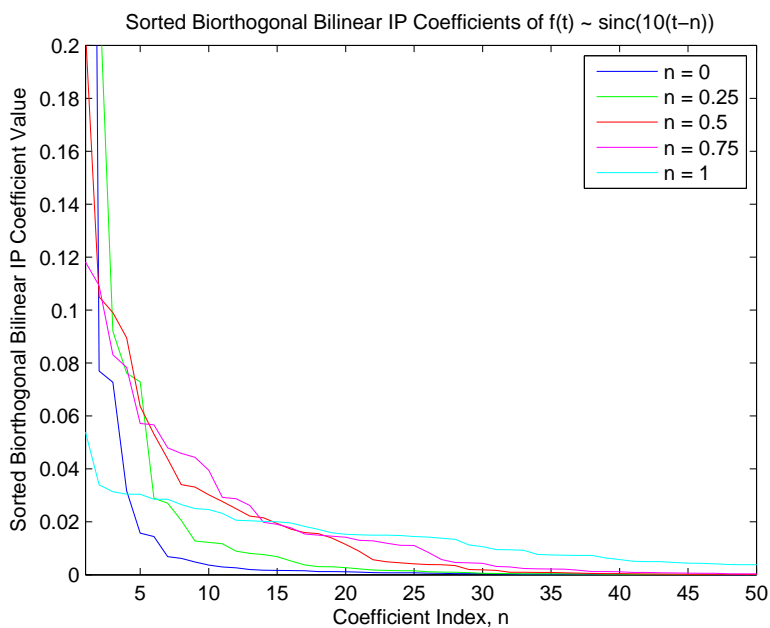
(b) Biorthogonal Inner Product Coefficients

Figure 5-8: Sorted Bilinear Coefficients for Shifted sinc Functions, $a=10$
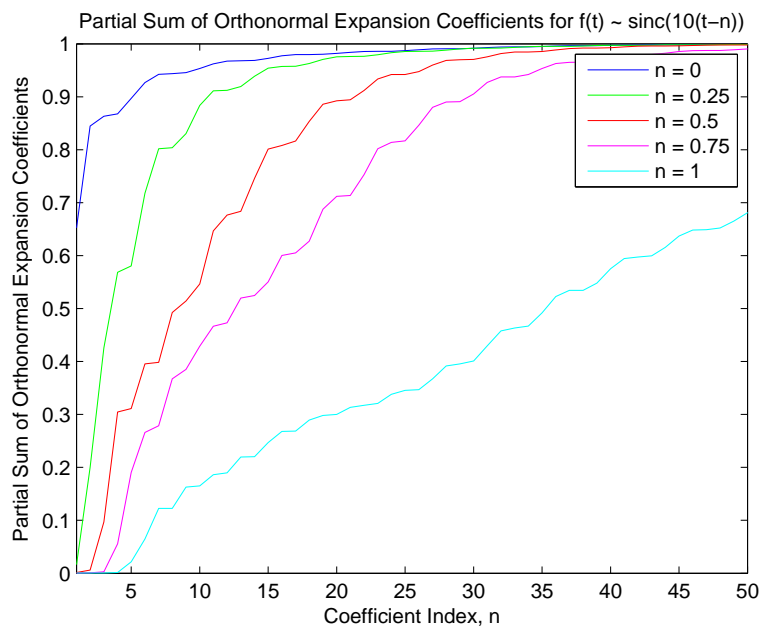
(a) Orthonormal Expansion Coefficients
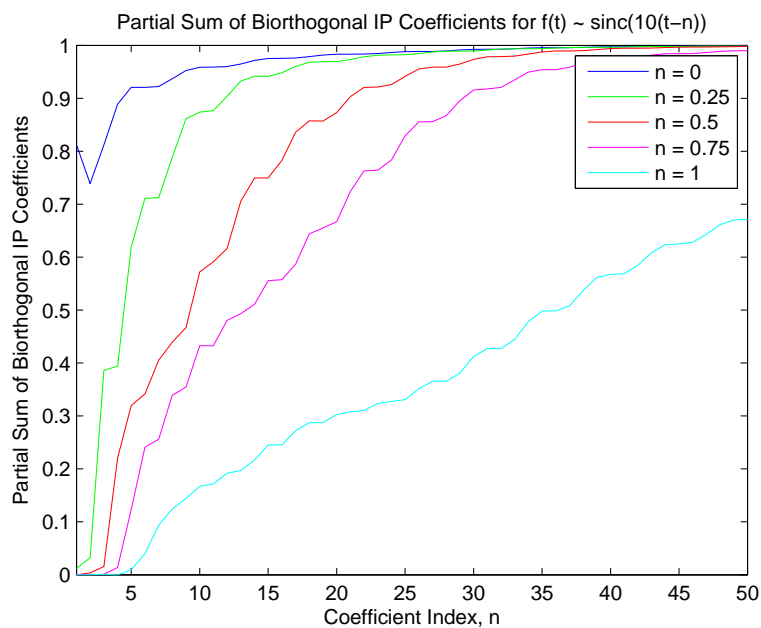
(b) Biorthogonal Inner Product Coefficients

Figure 5-9: Partial Sum Sequences for Shifted sinc Functions, $a=10$
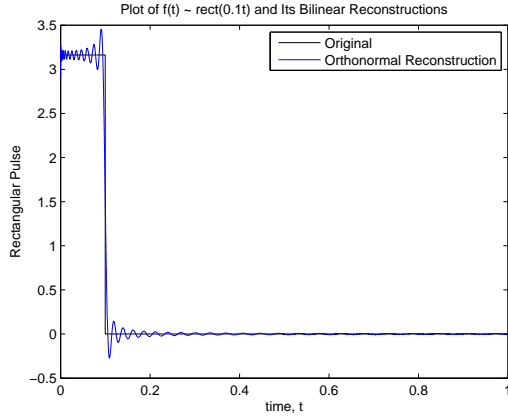
(a) Orthonormal Representation, $a = 62.8$
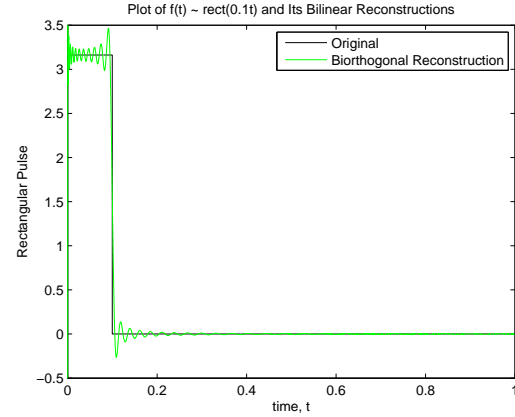
(b) Biorthogonal Representation, $a = 62.8$

Figure 5-10: Original Signal (black) and its Bilinear Reconstructions (color)

5.5.3 Signal Decay Rate

We use following *sinc* and sinusoidal pulses to study the effect of decay rate on the bilinear approximation properties:

$$f_1(t) \quad \sim \quad \begin{cases} \sin(20t), & 0 \leq t < 1 \\ 0, & \text{otherwise} \end{cases} \tag{5.12}$$

$$f_2(t) \quad \sim \quad \begin{cases} sinc(20t), & 0 \leq t < 1 \\ 0, & \text{otherwise} \end{cases} \tag{5.13}$$

A value of $a = 20$ is used to compute all bilinear expansions.

Figures (5-12) and (5-13) show the sorted bilinear coefficients and partial sum sequences, respectively. As seen, the approximation performance is much better for the *sinc* pulse, which decays as $\frac{1}{t}$, than for the sinusoidal pulse, which does not decay.

However, when using $a = 20$ for the bilinear expansions, the approximation performance shown in Figures (5-12) and (5-13) is worse than that for any of the rational Laplace transforms considered in Section 5.4. This indicates that an exponential decay rate is preferable over a polynomial one.
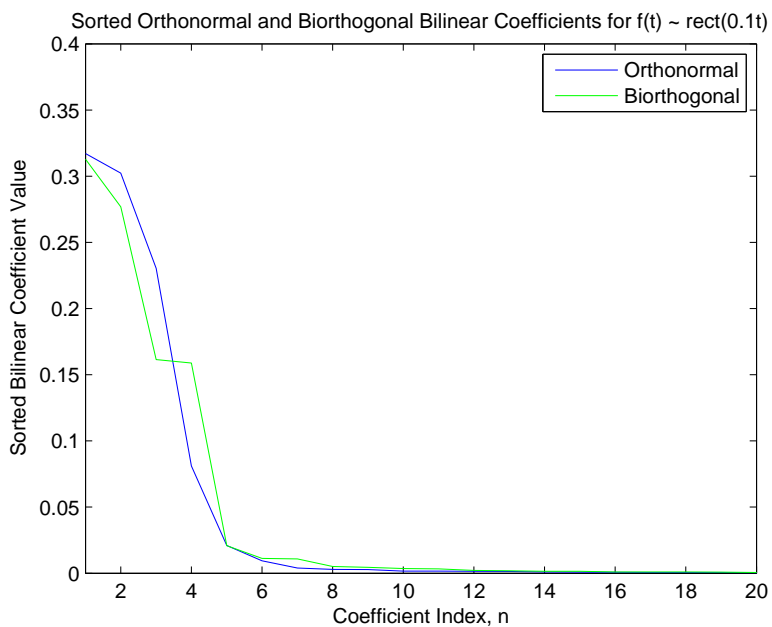
(a) Sorted Bilinear Coefficients
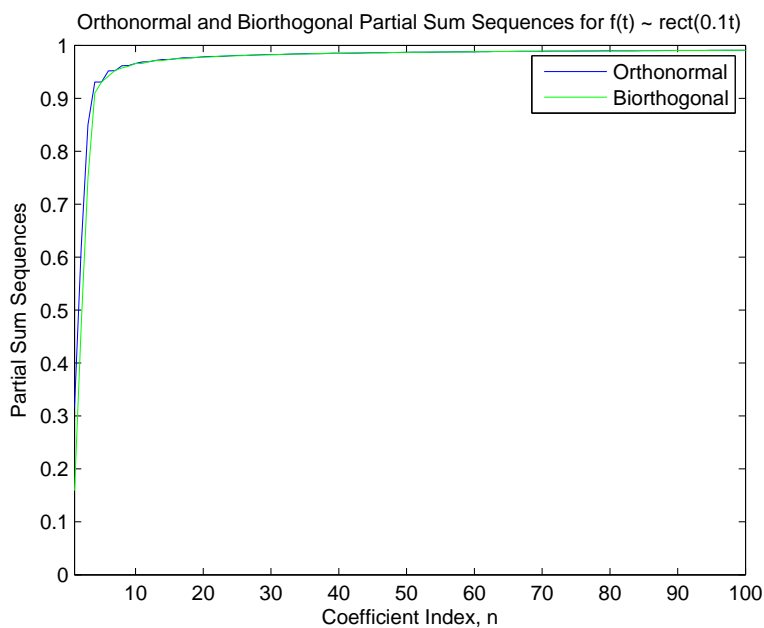
(b) Partial Sum Sequences

Figure 5-11: Sorted Coefficients and Partial Sum Sequences for Rectangular Pulse, $a = 62.8$
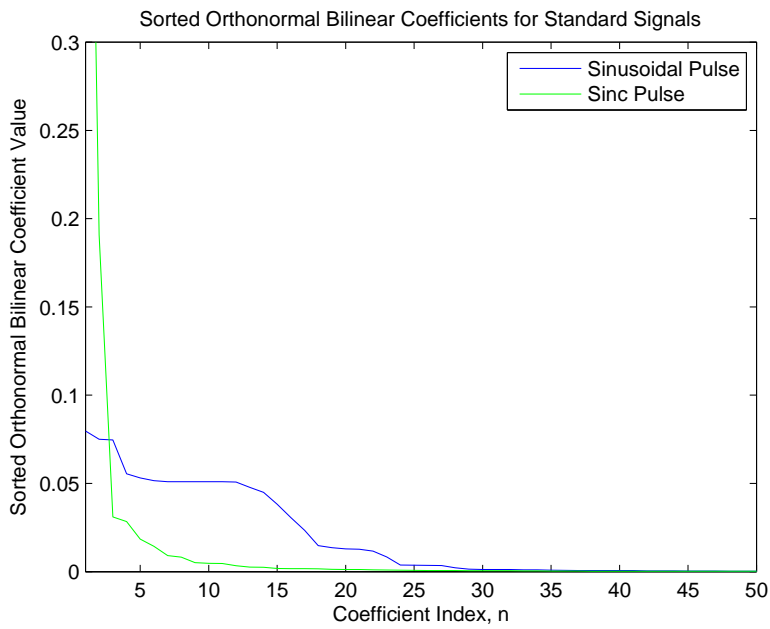
(a) Orthonormal Expansion Coefficients
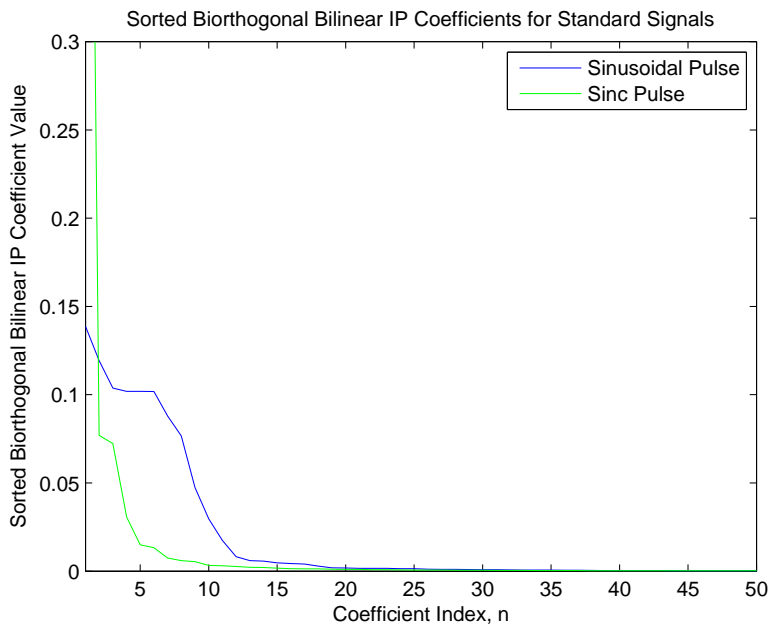
(b) Biorthogonal Inner Product Coefficients

Figure 5-12: Sorted Bilinear Coefficients for $f_1(t)$ and $f_2(t)$
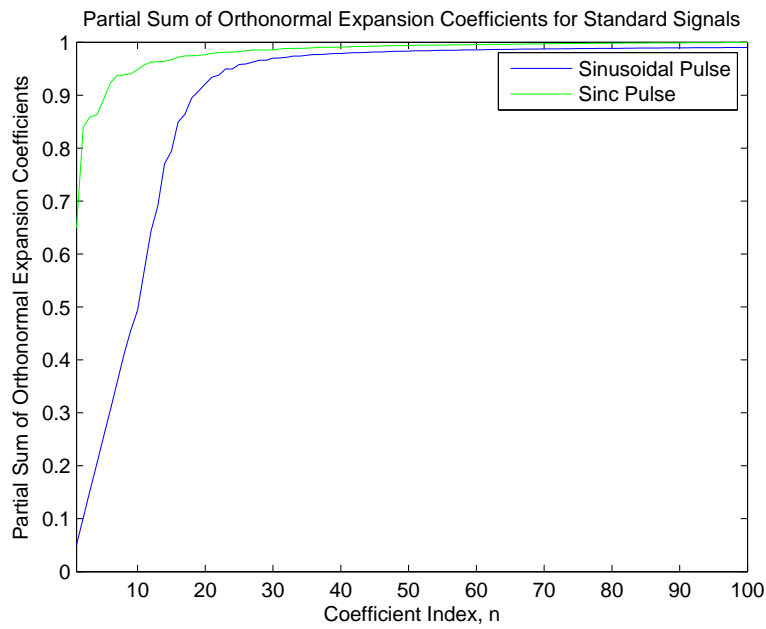
(a) Orthonormal Expansion Coefficients
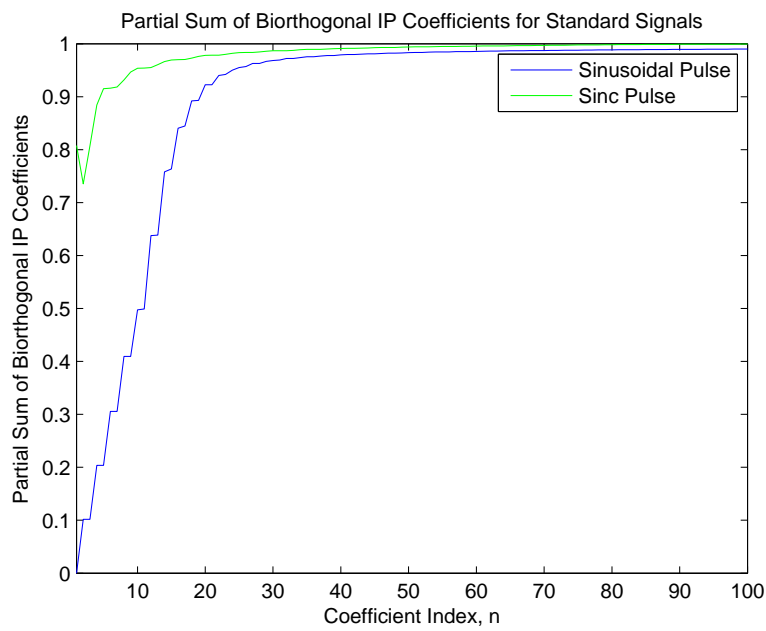
(b) Biorthogonal Inner Product Coefficients

Figure 5-13: Partial Sum Sequences for $f_1(t)$ and $f_2(t)$

5.6 Summary

The results presented in this chapter provide a number of key insights into the bilinear approximation properties.

As described in Section 5.2, the parameter a plays an important role in determining the group delay $\tau_g(\omega)$ of the all-pass filters in Figures (2-3) and (2-9). We suggest initializing the value of a to the maximum frequency of interest in order to reduce the number of significant expansion terms.

From Section 5.3, signals which can be exactly represented using a finite number of bilinear basis functions must have rational Laplace transforms with all poles located at $s = -a$. Section 5.3 shows that rational transforms with poles close to $s = -a$ are well-approximated using the bilinear expansions. However, the performance worsens as the poles move away from this location, both along the real axis as well as perpendicular to it.

Section 5.5 investigates general signal characteristics which impact the approximation performance. Due to the behavior of $\lambda_n(t)$ and $\phi_n(t)$, the bilinear representations are best-suited to signals with their energy concentrated near the time origin. Furthermore, the presence of isolated discontinuities results in a slow growth of the sequences $S_{ON}[M]$ and $S_{BiO}[M]$. This translates into large reconstruction errors around the discontinuities. The approximation is also sensitive to the decay rate. In general, signals with an exponential decay are preferred to those which do not decay or which have a polynomial decay.

We conclude this chapter by noting that, from Figures (5-3) through (5-13), the approximation performance of the orthonormal and the biorthogonal representations are very similar.

In fact, the main difference between the two expansions seems to be the overall implementation. Namely, for the orthonormal expansion, we need to consider only the relative magnitudes of the expansion coefficients to determine the index set I_M. However, for the biorthogonal representation, we need both the expansion coefficients $f[n]$ and a sequence of secondary coefficients $b_f[n]$ to select the significant indices. Not only does the nonlinear approximation become more complicated, but additional hardware is required to compute the second set of bilinear coefficients.

Chapter 6

The Windowed Bilinear Representation

This chapter explores a modified bilinear representation in which we segment the original CT signal into finite-duration blocks and compute the expansion of each block separately. Mathematically, we treat the original CT signal as a sum of segments according to

$$f(t) = \sum_{k=0}^{\infty} f_k(t - kT) \tag{6.1}$$

$$f_k(t) = f(t + kT)w(t) \tag{6.2}$$

such that the finite-duration window function, $w(t)$, satisfies

$$\sum_k w(t - kT) = 1, \ \forall t \tag{6.3}$$

An example of this representation is shown pictorially in Figure (6-1).
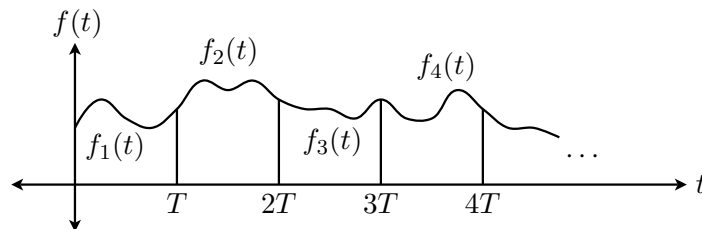
Figure 6-1: Segmenting the Original CT Signal using a Non-Overlapping Window.

There are many reasons for investigating the windowed bilinear representation. From an approximation perspective, we are most interested in the potential time resolution that it provides. Namely, since the amount of energy present in a signal often varies considerably over time, it may be possible to achieve a lower approximation error by allocating more expansion terms to segments with a lot of signal energy at the expense of those segments with less signal content.

Also, from an implementation perspective, this representation allows us to control the latency when computing the bilinear expansion. This is important considering that the input to the first-order cascades in Figures (2-3) and (2-9) is the time-reversed signal $f(-t)$. Therefore, we must obtain and store the entire CT signal before computing its expansion coefficients. Depending on the signal duration, the associated latency may become much longer than desired.

Section 6.1 summarizes the importance of the function $w(t)$ in Equation (6.2) and presents the window choices used for each of the applications in Chapters 7-9. Section 6.2 outlines the relationship between the original and the windowed bilinear representations. In Section 6.3 we examine the approximation properties of this representation as it applies to both the binary detection and the audio approximation applications. We will see that the windowed representation affords certain advantages for each application.

6.1   The Window Function $w(t)$

The choice of window depends on both the particular application as well as the bilinear approximation properties. As seen in Section 5.5, the bilinear representation is sensitive to discontinuities, the energy distribution over time and the signal decay rate. In contrast, the window function is constrained by Equation (6.3). Therefore, we must balance several factors in selecting an appropriate $w(t)$.

When computing inner products for the binary detection application, we consider only the rectangular window

$$w_R(t) = \begin{cases} 1, & 0 \le t < T \\ 0, & \text{otherwise} \end{cases} \qquad (6.4)$$

The primary reason for this choice is to maintain simplicity. Namely, since the resulting segments do not overlap in time, we can just sum the inner products of individual segments to compute the desired quantity. Furthermore, under our assumption of additive white Gaussian noise (see Chapter 8), the noise remains uncorrelated between segments. This means that we do not complicate our overall detection problem.

The rectangular window also has an advantage in terms of its approximation performance. For a given value of T in Equation (6.1), the rectangular window has the shortest segment duration. As explained in Chapter 5, short-duration signals often have fewer significant expansion coefficients which translates to a better approximation.

For the audio approximation application in Chapter 7, we will compare the performance of a rectangular window with that of a Bartlett triangular window and a raised cosine window with 50 percent overlap. Mathematically, these windows can be expressed

$$
w_B(t) \;=\; \begin{cases} \frac{1}{T}t, & 0 \le t < T \\ 2 - \frac{1}{T}t, & T \le t < 2T \\ 0, & \text{otherwise} \end{cases} \tag{6.5}
$$

$$
w_C(t) \;=\; \begin{cases} 1, & 0 \le |t - T| < \frac{T}{4} \\ 0.5\left(1 + \cos\left(\frac{2\pi}{T}\left(|t - T| - \frac{T}{4}\right)\right)\right), & \frac{T}{4} \le |t - T| < \frac{3T}{4} \\ 0, & \text{otherwise} \end{cases} \tag{6.6}
$$

The rectangular, Bartlett and raised cosine windows are depicted in Figure (6-2).
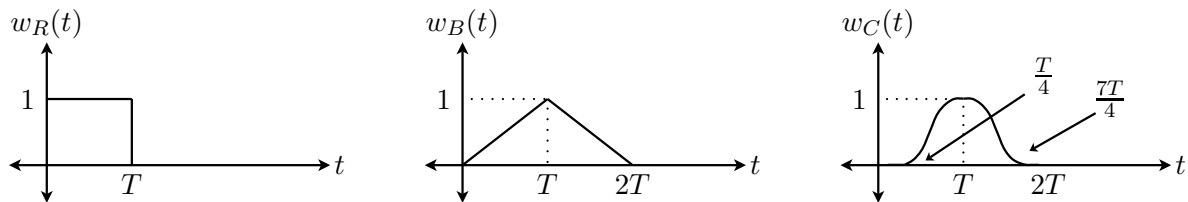
Figure 6-2: Rectangular, Bartlett and Hanning Windows to Segment a CT Signal.

One advantage that the Bartlett and raised cosine windows have over the rectangular one is a smoother transition between consecutive segments. This reduces the effect of boundary discontinuities (see Figure 5-10), which can be perceptually disturbing in the reconstructed signal. A second advantage is that, due to the shapes of $w_B(t)$ and $w_C(t)$, the resulting

segments decay to zero. This is unlike segments generated by the rectangular window, which has unity gain for $0 < t \leq T$. According to Section 5.5 this gradual decay may have a positive impact on the bilinear approximation performance.

The major disadvantages of the Bartlett and raised cosine windows are that the segment durations are longer, and that the signal energy will generally be found near the center of each segment, rather than at the beginning. In contrast, bilinear approximation seems to perform best when the signal energy is concentrated near the time origin. Furthermore, the number of significant coefficients usually increases with the signal duration.

6.2 Relationship to Original Representation

Equation (6.1) leads to a theoretical relationship between the original and the windowed bilinear representations. First, consider the two CT signals shown in Figure (6-3). Specifically, $f_1(t)$ and $f_2(t)$ consist of the same pulse shape located at the origin and at t_o respectively. In the windowed representation $f_2(t)$ corresponds to the actual time segment, but the bilinear coefficients are computed as if it were $f_1(t)$.
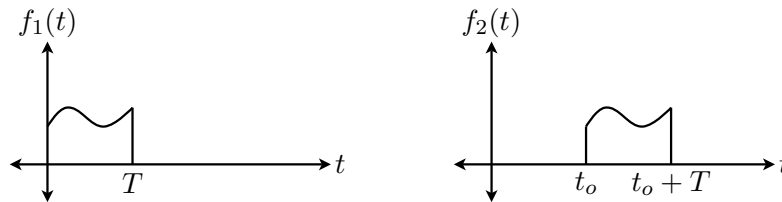
Figure 6-3: Original Continuous-Time Signal and its Shifted Version.

Next, from Chapter 2 that the orthonormal and biorthogonal bilinear frequency-warping relationships are

$$F_{ON}\left(e^{j\Omega}\right) = \frac{\sqrt{2a}}{e^{j\Omega}+1}F\left(ja\tan(\Omega/2)\right) \tag{6.7}$$

$$F_{BiO}\left(e^{j\Omega}\right) = F\left(ja\tan(\Omega/2)\right) \tag{6.8}$$

where $F_{ON}\left(e^{j\Omega}\right)$ and $F_{BiO}\left(e^{j\Omega}\right)$ are the Fourier transforms of the expansion coefficient sequences and Ω is the discrete-time frequency variable.

Using Equations (6.7) and (6.8), the coefficient sequences $f_1[n]$ and $f_2[n]$ are related by

$$F_2\left(e^{j\Omega}\right) = F_1\left(e^{j\Omega}\right)e^{ja\tan(\Omega/2)t_o} \tag{6.9}$$

The above expression is true for both the orthonormal and the biorthogonal representations.

As seen, shifting a CT signal corresponds to a nonlinear phase factor in the DT expansion coefficients. We can extrapolate from Equation (6.9) to express the coefficients of the original signal $f(t)$ in terms of the expansion coefficients of its windowed segments $f_k(t)$, specifically

$$F\left(e^{j\Omega}\right) = \sum_{k=0}^{\infty} F_k\left(e^{j\Omega}\right)e^{ja\tan(\Omega/2)kT} \tag{6.10}$$

Equation (6.10) can also be used to compute the true bilinear expansion coefficients of a CT signal from its windowed representation.

6.3   Approximation Using the Windowed Representation

The following simulations are used to investigate the effect that segmentation has on the bilinear approximation properties. We first examine the performance when using a rectangular window to segment the CT signal, in the context of binary detection. Then we compare the performances of segmenting with a rectangular, a Bartlett triangular and a raised cosine window, as they would apply to the audio approximation problem.

The following terminology denotes the three linear and nonlinear approximation methods employed in this section:

Linear The first M coefficients are retained from each segment.

Nonlinear 1 The M largest coefficients are retained from each segment.

Nonlinear 2 The largest coefficient is selected from each segment. Then, for the remaining, the largest coefficients overall are kept.

All results presented in this section are based on the class of signals

$$f(t) \sim \begin{cases} \text{sinc}(p(t-0.5)), & 0 \le t < 1 \\ 0, & \text{otherwise} \end{cases} \tag{6.11}$$

69

Since the energy of a *sinc* function is largely concentrated around its main lobe, it is representative of a signal whose energy content varies considerably over time. All signals are normalized to have unit energy.

6.3.1   Segmenting with a Rectangular Window

As discussed in Chapter 8, our objective in the binary detection application is to capture the maximum amount of energy from the original CT signal for a fixed number of DT coefficients. Therefore, if I_n represents the set of retained indices in segment n, then our error metrics become

$$\delta_{ON} = \int_0^\infty f^2(t)dt - \sum_{n=1}^N \sum_{k \in I_n} f_n^2[k] \tag{6.12}$$

$$\delta_{BiO} = \int_0^\infty f^2(t)dt - \sum_{n=1}^N \sum_{k \in I_n} IP_n[k] \tag{6.13}$$

The data presented in this section is based on the signal $f(t)$ from Equation (6.11) with $p = 100$. The bilinear representations are calculated using $a = p = 100$.

No. of DT Coefficients	Window Duration, T	Approximation Type		
		Linear	*Nonlinear 1*	*Nonlinear 2*
50	Original	0.6840	0.4567	——
	0.2 *sec*	0.6832	0.4532	0.0323
	0.25 *sec*	0.5088	0.4156	0.3044
	0.34 *sec*	0.6533	0.4260	0.0930
	0.5 *sec*	0.5056	0.4062	0.3819
100	Original	0.4487	0.2166	——
	0.2 *sec*	0.4487	0.2319	0.0078
	0.25 *sec*	0.4274	0.3474	0.1822
	0.34 *sec*	0.4234	0.1871	0.0102
	0.5 *sec*	0.4243	0.3412	0.2812
200	Original	0.1588	0.0231	——
	0.2 *sec*	0.1089	0.0422	0.0031
	0.25 *sec*	0.3559	0.2478	0.1014
	0.34 *sec*	0.1032	0.0322	0.0028
	0.5 *sec*	0.3568	0.2455	0.1663

Table 6.1: δ_{ON} for $f(t) \sim \text{sinc}(100(t - 0.5))$

Table (6.1) shows the orthonormal bilinear approximation performance for different rectangular window sizes and each of the three approximation techniques.

There are two main points to note from this data. First, in many cases the segmented representation achieves a lower error than the original bilinear representation when using the Nonlinear 2 approximation technique. This can be attributed to the increased time resolution, since more coefficients are allotted to the segment(s) containing the main lobe of the *sinc* function. The improvement in performance becomes especially pronounced as the total number of DT coefficients decreases.

The second point is that the approximation performance for window durations $T = 0.25, 0.5$ is notably poorer than for the other two window lengths. This is because these values of T divide the main lobe in half, meaning that one segment will contain a rapidly-increasing signal with a large amount of energy. From Section 5.5, as the signal energy moves farther from the time origin, the number of coefficients needed to represent it increases. In contrast, window durations of $T = 0.2, 0.34$ capture the entire main lobe in a single segment. This has the advantages of isolating most of the energy in one segment and of requiring fewer coefficients to represent. Notice, however, that any segment duration outperforms the original representation as the number of coefficients decreases to 50.

Table (6.2) shows the biorthogonal approximation performance for different rectangular window sizes and each of the three approximation techniques.

No. of DT Coefficients	Window Duration, T	Approximation Type		
		Linear	*Nonlinear 1*	*Nonlinear 2*
50	Original	0.9933	0.9913	——
	0.2 *sec*	0.6795	0.4651	0.0356
	0.25 *sec*	0.5163	0.3346	0.2242
	0.34 *sec*	0.6730	0.4517	0.0979
	0.5 *sec*	0.5071	0.3300	0.3034
100	Original	0.9916	0.9902	——
	0.2 *sec*	0.4449	0.2149	0.0063
	0.25 *sec*	0.4291	0.2657	0.1039
	0.34 *sec*	0.4163	0.2102	0.0103
	0.5 *sec*	0.4252	0.2637	0.2043
200	Original	0.9902	0.9897	——
	0.2 *sec*	0.1287	0.0492	0.0015
	0.25 *sec*	0.3563	0.1685	0.0278
	0.34 *sec*	0.1073	0.0307	0.0028
	0.5 *sec*	0.3578	0.1690	0.0909

Table 6.2: δ_{BiO} for $f(t) \sim \text{sinc}(100(t-0.5))$

The most striking result is the vast performance difference between the original (un-segmented) representation and the windowed representation. Once again, the greatest gain from segmentation is realized when using the Nonlinear 2 approximation technique. However, in this case, the windowed representation achieves a lower error for *any* of the three methods. A possible reason for this behavior is that the infinite-duration *sinc* function does not fall in the class of signals which can be represented using the biorthogonal expansion since $\int_0^\infty t \cdot sinc^2(t - 0.5)dt \to \infty$. In contrast, when the *sinc* is windowed into finite-duration blocks, each segment can individually be represented using the primal basis functions $\phi_n(t)$.

Finally, notice that the performance when using window durations of $T = 0.25, 0.5$ is notably poorer than for the other two window lengths. Once again, this is because the main lobe is divided into two parts, so the segment with a rapidly-increasing signal requires a large number of DT coefficients to represent. Nevertheless, even this performance degradation is preferable to using the original representation.

From Tables (6.1) and (6.2) we conclude that a much better approximation performance can be realized by segmenting the CT signal using a rectangular window and employing the Nonlinear 2 technique.

Another noteworthy observation is that the performance, as measured by δ_{ON} and δ_{BiO}, of the windowed orthonormal and the windowed biorthogonal representations are fairly similar. This is in accordance with the results seen in Chapter 5. However, the original orthonormal and the original biorthogonal representations differ drastically in performance. This indicates that the representations behave similarly for only a specific class of signals. A precise characterization of this class is left to future study.

6.3.2 Comparison of a Rectangular, Bartlett and Raised Cosine Window

In the audio approximation problem (see Chapter 7), our goal is to achieve a representation which is as close as possible to the original CT signal, as measured by the squared reconstruction error, for a fixed number of DT coefficients. Therefore, if I_n represents the set of retained indices in segment n, then our error metric is

$$\epsilon = \int_0^\infty \left(f(t) - \sum_{n=1}^{N} \sum_{k \in I_n} f_n[k] \lambda_k(t - nT) \right)^2 dt \qquad (6.14)$$

72

We limit ourselves to the orthonormal representation for this application.

The data presented in this section is based on the signal $f(t)$ from Equation (6.11) with $p = 50$. The bilinear expansion coefficients and reconstructions are computed using $a = p = 50$. We consider a lower frequency *sinc* in this section to avoid the dynamic range issue, discussed in Section 4.3. As an added precaution, only the first 100 basis functions are generated during synthesis. However, this does not impact the approximation results.

Tables (6.3), (6.4) and (6.5) show the reconstruction errors when using different rectangular, Bartlett and raised cosine window sizes for each of the three approximation techniques. From Figure (6-2) the rectangular window duration is equal to the shift T, the Bartlett window duration is $2T$, and the effective raised cosine window duration is $1.5T$.

On average, the rectangular window achieves the lowest reconstruction error, followed by the raised cosine window, which has the second-lowest error. This is true regardless of the approximation technique used. There are two factors which contribute to this trend.

First, for a given window shift T, the rectangular window has the shortest duration, and the raised cosine window has the next-shortest duration. As previously discussed, higher order basis functions are needed to represent longer duration signals. Since this often translates to a slower decay of sorted coefficients, the rectangular window has an advantage in terms of its approximation properties.

Second, for a given value of T, the Bartlett and raised cosine windows require an additional segment relative to the rectangular window. The extra segment confers a disadvantage because the same number of DT coefficients is being used to represent, not only longer duration blocks, but a greater number of blocks as well. One point to note is that, as the number of DT coefficients increases, the effect of this additional segment should become less and less significant.

Although the overlapping windows have some drawbacks when minimizing the squared reconstruction error, the resulting approximations have better perceptual quality. This is due to the smoother transition between subsequent blocks which eliminates artificial discontinuities between segments. The effect of such discontinuities is illustrated in Figure (5-10). This issue is discussed further in Chapter 7.

We can use Tables (6.3), (6.4) and (6.5) to compare the windowed bilinear representations with the original. As seen, the Nonlinear 2 approximation technique often achieves a lower

reconstruction error for the same number of DT coefficients. This is true for any of the three window types with appropriate choice of the parameter T. The enhanced performance is attributed to the increased time resolution which comes from windowing the CT signal. In this particular case, more coefficients are used for the segment(s) containing the main lobe of the *sinc* function, thus reducing the total squared error.

As a final comment, the windowed representations offer an additional benefit, specific to the MATLAB implementation discussed in Chapter 4. Namely, having shorter duration signals increases the number of basis functions that can be generated before encountering the dynamic range issue of Section 4.3. Therefore, segmentation makes it possible to accurately reconstruct the audio signals in the following chapter.

No. of DT Coefficients	Window Shift, T	Approximation Type		
		Linear	Nonlinear 1	Nonlinear 2
13	Original	0.9598	0.6033	——
	0.167 sec	0.6276	0.5259	0.4012
	0.20 sec	0.9931	0.6446	0.2879
	0.25 sec	0.5706	0.4786	0.4042
	0.34 sec	0.9730	0.5994	0.2854
	0.50 sec	0.5389	0.4570	0.4570
25	Original	0.6744	0.3768	——
	0.167 sec	0.6071	0.4210	0.1942
	0.20 sec	0.6907	0.3687	0.0582
	0.25 sec	0.5326	0.3866	0.2508
	0.34 sec	0.6614	0.3399	0.0833
	0.50 sec	0.5161	0.4151	0.3805
50	Original	0.4355	0.2000	——
	0.167 sec	0.4427	0.2826	0.0861
	0.20 sec	0.4350	0.1484	0.0143
	0.25 sec	0.4117	0.2748	0.1233
	0.34 sec	0.4553	0.1278	0.0173
	0.50 sec	0.3892	0.3255	0.2856
75	Original	0.2834	0.1533	——
	0.167 sec	0.3556	0.2083	0.0612
	0.20 sec	0.1951	0.062	0.0073
	0.25 sec	0.3530	0.2060	0.0841
	0.34 sec	0.2105	0.0655	0.0075
	0.50 sec	0.3408	0.2856	0.2335

Table 6.3: ϵ when using a Rectangular window for $f(t) \sim \text{sinc}(50(t - 0.5))$

No. of DT Coefficients	Window Shift, T	Approximation Type		
		Linear	*Nonlinear 1*	*Nonlinear 2*
13	Original	0.9598	0.6033	——
	0.167 *sec*	0.9864	0.8731	0.8731
	0.20 *sec*	0.9957	0.7063	0.4769
	0.25 *sec*	0.9842	0.8248	0.6130
	0.34 *sec*	0.9984	0.7229	0.5708
	0.50 *sec*	0.9917	0.8070	0.6724
25	Original	0.6744	0.3768	——
	0.167 *sec*	0.9775	0.6957	0.2086
	0.20 *sec*	0.7796	0.5700	0.2645
	0.25 *sec*	0.9793	0.6622	0.2293
	0.34 *sec*	0.8181	0.5709	0.3802
	0.50 *sec*	0.9885	0.7029	0.4407
50	Original	0.4355	0.2000	——
	0.167 *sec*	0.7272	0.4314	0.0285
	0.20 *sec*	0.6219	0.3211	0.0960
	0.25 *sec*	0.7461	0.4634	0.0422
	0.34 *sec*	0.6662	0.3747	0.2022
	0.50 *sec*	0.8150	0.5263	0.2085
75	Original	0.2834	0.1533	——
	0.167 *sec*	0.5748	0.2781	0.0160
	0.20 *sec*	0.4441	0.2194	0.0334
	0.25 *sec*	0.5855	0.3015	0.0175
	0.34 *sec*	0.5028	0.2402	0.1192
	0.50 *sec*	0.6616	0.3717	0.1606

Table 6.4: ϵ when using a Bartlett triangular window for $f(t) \sim \mathrm{sinc}(50(t - 0.5))$

No. of DT Coefficients	Window Shift, T	Approximation Type		
		Linear	*Nonlinear 1*	*Nonlinear 2*
13	Original	0.9598	0.6033	——
	0.167 *sec*	1.000	0.8518	0.8518
	0.20 *sec*	0.8450	0.6599	0.4011
	0.25 *sec*	0.9999	0.7980	0.5803
	0.34 *sec*	0.8315	0.6260	0.5239
	0.50 *sec*	0.9999	0.7863	0.6031
25	Original	0.6744	0.3768	——
	0.167 *sec*	0.9719	0.6443	0.1225
	0.20 *sec*	0.6033	0.4307	0.1775
	0.25 *sec*	0.9533	0.6259	0.1418
	0.34 *sec*	0.7142	0.4686	0.3216
	0.50 *sec*	0.9976	0.6567	0.3031
50	Original	0.4355	0.2000	——
	0.167 *sec*	0.6109	0.3016	0.0196
	0.20 *sec*	0.3952	0.2273	0.0549
	0.25 *sec*	0.6790	0.3460	0.0218
	0.34 *sec*	0.4647	0.2784	0.1216
	0.50 *sec*	0.7371	0.4439	0.0969
75	Original	0.2834	0.1533	——
	0.167 *sec*	0.5326	0.2011	0.0118
	0.20 *sec*	0.2861	0.1494	0.0204
	0.25 *sec*	0.5225	0.1933	0.0104
	0.34 *sec*	0.3248	0.1793	0.0520
	0.50 *sec*	0.5866	0.2483	0.0337

Table 6.5: ϵ when using a Raised Cosine window for $f(t) \sim \text{sinc}(50(t - 0.5))$

Chapter 7

Approximation of Audio Signals

In Chapters 5 and 6 we discussed the bilinear approximation properties in the context of various synthetic waveforms. In this chapter we use the orthonormal bilinear representation to approximate audio signals. This choice is motivated by the fact that instrumental music can often be represented using decaying harmonic functions, thereby falling into the class of potentially well-approximated signals discussed in Section 5.5.

Section 7.1 of this chapter outlines the experimental details. In Section 7.2 we present the simulation results for two different audio clips. A short discussion of the results is found in Section 7.3.

We consider only the orthonormal representation for this application. This is due to the difficulty in selecting the appropriate subset of biorthogonal expansion coefficients to minimize the approximation error $\epsilon[M]$ in Equation (5.2). Since we desire an approximation which is perceptually similar to the original signal, achieving a close reconstruction seems like a reasonable goal.

7.1 Details of the Simulation Setup

The audio signals used in this experiment are read from *.wav* files, which have been sampled at a rate of $44.1kHz$. Since audio content can vary considerably over time, we segment the signal, using a discrete-time window function, and calculate the expansion for each segment individually. The window functions are DT counterparts of the Rectangular, Bartlett and raised cosine windows presented in Chapter 6.

In order to use the MATLAB analysis approximations, the segments are interpolated

to achieve finer sampling. However, they are reconstructed at $44.1kHz$, so that we can compare them with the original audio signal.

We compare the approximation performance of the bilinear representation with that of a Discrete Cosine Transform (DCT) based representation. Since variants of the DCT are often used in audio compression standards, it provides a reasonable benchmark against which we can evaluate the bilinear representation. In particular, we employ the following orthonormal DCT-IV expansion:

$$X[k] = \sqrt{\frac{2}{N}} \sum_{n=0}^{N-1} x[n] \cos\left(\frac{\pi}{N}(n+1/2)(k+1/2)\right), \ k = 0, \ldots, N-1 \qquad (7.1)$$

$$x[n] = \sqrt{\frac{2}{N}} \sum_{n=0}^{N-1} X[k] \cos\left(\frac{\pi}{N}(n+1/2)(k+1/2)\right), \ n = 0, \ldots, N-1 \qquad (7.2)$$

In the above expressions, $x[n]$ is the original DT signal, $X[k]$ is its DCT-IV coefficients, and N denotes the total number of (uninterpolated) samples in each windowed segment.

We implement the 'Nonlinear 1' and 'Nonlinear 2' approximation techniques from Section 6.3 in order to reduce the (total) number of bilinear or DCT coefficients.

In the Nonlinear 1 method we retain an equal number of coefficients from each segment. In the Nonlinear 2 method we retain the largest coefficient in each segment and, for the remaining ones, select the largest coefficients over all blocks. The goal of this method is to achieve greater accuracy in regions with more signal content at the expense of regions that have less signal energy.

7.2 Simulation Results

The bilinear and DCT representations are used to approximate two distinct .*wav* files. The first audio clip features a piano playing smooth and flowing music, which is accentuated by a few contrasting notes. The second clip consists of a violin playing a fast-paced country tune with frequent changes in pitch. Based on the frequency content of each .*wav* file, a value of $a = 8820$ is chosen for the piano music, and a value of $a = 14700$ is used for the violin music.

In order to quantitatively compare the bilinear and the DCT approximation performance, we look at the reconstruction error $\epsilon[M]$ from Equation (5.2), normalized by the original signal energy. We refer to this quantity as the Normalized Squared Error (NSE). Although this metric does not necessarily predict the perceptual quality of each approximation, it is useful to observe because we consciously select coefficients to minimize $\epsilon[M]$.

The NSE for the piano and violin clips are given in Tables (7.1) and (7.2), respectively. The 'DT Coefficient Retention' column describes the total number of (bilinear or DCT) expansion coefficients used in the approximation relative to the number of samples in the original *.wav* clip. To avoid the synthesis problems discussed in Chapter 4, the bilinear reconstructions include only the first 100 expansion coefficients. While this does not impact the 10% and 20% approximations, it does affect the minimum NSE that can be achieved using the bilinear representation.

Window Function	Representation	DT Coefficient Retention	Approximation Type	
			Nonlinear 1	*Nonlinear 2*
Rectangular	Bilinear	100/seg	0.00298	——
		20% of total	0.00497	0.00414
		10% of total	0.03493	0.02095
	DCT-IV	100%	~ 0	——
		20% of total	0.00435	0.00258
		10% of total	0.00888	0.00652
Bartlett	Bilinear	100/seg	0.00189	——
		20% of total	0.00565	0.00424
		10% of total	0.06259	0.03787
	DCT-IV	100%	~ 0	——
		20% of total	0.00080	0.00062
		10% of total	0.00682	0.00424
Raised Cosine	Bilinear	100/seg	0.00119	——
		20% of total	0.00299	0.00220
		10% of total	0.03944	0.02278
	DCT-IV	100%	~ 0	——
		20% of total	0.00089	0.00066
		10% of total	0.00821	0.00513

Table 7.1: Normalized Reconstruction Error for the Piano Sound Clip, $a = 8820$

Figures (7-1) and (7-2) depict the normalized errors, $f(t) - \hat{f}_M(t)$, for each sound clip, while Figures (7-3) and (7-4) show plots of the original and approximated signals for a single windowed segment. Only the Nonlinear 1 approximations are displayed since the Nonlinear 2 performance is qualitatively very similar.

Window Function	Representation	DT Coefficient Retention	Approximation Type	
			Nonlinear 1	Nonlinear 2
Rectangular	Bilinear	100/seg	0.05478	——
		20% of total	0.08967	0.08375
		10% of total	0.23854	0.19333
	DCT-IV	100%	~ 0	——
		20% of total	0.01327	0.01045
		10% of total	0.05375	0.04468
Bartlett	Bilinear	100/seg	0.12653	——
		20% of total	0.17513	0.16905
		10% of total	0.30930	0.26610
	DCT-IV	100%	~ 0	——
		20% of total	0.02656	0.02222
		10% of total	0.07687	0.06724
Raised Cosine	Bilinear	100/seg	0.09000	——
		20% of total	0.13164	0.12508
		10% of total	0.26972	0.23044
	DCT-IV	100%	~ 0	——
		20% of total	0.03173	0.02671
		10% of total	0.09148	0.07975

Table 7.2: Normalized Reconstruction Error for the Violin Sound Clip, $a = 14700$

7.3 Discussion

We use two criteria to analyze each of the approximations: the NSE and the perceptual quality of the reconstructed signal.

We see from Tables (7.1) and (7.2) that the DCT-IV representation, in general, achieves 5-10X lower NSE than the bilinear representation for the same window function, number of coefficients and approximation type. This observation is further supported by comparing the dynamic range of the normalized errors for the bilinear and the DCT-IV approximations in Figures (7-1) and (7-2).

In addition, Figures (7-3) and (7-4) indicate that the bilinear representation is not able to capture rapid signal fluctuations. This is evidenced most strikingly from the fact that even the 100-coefficient reconstructions cannot represent the violin music as well as the 20% DCT-IV approximations.

The data from Section 7.2 also suggests that the rectangular window typically has the lowest NSE followed by the raised cosine window. This pattern is very similar to the results presented in Section 6.3.2.

There are some notable differences when listening to each signal approximation, as compared with the NSE. For example, the bilinear approximations sound worst when using a rectangular window. Due to the discontinuities between segments, there is a loud hissing noise present throughout the entire clip. Furthermore, the raised cosine approximations sound the same as the Bartlett ones, and the Nonlinear 1 and Nonlinear 2 approximations are virtually indistinguishable when heard.

The DCT-IV approximations generally sound better than the bilinear ones for a 20% coefficient retention because they are much cleaner and closer to the original. This is especially true for the violin clip, since even the 100-coefficient bilinear reconstructions sound fuzzy. Additionally, the DCT-IV expansion seems more robust because, when gradually reducing the total number of coefficients, distortions become noticeable first in the bilinear representation. This is consistent across window functions and approximation types.

However, as the coefficient retention decreases, the bilinear and DCT-IV representations eventually suffer from different distortions. For the bilinear representation, the fuzzy background noise becomes increasingly louder until it overwhelms any music present. In contrast, the DCT-IV representation starts to lose important high-frequency information, resulting in unpleasant low-frequency harmonics. In these cases, deciding which is the preferred approximation becomes very subjective.

Our conclusion from the above results would suggest that the DCT-IV representation is better at approximating audio signals. Not only do the DCT-IV approximations achieve much lower NSE, but the bilinear basis functions are not well-suited for capturing rapid signal fluctuations. Therefore, using the DCT-IV representation over the bilinear one can lead to a better-sounding approximation.

We may also conclude that, although it achieves a lower NSE in the bilinear case, using a non-overlapping rectangular window results in a poorer-sounding approximation than for either of the two overlapping window choices. This is due to the discontinuities between segments, which produces a fuzzy background noise throughout the approximated clip.
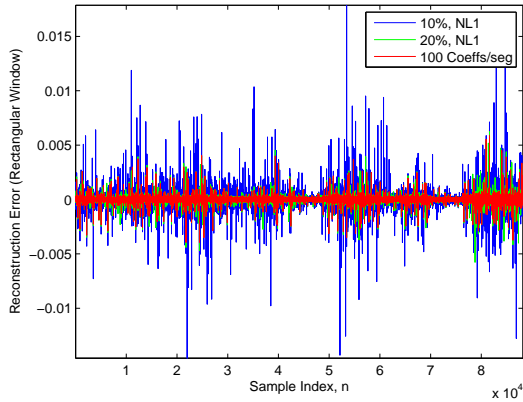
(a) Rectangular Window, Bilinear
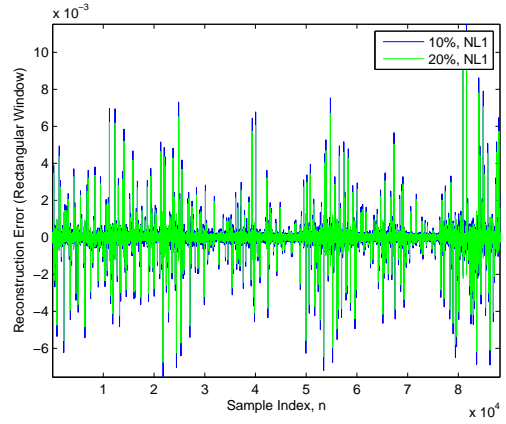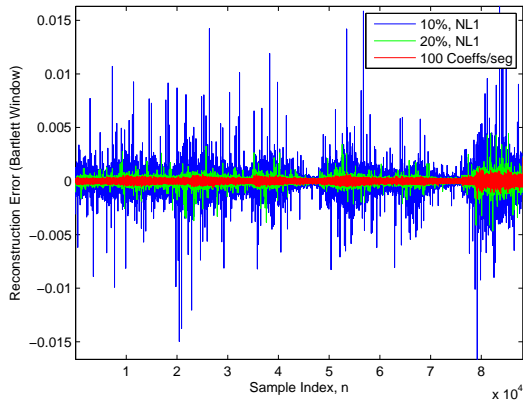
(b) Rectangular Window, DCT

(c) Bartlett Window, Bilinear
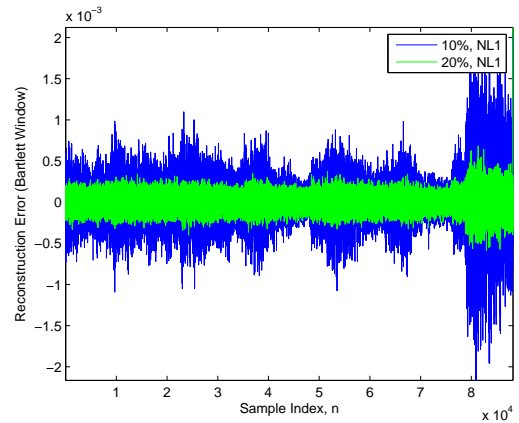
(d) Bartlett Window, DCT
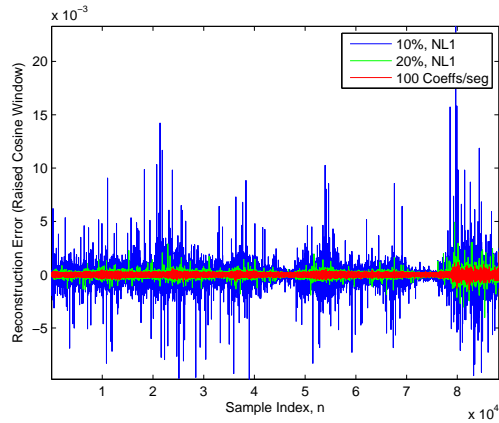
(e) Raised Cosine Window, Bilinear
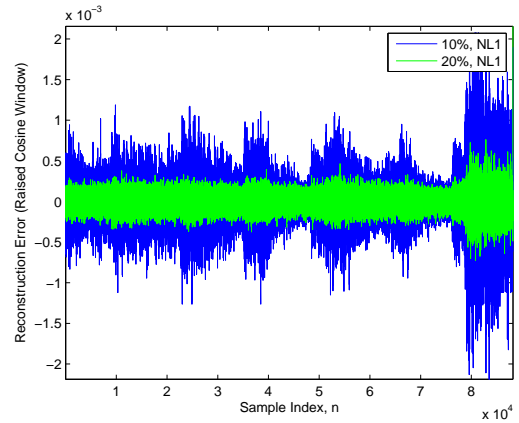
(f) Raised Cosine Window, DCT

Figure 7-1: Normalized Error $f(t) - \hat{f}_M(t)$ for the Piano Sound Clip
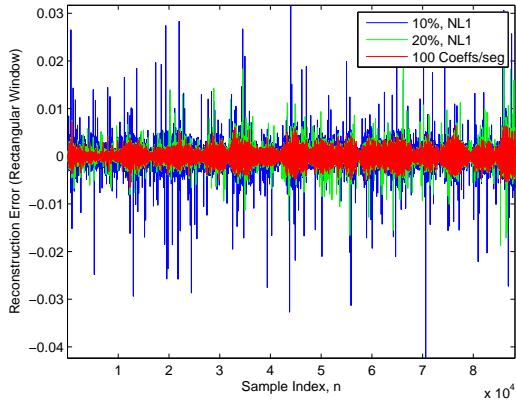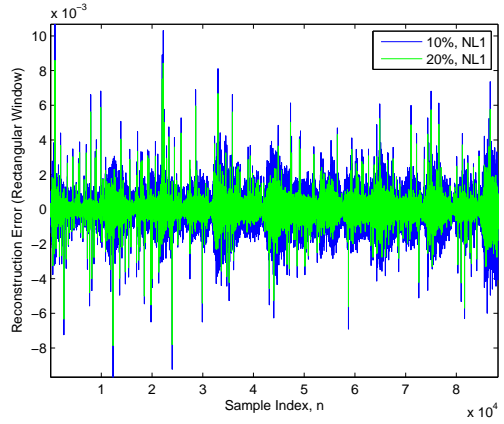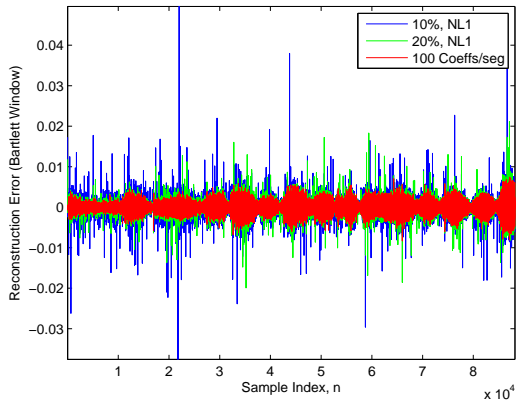
(a) Rectangular Window, Bilinear

(b) Rectangular Window, DCT

(c) Bartlett Window, Bilinear
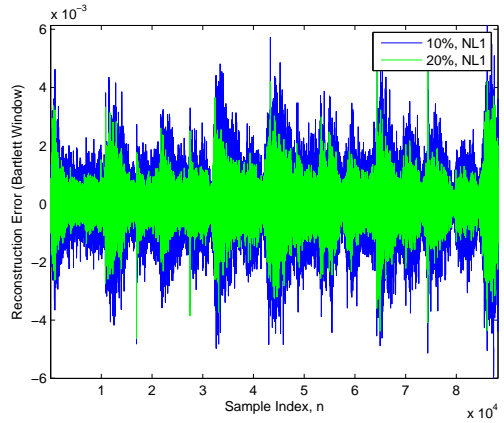
(d) Bartlett Window, DCT
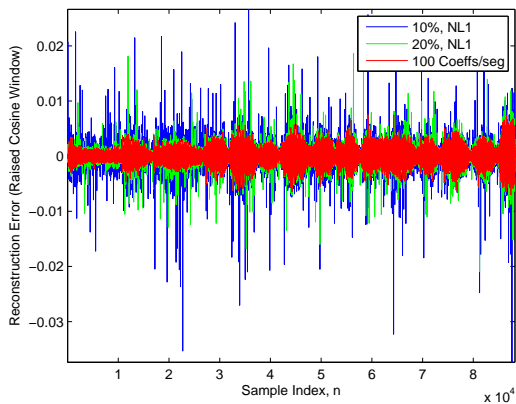
(e) Raised Cosine Window, Bilinear
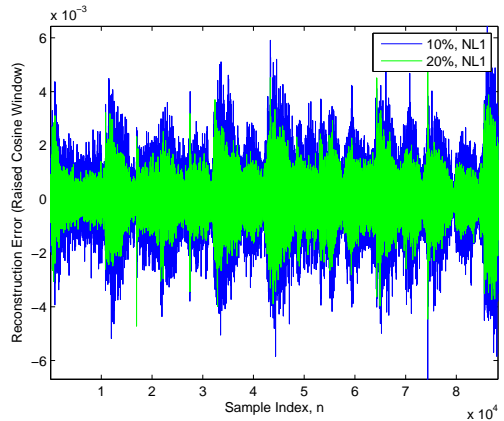
(f) Raised Cosine Window, DCT

Figure 7-2: Normalized Error $f(t) - \hat{f}_M(t)$ for the Violin Sound Clip
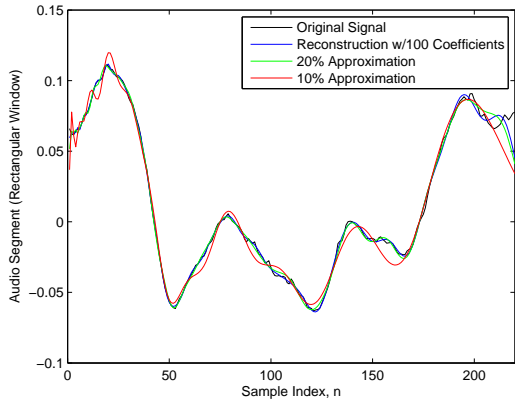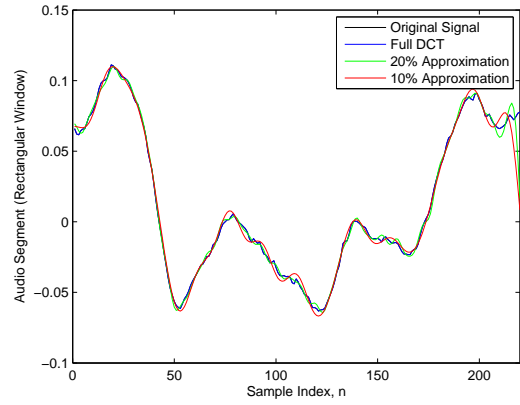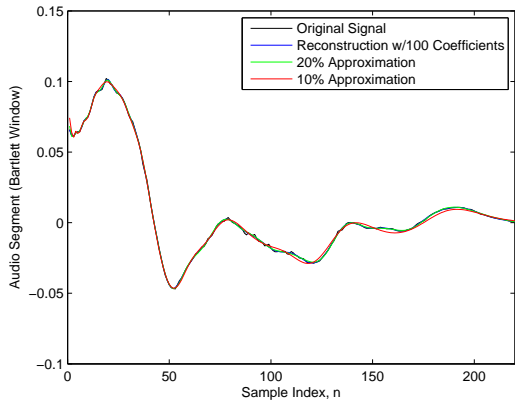
83

(a) Rectangular Window, Bilinear

(b) Rectangular Window, DCT

(c) Bartlett Window, Bilinear
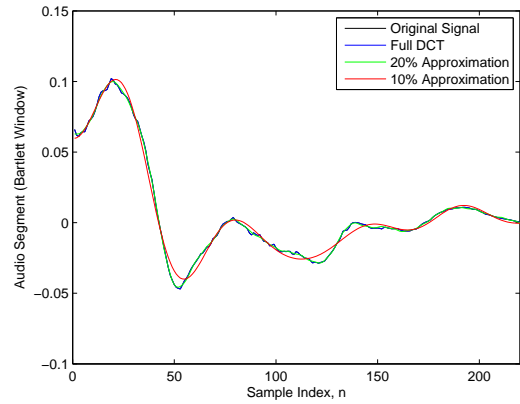
(d) Bartlett Window, DCT
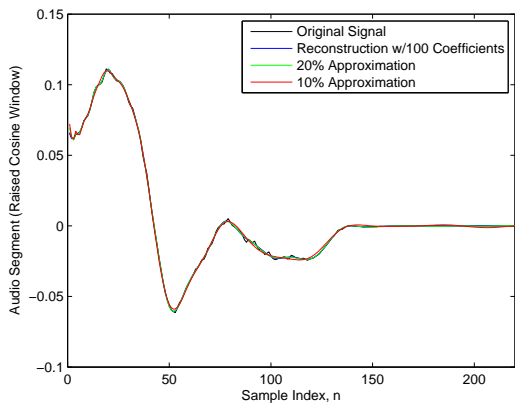
(e) Raised Cosine Window, Bilinear
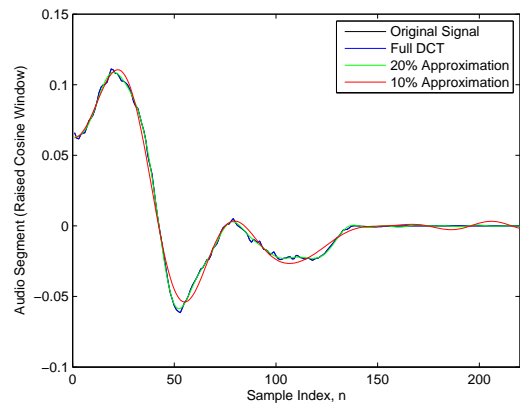
(f) Raised Cosine Window, DCT

Figure 7-3: Reconstructed Audio Segment of a Piano Sound Clip
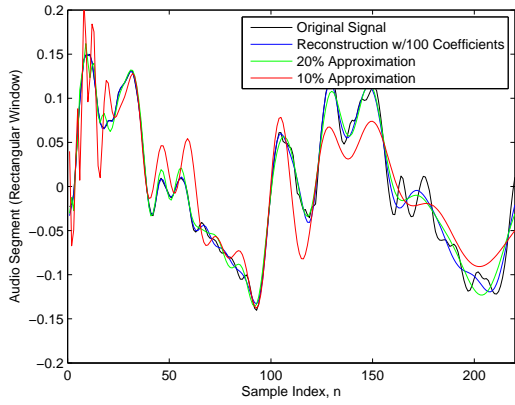
(a) Rectangular Window, Bilinear
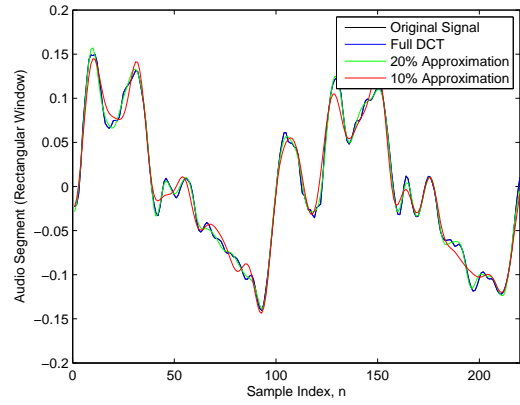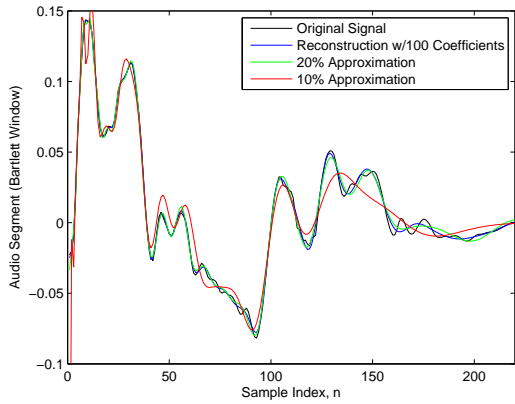
(b) Rectangular Window, DCT

(c) Bartlett Window, Bilinear
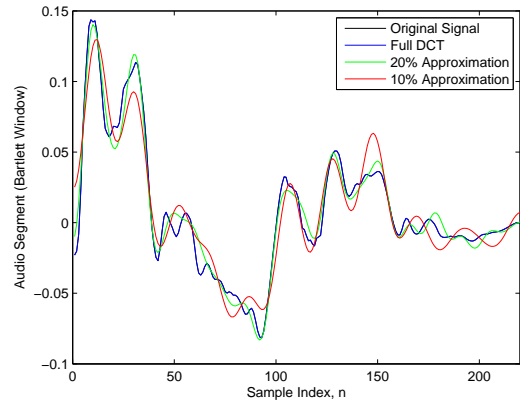
(d) Bartlett Window, DCT
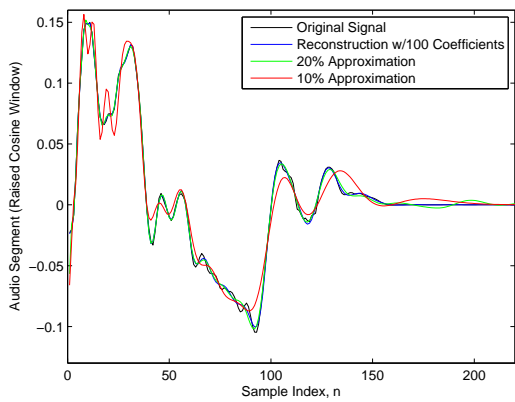
(e) Raised Cosine Window, Bilinear
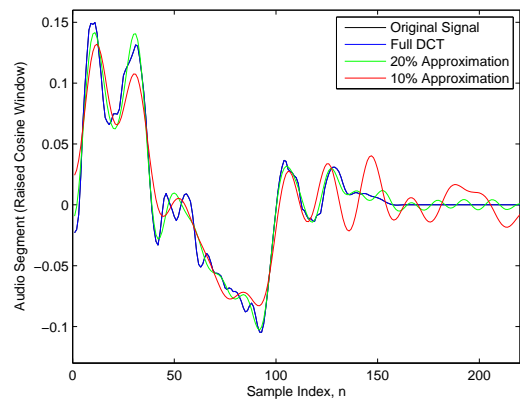
(f) Raised Cosine Window, DCT

Figure 7-4: Reconstructed Audio Segment of a Violin Sound Clip

Chapter 8

The Binary Detection Problem

Chapter 7 focused on an audio approximation problem. We now consider a different type of application, corresponding to binary detection. In this context our goal is to determine whether a desired signal $s(t)$ is present (*Hypothesis 1*, H_1) or absent (*Hypothesis 0*, H_0) by analyzing a noisy received signal $x(t)$. This is depicted pictorially in Figure (8-1).

$$H_0 : r(t) = 0, \; x(t) = \eta(t)$$
$$H_1 : r(t) = s(t), \; x(t) = s(t) + \eta(t)$$

$$\eta(t) \rightarrow \text{zero-mean AWGN, } \sigma_\eta^2$$
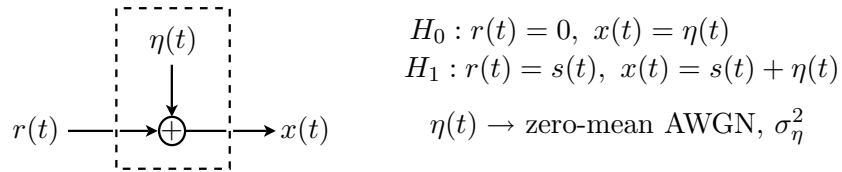
Figure 8-1: Binary detection scenario. The transmitted signal $r(t)$ is corrupted by AWGN. The received signal $x(t)$ consists either of noise or the signal $s(t)$ plus noise.

We assume that $\eta(t)$ is additive white Gaussian noise (AWGN) with a constant power spectrum, $P_\eta(j\omega) = \sigma_\eta^2$. In addition, the value of σ_η^2 does not depend on whether or not $s(t)$ is transmitted. In this case, the well-known decision rule involves comparing the integral of the desired and received signals with a threshold γ. Mathematically,

$$\int_0^\infty x(t)s(t)dt \gtrless \gamma \tag{8.1}$$

where we assume that the desired signal $s(t)$ is real-valued and causal

In theory the left-hand side of Equation (8.1) can be computed using an analog matched filter with impulse response $h(t) = s(-t)$. However, due to the complexity of real-world signals, it is usually difficult and/or impossible to design such a filter. We can circumvent

this problem by expanding the CT signals in a specific basis according to Equation (1.1), and then manipulating the DT expansion coefficients to obtain the integral.

We highlight the relationship between binary detection and signal approximation by further consideration of the random variable $V = \int x(t)s(t)dt$.

It follows from the assumptions on $\eta(t)$ that the integral $\int \eta(t)s(t)dt$ is a zero-mean Gaussian random variable. Therefore, V can be characterized under each hypothesis

$$
\begin{aligned}
H_0 &: \quad V = \int \eta(t)s(t)dt \sim N(0, \sigma_V^2) \\
H_1 &: \quad V = \int s^2(t)dt + \int \eta(t)s(t)dt \sim N(E_V, \sigma_V^2)
\end{aligned}
$$

where $N(\mu, \sigma^2)$ denotes a Gaussian random variable with mean μ and variance σ^2. The bias and variance from the above expressions are

$$
E_V = \int s^2(t)dt \tag{8.2}
$$

$$
\sigma_V^2 = E\left[\int \eta(t)s(t)dt\right]^2 \tag{8.3}
$$

We note that the value of σ_V^2 depends heavily on the expansions used for $x(t)$ and $s(t)$.

The associated detection and error probabilities can be calculated in terms of E_V, σ_V^2 and γ using Gaussian Q-function, $Q(x) = \frac{1}{\sqrt{2\pi}} \int_x^\infty e^{-t^2/2}dt$, as follows:

$$
P_m = Pr\left[error|H_1\right] = Pr\left[V < \gamma|H_1\right] = Q\left(\frac{E_V - \gamma}{\sigma_V}\right) \tag{8.4}
$$

$$
P_d = Pr\left[correct|H_1\right] = Pr\left[V > \gamma|H_1\right] = 1 - Q\left(\frac{E_V - \gamma}{\sigma_V}\right) \tag{8.5}
$$

$$
P_{fa} = Pr\left[error|H_0\right] = Pr\left[V > \gamma|H_0\right] = Q\left(\frac{\gamma}{\sigma_V}\right) \tag{8.6}
$$

$$
P_{cn} = Pr\left[correct|H_0\right] = Pr\left[V < \gamma|H_0\right] = 1 - Q\left(\frac{\gamma}{\sigma_V}\right) \tag{8.7}
$$

From the preceding analysis, the Gaussian distributions under H_0 and H_1 are separated by the bias E_V. Therefore, the larger this quantity, the better our ability to distinguish between the two hypotheses. According to Equation (8.2), for a perfect signal representation, E_V should equal the desired signal energy. However, if we constrain the number of DT expansion coefficients used to compute V, then the application becomes similar to

an approximation problem. The difference is that we would like to capture the maximum amount of energy from $s(t)$, to differentiate between H_0 and H_1, rather than represent the entire signal. This is the rationale behind the metric $\delta[M]$ from Chapters 5 and 6.

In this chapter we analyze the theoretical performance when using different signal representations for binary detection. Section 8.1 is devoted to Nyquist sampling and Section 8.2 explores the orthonormal and the biorthogonal bilinear signal representations. From Equations (8.4) through (8.7), the binary detection performance is largely determined by E_V and σ_V^2. Therefore, our focus is to compute these quantities for each representation. Additional expressions and derivations relevant to this topic can be found in [4], [14] and [10].

8.1 The Nyquist Signal Representation

A commonly-used representation is Nyquist sampling. The CT signal is expressed as

$$f(t) = \sum_{n=-\infty}^{\infty} f(nT) sinc\left(\frac{t}{T} - n\right) \tag{8.8}$$

According to Equation (8.8), the Nyquist basis functions are scaled and shifted *sinc* functions, and the expansion coefficients are equally-spaced time samples of the CT signal.

Using the orthogonality of *sinc* functions, we have the following inner product relationship between two CT signals and their time samples:

$$\int_{-\infty}^{\infty} f(t)g(t)dt = T \sum_{n=-\infty}^{\infty} f(nT)g(nT) \tag{8.9}$$

This relationship will be useful in determining E_V and σ_V^2 for the Nyquist representation.

8.1.1 Ideal (Unconstrained) Nyquist Detection

The Nyquist basis functions span the subspace of finite-energy signals that are bandlimited to $|\omega| \leq \frac{\pi}{T}$. Consequently, in order to compute the integral of Equation (8.1) using this expansion, we assume that the noise power spectrum is flat up to the frequency $\omega_M = \frac{\pi}{T}$ and zero afterwards. Moreover, ω_M must be greater than the effective bandwidth of $s(t)$.

Mathematically,

$$P_\eta(j\omega) = \begin{cases} \sigma_\eta^2, & |\omega| \leq \frac{\pi}{T} \\ 0, & |\omega| > \frac{\pi}{T} \end{cases} \tag{8.10}$$

Equation (8.10) implies that the noise samples $\eta(kT)$ are independent and identically distributed (*i.i.d.*) according to $N(0, \sigma_\eta^2/T)$.

We can now represent the desired signal and noise according to Equation (8.8). From Equation (8.9), it follows that

$$E_V = T \sum_{k=0}^{\infty} s^2(kT) \tag{8.11}$$

$$\sigma_V^2 = \sigma_\eta^2 \left[T \sum_{k=0}^{\infty} s^2(kT) \right] \tag{8.12}$$

The detection and error probabilities can be computed using Equations (8.4) through (8.7).

8.1.2 Constrained Nyquist Detection

If we constrain the maximum number of digital multiplies allowed to compute $\int x(t)s(t)dt$, it may not be possible to use all the Nyquist samples. In this section we consider two methods of reducing the number of samples. The first is to select samples with the largest magnitude. The second is to time alias the Nyquist samples. Again, our focus in each case is to determine E_V and σ_V^2.

Selecting a Subset of Nyquist Samples

According to Chapter 5, we should retain the subset of samples with the largest magnitudes in order to preserve the most signal energy. Since the noise samples are *i.i.d.*, if I denotes the set of selected indices, we can calculate E_V and σ_V^2 by summing over I instead of over all indices. Specifically,

$$E_V = T \sum_{k \in I} s^2(kT) \tag{8.13}$$

$$\sigma_V^2 = \sigma_\eta^2 \left[T \sum_{k \in I} s^2(kT) \right] \tag{8.14}$$

The performance depends on how well the samples in I approximate the energy of $s(t)$.

Time-Aliasing the Nyquist Samples

Another way to restrict the number of multiplications is to time-alias the sample magnitudes. In particular, we replace $s(kT)$ and $\eta(kT)$ with the coefficients $\tilde{s}[k]$ and $\tilde{\eta}[k]$ as defined below:

$$\tilde{s}[k] = \sum_{n=0}^{\infty} |s(kT + nMT)|, \text{ for } 0 \leq k \leq M - 1 \tag{8.15}$$

$$\tilde{\eta}[k] = \sum_{n=0}^{\infty} \pm\eta(kT + nMT), \text{ for } 0 \leq k \leq M - 1 \tag{8.16}$$

The ±1 factor is set based on whether the sample $s(kT + nMT)$ is positive or negative. It does not alter the variance of $\eta(kT + nMT)$.

Since the samples $\eta(kT)$ are $i.i.d$, the sequence $\tilde{\eta}[k]$ contains independent values. Furthermore, because the Gaussian distribution is symmetric, the ±1 factor should not introduce correlation between $\tilde{s}[k]$ and $\tilde{\eta}[k]$. Therefore, the bias and variance are

$$E_V = T \sum_{k=0}^{M-1} \tilde{s}^2[k] \tag{8.17}$$

$$\sigma_V^2 = T^2 \sum_{k=0}^{M-1} \tilde{s}^2[k] E\left[\tilde{\eta}^2[k]\right]$$

$$= T^2\sigma^2 \sum_{k=0}^{M-1} \tilde{s}^2[k]m_k \tag{8.18}$$

The value m_k represents the number of noise samples summed in each $\tilde{\eta}[k]$. If $s(t)$ is a finite-duration signal, only a finite number of samples $x(kT)$ will be used for the integral in Equation (8.1). In this case Equation (8.18) remains bounded.

The primary advantage of time aliasing is that we can exploit signal energy from all Nyquist samples. The primary disadvantage is that time aliasing increases the noise variance, which may worsen the overall performance

8.2   Bilinear Matched Filtering - A Theoretical Analysis

We now derive expressions for E_V and σ_V^2 when using the bilinear representations. The analysis in this section is based on CT signals and basis functions. The modifications when simulating the matched filter solution in MATLAB will be discussed in Chapter 9.

8.2.1 The Orthonormal Representation

Given the orthonormal expansion coefficients $s[n]$ and $x[n]$, it follows that $\int_0^\infty x(t)s(t)dt = \sum_{n=1}^\infty s[n]x[n]$. In this application we assume that the sequence $s[n]$ has already been computed and stored and that the coefficients $x[n]$ are calculated once the received signal has been obtained.

The first step to computing E_V and σ_V^2 is to express $x[n]$ using the orthonormal basis functions, in the case when $s(t)$ is present

$$
\begin{aligned}
x[n] &= \int x(t)\lambda_n(t)dt = \int \left[s(t) + \eta(t) \right] \lambda_n(t)dt \\
&= s[n] + \int \eta(t)\lambda_n(t)dt
\end{aligned}
\tag{8.19}
$$

By substituting Equation (8.19) for $x[n]$ and by using the orthonormality relationship in Equation (1.4), we have

$$
E_V = \sum_{k=0}^{M-1} s^2[k]
\tag{8.20}
$$

$$
\sigma_V^2 = E\left[\int \eta(t) \left(\sum_{n=1}^\infty s[n]\lambda_n(t) \right) dt \right]^2
$$

$$
= \sigma_\eta^2 \sum_{n=1}^\infty s^2[n]
\tag{8.21}
$$

Since $\sum_{n=1}^\infty s^2[n] = T\sum_{k=0}^\infty s^2(kT)$, in the limit of a perfect signal representation, the bias and variance for the orthonormal and Nyquist representations are equal. This implies that both expansions would yield the same binary detection performance.

8.2.2 The Biorthogonal Representation

Given the biorthogonal expansion coefficients $x[n]$ and the secondary coefficients $b_s[n]$, it follows that $\int_0^\infty x(t)s(t)dt = \sum_{n=0}^\infty x[n]b_s[n]$. Similar to the orthonormal case, we assume that the sequence $b_s[n]$ has already been computed and stored. The coefficients $x[n]$ are calculated once $x(t)$ has been obtained.

Again, we first express $x[n]$ using the biorthogonal basis functions in the case when the desired signal is present.

$$
\begin{aligned}
x[n] &= \int x(t)h_n(t)dt = \int \left[s(t) + \eta(t)\right] h_n(t)dt \\
&= s[n] + \int \eta(t)h_n(t)dt
\end{aligned}
\tag{8.22}
$$

The sequence $s[n]$ represents the biorthogonal expansion coefficients of $s(t)$.

From Equation (8.22), the quantities E_V and σ_V^2 will depend on the dual basis inner products. Since the set $\{h_n(t)\}_{n=0}^{\infty}$ is not orthogonal, we employ the recurrence relationship in Equation (A.4) with $\alpha = 0$:

$$
L_{n-1}^{(1)}(x) = \frac{n}{x} \left[L_{n-1}(x) - L_n(x)\right]
\tag{8.23}
$$

The dual basis functions (for $n \geq 0$) can now be expressed

$$
h_n(t) =
\begin{cases}
e^{-at} L_0(2at), & n = 0 \\
(-1)^{n-1} e^{-at} \left[L_{n-1}(2at) - L_n(2at)\right] u(t), & n > 0
\end{cases}
\tag{8.24}
$$

By substituting $x = 2at$ and applying the orthogonality relationship of Laguerre polynomials from Equation (A.3), the inner product of two dual basis functions is given by

$$
\int_0^\infty h_n(t)h_m(t)dt =
\begin{cases}
\frac{1}{2a}, & \text{for } m = n = 0 \\
\frac{1}{a}, & \text{for } m = n \neq 0 \\
\frac{1}{2a}, & \text{for } n = m+1 \text{ or } m = n+1, \, n, m \neq 0 \\
0, & \text{otherwise}
\end{cases}
\tag{8.25}
$$

If we replace $x[n]$ using Equation (8.22) and apply the inner products from Equation (8.25), the bias and variance are

$$
E_V = \sum_{n=0}^{\infty} s[n]b_s[n]
\tag{8.26}
$$

93

$$\sigma_V^2 = E\left[\int \eta(t)\left(\sum_{n=0}^{\infty} b_s[n]h_n(t)\right)dt\right]^2$$

$$= \sigma_\eta^2\left[\frac{1}{2a}b_s^2[0] + \frac{1}{a}\sum_{n=1}^{\infty}b_s^2[n] + \frac{1}{a}\sum_{n=0}^{\infty}b_s[n]b_s[n+1]\right] \tag{8.27}$$

Note that $\sum_{n=0}^{\infty} s[n]b_s[n]$ is the energy of the signal $s(t)$. Furthermore, since $s(t)$ can be expressed using the dual basis as $s(t) = \sum_{n=0}^{\infty} b_s[n]h_n(t)$, the bracketed term in Equation (8.27) is also equal to the desired signal energy. Therefore, in the limit of a perfect signal representation, the detection performance of the Nyquist, orthonormal and biorthogonal representations are equivalent.

8.2.3 Variations of the Bilinear Representations

If we constrain the number of digital multiplies, it will not in general be possible to use complete expansions for the signals $x(t)$ and $s(t)$. In this application we rely on the windowed bilinear representations and employ the Linear, Nonlinear 1 and Nonlinear 2 techniques (discussed in Section 6.3) to reduce the total number of DT coefficients.

The expressions for E_V and σ_V^2 are very similar to the ones already derived. Partial biases and variances are calculated by summing over the retained indices in each segment. Furthermore, since we use a non-overlapping rectangular window, the final E_V and σ_V^2 are obtained by summing these partial values over all segments.

Chapter 9

Matched Filtering Simulations

This chapter presents MATLAB simulation results of binary detection as described in Chapter 8. Specifically, we compare the detection performances when using the Nyquist, the orthonormal and the biorthogonal representations to compute the integral $\int x(t)s(t)dt$.

Section 9.1 of this chapter outlines the experimental details. In Section 9.2 we display a series of Receiver Operating Characteristic curves for different desired signals $s(t)$. A short discussion of the results is found in Section 9.3.

9.1   Details of the Simulation Setup

We assume that all signals have been sampled at a rate approximately 100 times greater than the Nyquist rate of $s(t)$. To simulate discrete-time AWGN, $i.i.d.$ noise with a distribution $N(0, \sigma_\eta^2/T)$ is added to each sample of the transmitted signal to form the received sequence $x(nT)$. This ensures that the additive channel noise is white over the frequency range of interest. Representative signal and noise spectra are shown in Figure (9-1).
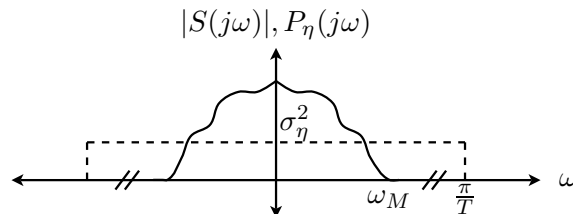
Figure 9-1: Magnitude of $S(j\omega)$ and Noise Power Spectrum with Sample Spacing T.

Since the bilinear expansions do not have an associated 'sampling rate', we look at the detection performance of each representation for a fixed number of discrete-time multiplies. This is equivalent to constraining the number of coefficients used to calculate $\int x(t)s(t)dt$.

For the Nyquist representation, the reduced set of time samples are obtained directly from the oversampled sequences $s(nT)$ and $x(nT)$ via two different methods. First, we select the subset of samples corresponding to the largest magnitudes in $s(nT)$. Second, we time-alias the sequences. In this case, each sample is multiplied by ± 1 according to the sign of the corresponding sample in $s(nT)$.

For the bilinear representations, the sequences are first segmented using a non-overlapping rectangular window. The necessary coefficients are then computed according to Section 4.1. In this application we use the Linear, Nonlinear 1 and Nonlinear 2 techniques from Section 6.3 to reduce the total number of DT coefficients. The indices are retained based on the (largest) orthonormal expansion coefficients and the (largest) biorthogonal inner product coefficients of the windowed $s(t)$. The same index set is used for both the desired and received signals.

In this chapter we compare the detection performances for the four desired signals:

$$
\begin{aligned}
s_1(t) \ &\sim \ t^2 e^{-150t} u(t) \\[2mm]
s_2(t) \ &\sim \ \begin{cases} \sin(100t), & 0 \le t < 1 \\ 0, & \text{otherwise} \end{cases} \\[2mm]
s_3(t) \ &\sim \ \begin{cases} sinc(100(t-0.5)), & 0 \le t < 1 \\ 0, & \text{otherwise} \end{cases} \\[2mm]
s_4(t) \ &\sim \ \begin{cases} 1, & 0 \le t < 0.1 \\ 0, & \text{otherwise} \end{cases}
\end{aligned}
$$

Once again, all signals are normalized to have unit energy.

The signal $s_1(t)$ has a rational Laplace transform and should be well-approximated using the bilinear basis functions. $s_2(t)$ is narrow-band in frequency with a constant energy distribution over time, while $s_3(t)$ has a wider frequency range and its energy concentrated around the main lobe. Finally, $s_4(t)$ is a short-duration signal with isolated discontinuities at $t = 0, 0.1$.

9.2 Simulation Results

We assess the binary detection performance by examining Receiver Operating Characteristic (ROC) curves. In Figures (9-2)-(9-5) the probability of detection, P_d, is plotted on the vertical axis, and the probability of false alarm, P_{fa}, is plotted on the horizontal axis. Since we desire a large P_d for a given P_{fa}, we would like the curves to lie near the upper-left corner of the graph. Consequently, an ROC curve which lies entirely above another has better performance.

The results presented in this section are based on the theoretical expressions derived in Chapter 8. A separate set of Monte Carlo experiments were done for each representation and approximation technique. In all cases, the Monte Carlo simulations converged to the theoretical performance as the number of trials increased.

Figures (9-2)-(9-5) depict ROC curves for a fixed number of DT multiplies. Throughout this section we assume that H_0 and H_1 are equally likely, and that the channel noise power is $\sigma_\eta^2 = 1$. The acronyms SLS and PA stand for 'Select Largest Samples' and 'Positive Aliased'. They denote the two Nyquist coefficient-reduction techniques. Each individual plot in Figures (9-2)-(9-5) compares the two Nyquist methods with a different bilinear approximation (Linear, Nonlinear 1 or Nonlinear 2).

Figures (9-2) and (9-5) present the ROC curves for the desired signals $s_1(t)$ and $s_4(t)$, respectively. In both cases the signal duration is artificially truncated to $t_{max} = 1$, and the integrals $\int x(t)s_{1,4}(t)dt$ are approximated using 5 DT multiplies. In this case the signals are not segmented, meaning that the Nonlinear 1 and Nonlinear 2 methods yield identical results. We use values of $a = 100$ and $a = 62.8$ to compute the bilinear coefficients for the two detection systems.

Figures (9-3) and (9-4) illustrate the ROC curves for the desired signals $s_2(t)$ and $s_3(t)$, respectively. In each case, the signal is segmented with a rectangular window of length $0.34sec$, and the inner products are computed using a total of 25 DT multiplies. Additionally, the bilinear expansions are obtained using a value of $a = 100$.
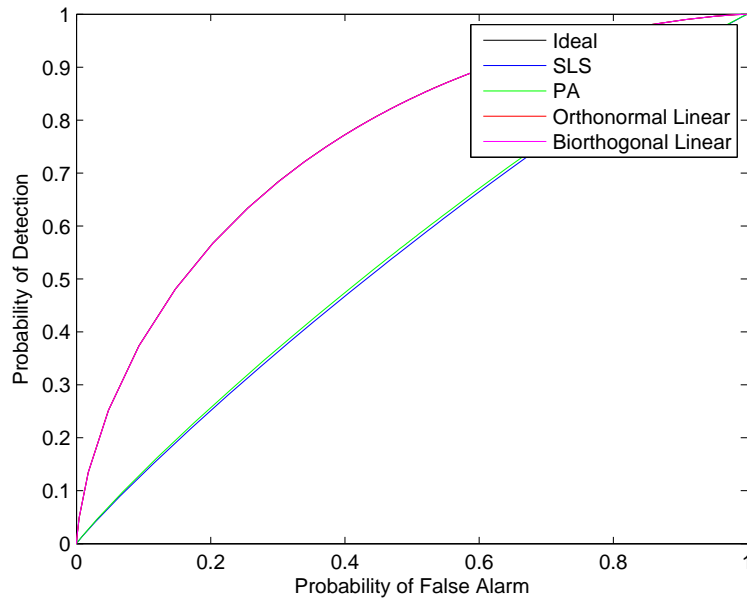
(a) Linear Approximation
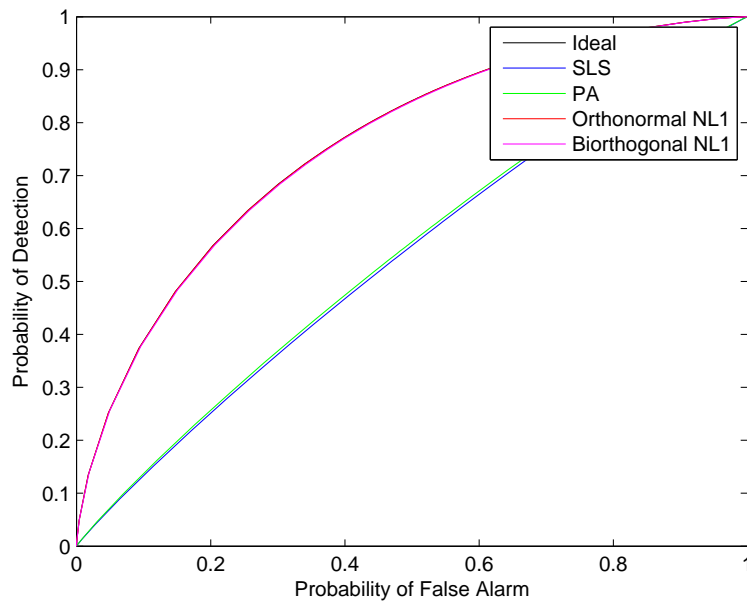
(b) Nonlinear 1 Approximation

Figure 9-2: ROC Curves for $s_1(t)$; 5 DT Multiplies, $a = 100$
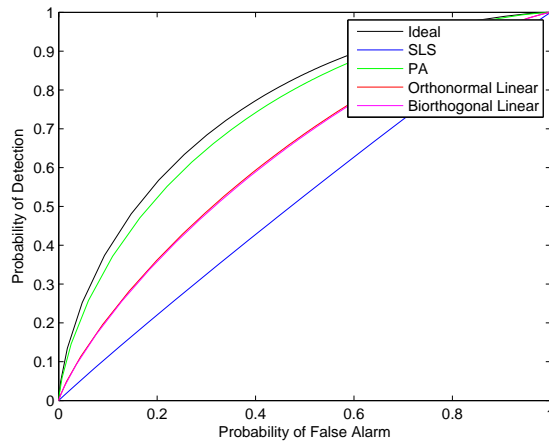
(a) Linear Approximation
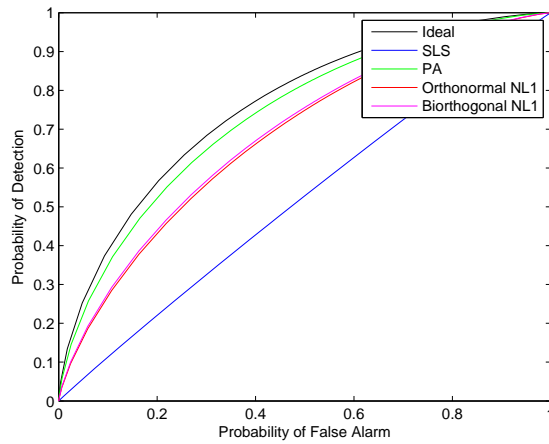
(b) Nonlinear 1 Approximation
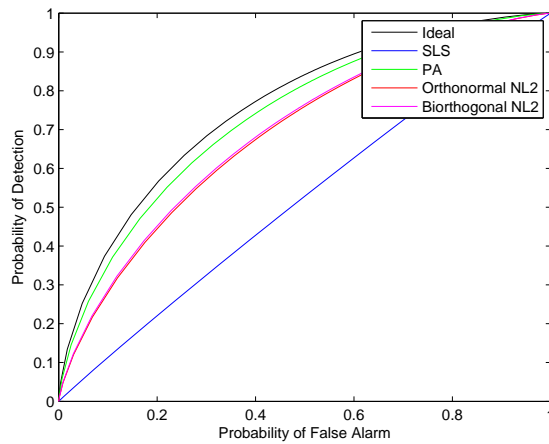
(c) Nonlinear 2 Approximation

Figure 9-3: ROC Curves for $s_2(t)$; 25 DT Multiplies, $a = 100$
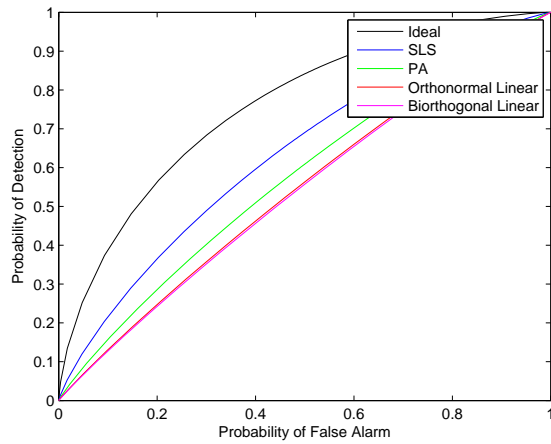
(a) Linear Approximation
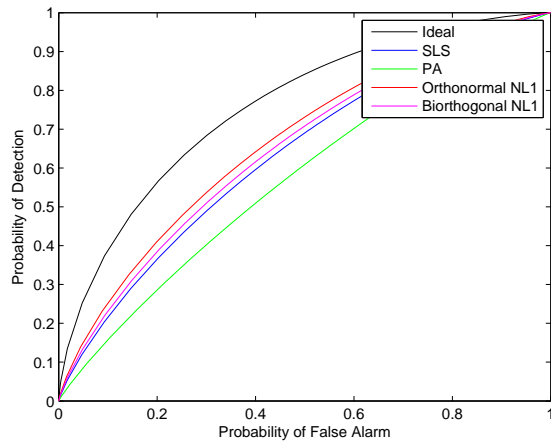
(b) Nonlinear 1 Approximation
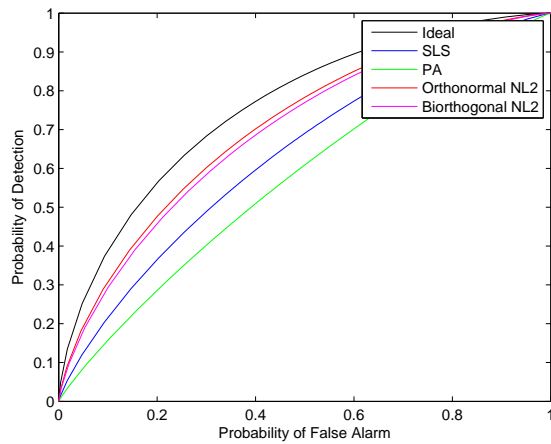
(c) Nonlinear 2 Approximation

Figure 9-4: ROC Curves for $s_3(t)$; 25 DT Multiplies, $a = 100$
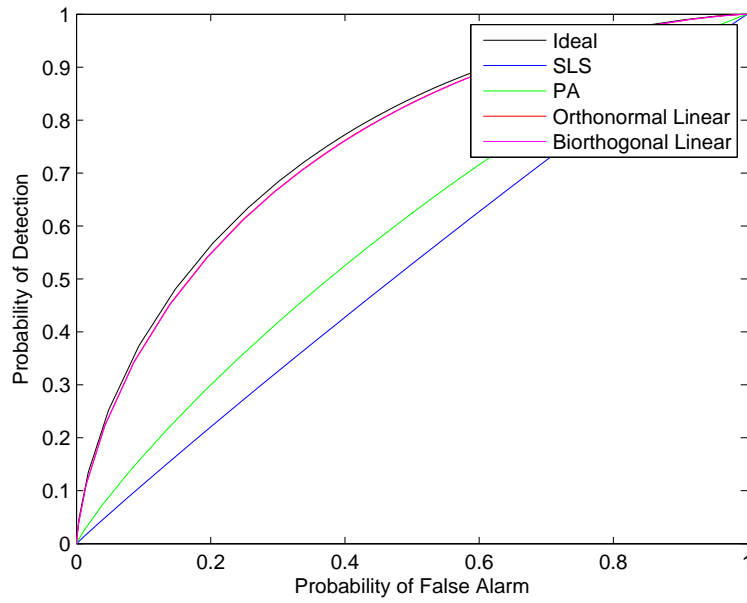
(a) Linear Approximation
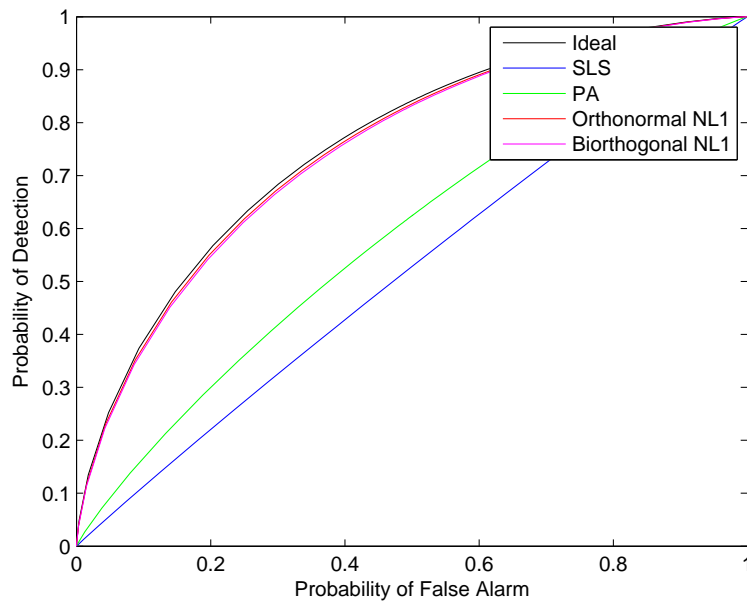
(b) Nonlinear 1 Approximation

Figure 9-5: ROC Curves for $s_4(t)$; 5 DT Multiplies, $a = 62.8$

9.3   Discussion

The bilinear ROC curves in Figures (9-2)-(9-5) conform to the intuition gained from Chapters 5 and 6. Specifically, the bilinear representations can well-approximate the integral $\int x(t)s(t)dt$ for signals with rational Laplace transforms, such as $s_1(t)$, and for short-duration signals with energy concentrated near the time origin, such as $s_4(t)$. In both examples, the performance is close to ideal when using only 5 DT multiplies.

In contrast, the bilinear representations do not perform as well when the desired signal is $s_2(t)$ in part because the sinusoidal pulse has its energy distributed evenly throughout the signal duration. The bilinear detection is even worse for $s_3(t)$ quite likely because the *sinc* pulse has its energy concentrated around $t = 0.5$ rather than at the origin. In these cases, the bilinear performance is not ideal, even when using 25 DT multiplies to compute the inner products.

Aside from distinguishing the well-approximated signals from the poorly-approximated ones, the plots in Section 9.2 reveal other trends. For example, there is a dramatic difference between the linear and nonlinear ROC curves in Figures (9-3) and (9-4). This indicates that being able to select the largest coefficients is very important when approximating the inner product. Also, the orthonormal and biorthogonal performance is very similar in all cases. This is consistent with the results of previous chapters. One more important point is that there is very little difference between the Nonlinear 1 and Nonlinear 2 curves for the sinusoidal pulse. This is because each segment of the windowed signal is almost identical.

The Nyquist SLS and PA methods behave very differently than the bilinear approximations.

SLS does well when the signal energy is concentrated in a small region and can be captured using a few samples. This is true of the pulse $s_3(t)$. Although the nonlinear approximations perform better than SLS in Figure (9-4), as the number of DT multiplies increases, the SLS performance improves very rapidly and approaches the ideal case ahead of the bilinear representations.

PA performs well when the signal energy is spread evenly over time, like the sinusoidal pulse $s_2(t)$. In this case, both the magnitude and the noise variance of the aliased samples increase linearly. This can be seen from Equations (8.15) and (8.16). The PA method does not perform well for rapidly-decaying signals because the magnitude of the aliased samples grows more slowly than the noise variance.

The ROC curves based on synthetic signals $s_1(t)$-$s_4(t)$ indicate that using the bilinear representations may be appropriate in certain binary detection scenarios. In three out of the four cases, the Nonlinear 1 and Nonlinear 2 performances exceed those of the two Nyquist methods. Furthermore, in applications where the desired signal $s(t)$ is not appropriately band-limited, the bilinear representations may provide a favorable alternative to eliminating signal content through an anti-aliasing filter.

On the other hand, if there is a constraint on the number of filter stages in the first-order analysis cascades (i.e. a constraint on the analog hardware), the bilinear representations may not be a good choice. This is because linear approximation performs much worse than the Nyquist methods for both the sinusoidal and the *sinc* pulses.

Appendix A

The Family of Generalized Laguerre Polynomials

Many properties of the two bilinear representations are derived from those of the generalized Laguerre polynomials, $L_n^{(\alpha)}(x)$. Therefore, this appendix provides a brief overview of these functions and their properties. For a more detailed treatment of Laguerre polynomials, refer to [5], [13] and [3].

A.1   Definition

The generalized Laguerre polynomials, $L_n^{(\alpha)}(x)$, are characterized by two parameters, the index, n, and the order value, α. They are defined according to the expression

$$L_n^{(\alpha)}(x) = \frac{e^x x^{-\alpha}}{n!} \frac{d^n}{dx^n}(e^{-x} x^{n+\alpha}) \tag{A.1}$$

Observe that the multiplicative term in Equation (A.1) cancels the factors of e^x and x^α in the derivative term. Consequently, the resulting function is simply a polynomial in x.

By using the product rule of differentiation, Equation (A.1) can be expanded into an $(n+1)$-term polynomial as shown below

$$L_n^{(\alpha)}(x) = \sum_{j=0}^{n} \frac{\Gamma(n+\alpha+1)}{\Gamma(n-j+1)\Gamma(j+\alpha+1)} \frac{(-x)^j}{j!} \tag{A.2}$$

Plots of the generalized Laguerre polynomials are shown in Figures (A-1) and (A-2).
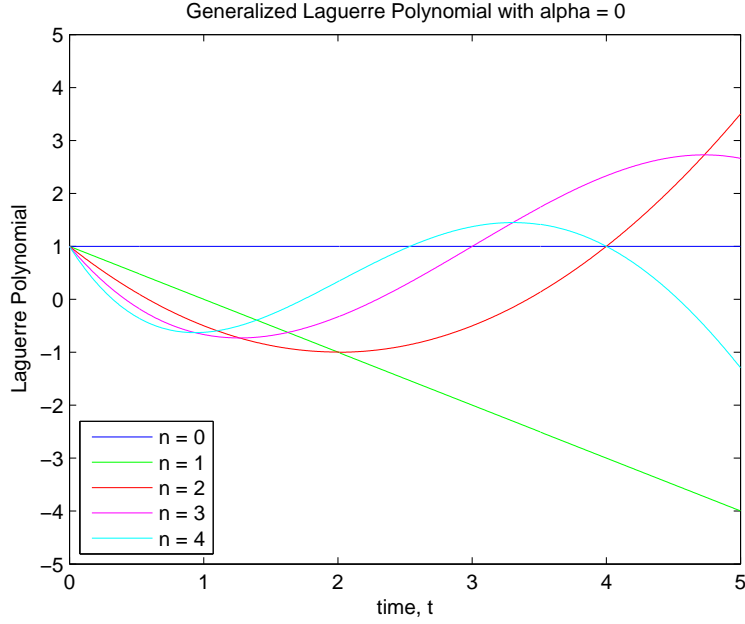
Figure A-1: $L_n^{(\alpha)}(x)$ for different index values using $\alpha = 0$

A.2   Properties

Below we describe some well-known properties of Laguerre polynomials. These are used extensively when deriving the bilinear representation properties in Chapter 3.

A.2.1   Orthogonality

For a given order value, α, the generalized Laguerre polynomials are orthogonal with respect to the weighting function $x^\alpha e^{-x}$. Mathematically

$$\int_0^\infty L_n^{(\alpha)}(x) L_m^{(\alpha)}(x) x^\alpha e^{-x} dx = \begin{cases} \frac{\Gamma(n+\alpha+1)}{\Gamma(n+1)}, & n = m \\ 0, & \text{otherwise} \end{cases} \tag{A.3}$$

Equation (A.3) can be used to verify that the basis functions $\lambda_n(t)$ are, indeed, orthonormal, and that the primal basis functions, $\phi_n(t)$, satisfy Equation (2.10).
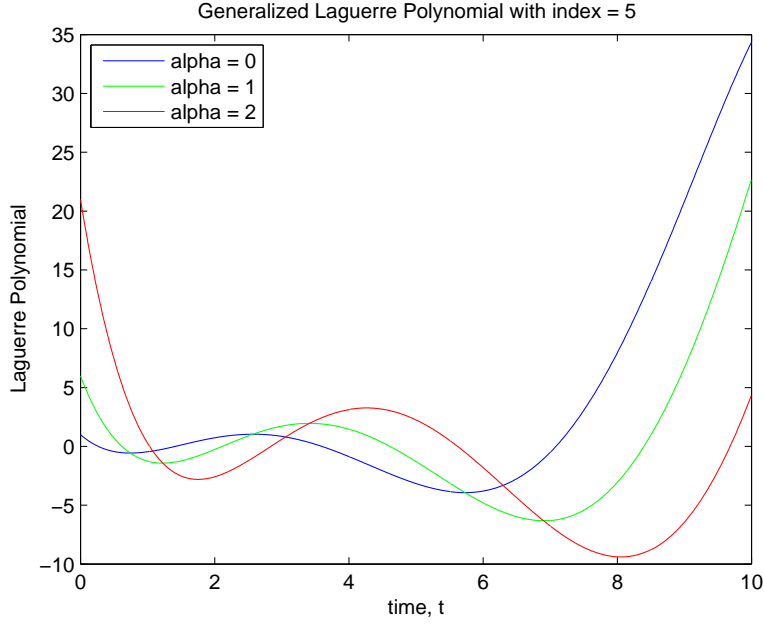
Figure A-2: $L_n^{(\alpha)}(x)$ for different values of a using $n = 5$

A.2.2 Recurrence Relation

Differentiating Equation (A.2) with respect to x yields the following recurrence relation between $L_n^{(\alpha)}(x)$ and its first derivative:

$$\frac{d}{dx}L_n^{(\alpha)}(x) = -L_{n-1}^{(\alpha+1)}(x) = \frac{1}{x}\left[nL_n^{(\alpha)}(x) - (n+\alpha)L_{n-1}^{(\alpha)}(x)\right] \qquad (A.4)$$

Equation (A.4) is important for analyzing the biorthogonal matched filtering network.

A.2.3 Signal Space

In [5] it is shown that the set of generalized Laguerre polynomials $\{L_n^{(\alpha)}(x)\}_{n=0}^{\infty}$ forms a basis for causal functions, $f(x) = 0$ for $x < 0$, which satisfy the following condition:

$$\int_0^{\infty} |f(x)|^2 x^{\alpha} e^{-x} dx < \infty \qquad (A.5)$$

Equation (A.5) is used when characterizing the span of the primal biorthogonal basis functions, $\phi_n(t)$ in Chapter 3.

A.2.4 Bounds on the Generalized Laguerre Polynomials

Define the normalized Laguerre polynomial as

$$\zeta_n^{(\alpha)}(x) = \left(\frac{\Gamma(n+1)}{\Gamma(n+\alpha+1)} \right)^{1/2} e^{-x/2} x^{\alpha/2} L_n^{(\alpha)}(x) u(x) \tag{A.6}$$

If $C, \gamma > 0$ are constants and we let $\nu = 4n + 2\alpha + 2$, then according to [13], the function $\zeta_n^{(\alpha)}(x)$ is bounded as follows:

$$|\zeta_n^{(\alpha)}(x)| \leq C \begin{cases} (x\nu)^{\alpha/2}, & 0 \leq x \leq 1/\nu \\ (x\nu)^{-1/4}, & 1/\nu \leq x \leq \nu/2 \\ \nu^{-1/4} \left(\nu^{1/3} + |\nu - x| \right)^{-1/4}, & \nu/2 \leq x \leq 3\nu/2 \\ e^{-\gamma x}, & x \geq 3\nu/2 \end{cases} \tag{A.7}$$

Equation (A.7) is used to derive bounds on the functions $\lambda_n(t)$, $\phi_n(t)$ and $h_n(t)$. These bounds are, in turn, useful when analyzing the approximation properties of the two bilinear representations.

Appendix B

Additional Properties of the Bilinear Representations

B.1 Representing Anti-causal Signals

In this thesis, we have represented only causal continuous-time signals which satisfy $f(t) = 0$, $\forall t < 0$. While this does not impede our investigation of the bilinear approximation properties, from a theoretical perspective, it is worthwhile to consider how we may represent anti-causal CT signals as well.

From Equations (2.4) and (2.9) we note that $\lambda_n(t)$, $\phi_n(t)$ and $h_n(t)$ are zero for $t > 0$ or $t < 0$ depending on the index value, n. Therefore, we can divide a two-sided signal into its causal and its anti-causal parts and compute the bilinear expansions of each one separately.

In this section we derive both the orthonormal and the biorthogonal analysis and synthesis networks for bounded anti-causal CT signals, $f(t)$.

B.1.1 The Orthonormal Representation

From Equation (2.4) if $f(t) = 0$ $\forall t > 0$ the only basis functions with indices $n \leq 0$ will contribute to the expansion. By inspection, the analysis and synthesis networks for anti-causal inputs are described by the first-order cascades in Figures (B-1) and (B-2).
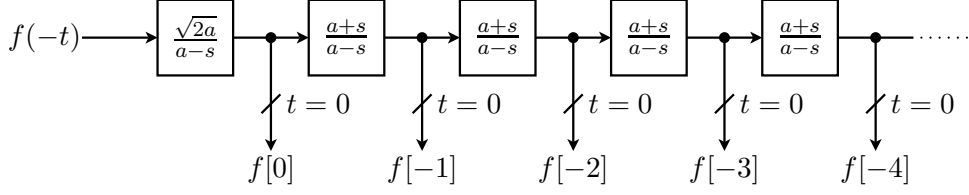
Figure B-1: Orthonormal analysis network for anti-causal CT signals.
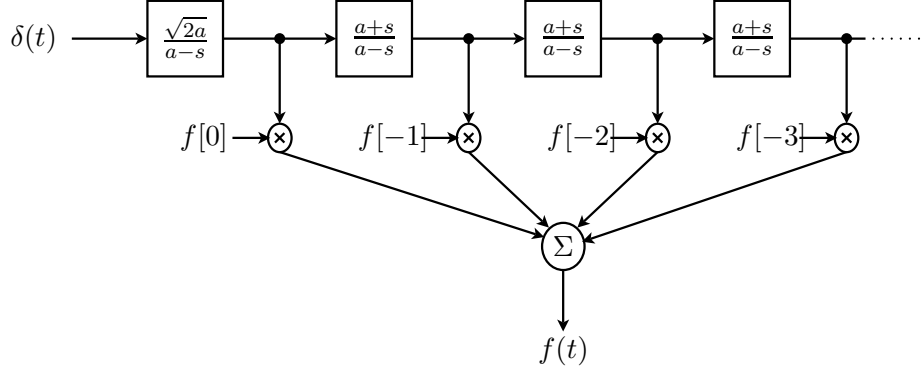
Figure B-2: Orthonormal synthesis network for anti-causal CT signals.

B.1.2 The Biorthogonal Representation

Recall from Equation (2.9) that for anti-causal signals, only primal basis functions with index $n \leq 0$ contribute to the overall expansion.

As seen in Chapter 2, the dual basis functions for $n \neq 0$ are given by $h_n(t) = \frac{1}{n}t\phi_n(t)$. In the Laplace transform domain, this corresponds to

$$H_n(s) = -\frac{d}{ds}\Phi_n(s) = \frac{2a}{(a-s)^2}\left(\frac{a+s}{a-s}\right)^{-n-1} \tag{B.1}$$

The final step is to find $H_0(s)$ by constraining $f(t)$ to remain bounded for all time. Since the primal basis functions $\phi_n(t)$ have an impulse at the origin, the expansion coefficients must satisfy

$$f[0] = -\sum_{n=-\infty}^{-1} f[n] \tag{B.2}$$

By expressing the expansion coefficients $f[n]$ as an inner product in the Laplace transform domain and by substituting Equation (B.1) into Equation (B.2), it follows that

$$H_0(s) = \frac{1}{a-s} \tag{B.3}$$

110

Using the above expressions for $\Phi_n(s)$ and $H_n(s)$, the analysis and the synthesis networks first-order cascades for anti-causal inputs are depicted in Figures (B-3) and (B-4).
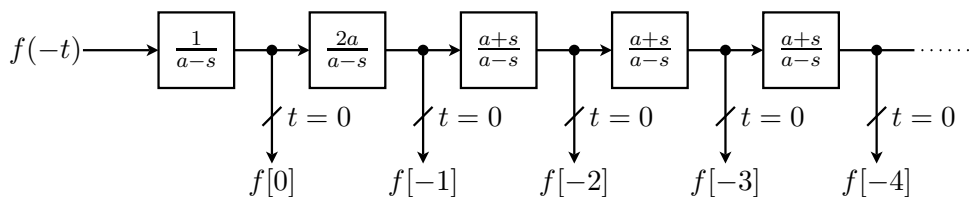
Figure B-3: Biorthogonal analysis network for anti-causal CT signals.
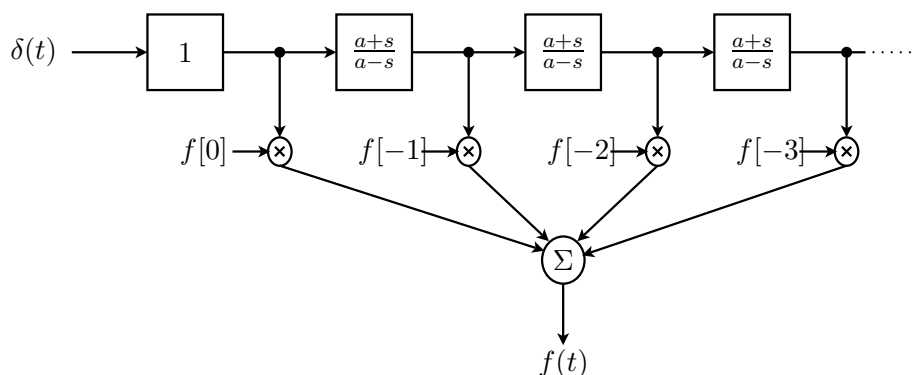

Figure B-4: Biorthogonal synthesis network for anti-causal CT signals.

B.2   Conditions to Preserve Correlation

In [8] the authors derive necessary and sufficient conditions to map a continuous-time LTI system onto a discrete-time LSI system. This is equivalent to preserving convolution between the CT and DT domains. Below, we follow a similar approach and derive the necessary conditions to preserve *correlation* between continuous and discrete time. This property may be useful in certain applications.

Let $f(t) = \sum_{n \in Z} f[n]\psi_n(t)$ and let $g(t)$ and $h(t)$ be defined in a similar fashion. We seek conditions on the basis functions $\{\psi_n(t)\}_{n \in Z}$ so that

$$g(t) = \int f(\tau)h(\tau - t)dt \;\longleftrightarrow\; g[n] = \sum_{k \in Z} f[k]h[k-n] \qquad (\text{B.4})$$

Since $F(s) = \sum_{n \in Z} f[n]\Psi_n(s)$ and $H(-s) = \sum_{n \in Z} h[n]\Psi_n(-s)$, we express the Laplace transform of $g(t)$ in Equation (B.4) as

$$
\begin{aligned}
\sum_{n \in Z} g[n]\Psi_n(s) &= \left(\sum_{k \in Z} f[k]\Psi_k(s)\right)\left(\sum_{r \in Z} h[r]\Psi_r(-s)\right) \\
&= \sum_{k \in Z}\sum_{r \in Z} f[k]h[r]\Psi_k(s)\Psi_r(-s) \\
&= \sum_{k \in Z}\sum_{n \in Z} f[k]h[k-n]\Psi_k(s)\Psi_{k-n}(-s) \quad\quad \text{(B.5)}
\end{aligned}
$$

It follows that $\Psi_n(s)$ must satisfy Equation (B.6) below in order for the expansion to preserve correlation.

$$
\Psi_n(s) = \Psi_k(s)\Psi_{k-n}(-s) \quad\quad\quad \text{(B.6)}
$$

Notice that if $\Psi_n(s) = \Psi_{-n}(-s)$, then the expansion also preserves convolution.

Since the primal basis functions $\Phi_n(s) = \left(\frac{a-s}{a+s}\right)^n$ satisfies the above criterion, the biorthogonal representation preserves correlation as well as convolution between continuous and discrete time.

B.3   Noise Analysis for the Analysis and Synthesis Networks

The presence of noise is inevitable in any real-world system implementation. In this section, we present simple noise models for the bilinear analysis and synthesis networks.

We consider two types of noise. The first is additive noise at the input to the first-order cascade, $\eta(t)$. The second is additive noise introduced by the analog components, $\varepsilon(t)$. We assume that component noise is added after each non-unity gain factor in each stage, and that it is uncorrelated with all other noise sources.

Since, the first-order cascades consist only of low-pass and all-pass filters, we examine separately the effect of input and component noise on each type of filter.

B.3.1   The Low-pass Filter Stage

An implementation for a low-pass filter stage with system function $H(s) = \frac{A}{a+s}$ is depicted in Figure (B-5). The block with transfer function $\frac{1}{s}$ corresponds to an integrator.
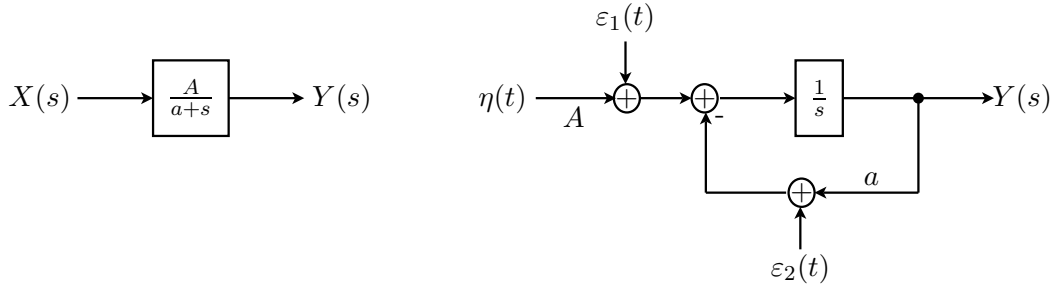
Figure B-5: Block and Implementation Diagram for the Low-pass Filter Stage.

The transfer function for the additive input noise, $\eta(t)$, is $H_\eta(s) = H(s) = \frac{A}{a+s}$. Assuming that the noise has a power spectrum $P_\eta(j\omega)$, the output power spectrum is

$$P_{y,\eta}(j\omega) = P_\eta(j\omega)|H_\eta(j\omega)|^2 = P_\eta(j\omega)\left(\frac{A^2}{a^2+\omega^2}\right) \tag{B.7}$$

As seen in Figure (B-5) there are two component noise sources in the low-pass filter stage. The noise $\varepsilon_1(t)$ arises from the gain A in the numerator of $H(s)$ and the noise $\varepsilon_2(t)$ comes from the constant a in the denominator of $H(s)$. Using the low-pass filter implementation diagram, we can derive the following noise-to-output transfer functions:

$$H_{\varepsilon_1}(s) = \frac{1}{a+s} \tag{B.8}$$

$$H_{\varepsilon_2}(s) = \frac{-1}{a+s} \tag{B.9}$$

Notice that both transfer functions are low-pass filters.

Assuming that the noise sources have power spectra $P_{\varepsilon_1}(j\omega)$ and $P_{\varepsilon_2}(j\omega)$, the output power spectra can be expressed

$$P_{y,\varepsilon_1}(j\omega) = P_{\varepsilon_1}(j\omega)\left(\frac{1}{a^2+\omega^2}\right) \tag{B.10}$$

$$P_{y,\varepsilon_2}(j\omega) = P_{\varepsilon_2}(j\omega)\left(\frac{1}{a^2+\omega^2}\right) \tag{B.11}$$

If either constant in Figure (B-5) is ± 1, then the corresponding noise source is zero. This is because unity gain is equivalent to a wire, which we assume to be noiseless.

B.3.2 The All-pass Filter Stage

An implementation for an all-pass filter stage with system function $H(s) = \frac{a-s}{a+s}$ is depicted in Figure (B-6).
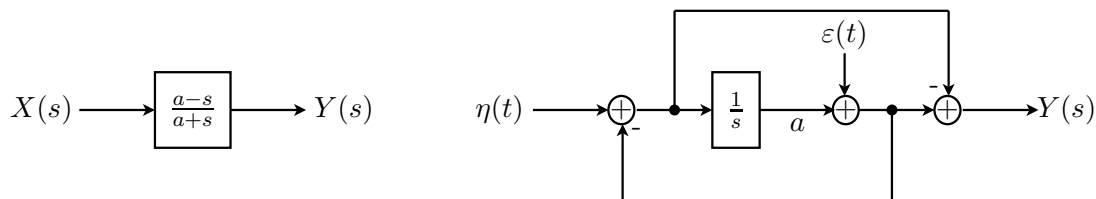

Figure B-6: Block and Implementation Diagram for the All-pass Filter Stage.

Once again, the transfer function for the additive input noise is given by $H_\eta(s) = H(s) = \frac{a-s}{a+s}$. In this case, the output power spectrum is

$$P_{y,\eta}(j\omega) = P_\eta(j\omega)|H_\eta(j\omega)|^2 = P_\eta(j\omega) \tag{B.12}$$

Thus, the noise spectrum remains unchanged by the all-pass filter stage.

From Figure (B-6), the constants a in the numerator and denominator of $H(s)$ can be combined into a single gain element. Therefore, the all-pass filter only has one component noise source. Using the implementation diagram, we can derive the following transfer function for the component noise source $\varepsilon(t)$:

$$H_\varepsilon(s) = \frac{2s}{s+a} \tag{B.13}$$

with output power spectrum

$$P_{y,\varepsilon}(j\omega) = P_\varepsilon(j\omega)\left(\frac{4\omega^2}{a^2+\omega^2}\right) \tag{B.14}$$

Equation (B.14) corresponds to a high-pass filter. Since the transfer function $H_\varepsilon(s)$ eliminates low-frequency noise, this may be beneficial should the CT input signal be low-pass in nature.

B.3.3 Combined Effect of Input and Component Noise

When analyzing the combined effects of input and component noise, we assume that the additive input noise is white with variance σ_η^2 and that each component noise source is white with variance σ_ε^2. The output power spectrum after the nth stage is denoted by $P_{y,n}(j\omega)$.

The Orthonormal Networks

The orthonormal cascade consists of one low-pass filter followed by a succession of all-pass filters. The output power spectrum after the low-pass filter is

$$P_{y,1}(j\omega) = \left(\frac{2a}{a^2 + \omega^2} \right) \sigma_\eta^2 + 2 \left(\frac{1}{a^2 + \omega^2} \right) \sigma_\varepsilon^2 \tag{B.15}$$

At each subsequent stage, additional coefficient noise is added according to Equation (B.14), however noise present at the input to a stage is not modified by an all-pass filter. Therefore, the output power spectra for $n > 1$ is

$$P_{y,n}(j\omega) = \left(\frac{2a}{a^2 + \omega^2} \right) \sigma_\eta^2 + 2 \left(\frac{1}{a^2 + \omega^2} \right) \sigma_\varepsilon^2 + (n - 1) \left(\frac{4\omega^2}{a^2 + \omega^2} \right) \sigma_\varepsilon^2 \tag{B.16}$$

The Biorthogonal Analysis Network

The biorthogonal analysis network consists of two low-pass filter stages followed by a cascade of all-pass filters. The output power spectrum after the first low-pass filter is

$$P_{y,1}(j\omega) = \left(\frac{1}{a^2 + \omega^2} \right) \sigma_\eta^2 + \left(\frac{1}{a^2 + \omega^2} \right) \sigma_\varepsilon^2 \tag{B.17}$$

Notice that since there is only one non-unity coefficient, there is only one component noise source. After the second low-pass filter, two coefficient noise sources are added and the noise from the previous stage is modified. The output power spectrum becomes

$$P_{y,2}(j\omega) = \left(\frac{4a^2}{(a^2 + \omega^2)^2} \right) \sigma_\eta^2 + \left(\frac{4a^2}{(a^2 + \omega^2)^2} \right) \sigma_\varepsilon^2 + 2 \left(\frac{1}{a^2 + \omega^2} \right) \sigma_\varepsilon^2 \tag{B.18}$$

Finally, the all-pass filters add coefficient noise sources but do not modify noise present at the input. The output power spectra for $n > 2$ is

$$P_{y,n}(j\omega) = \left(\frac{4a^2}{(a^2 + \omega^2)^2} \right) \sigma_\eta^2 + \left(\frac{4a^2}{(a^2 + \omega^2)^2} \right) \sigma_\varepsilon^2 + \left(\frac{2 + 4(n - 2)\omega^2}{a^2 + \omega^2} \right) \sigma_\varepsilon^2 \tag{B.19}$$

The Biorthogonal Synthesis Network

The biorthogonal synthesis network consists only of all-pass filters. This means that each stage adds a coefficient noise source but does not modify existing noise at the input. The output power spectra (for all) n is

$$P_{y,n}(j\omega) = \sigma_\eta^2 + n\left(\frac{4\omega^2}{a^2 + \omega^2}\right)\sigma_\varepsilon^2 \qquad \text{(B.20)}$$

From the above analysis we recognize that although increasing the number of stages in the cascade allows for a more accurate signal representation, we suffer performance degradation with the addition of a linearly-increasing number of noise sources.

Bibliography

[1] E. W. Cheney. *Introduction to Approximation Theory*. McGraw-Hill, New York, 1966.

[2] Ole Christensen and Khadija L. Christensen. *Approximation Theory: From Taylor Polynomials to Wavelets*. Birkhauser, Boston, 2004.

[3] E. H. Doha. On the connection coefficients and recurrence relations arising from expansions in series of laguerre polynomials. *Journal of Physics A: Mathematical and General*, pages 5449–5462, 2003.

[4] Robert G. Gallager. 6.450: Principles of digital communication, August 23, 2006.

[5] Allan M. Krall. *Hilbert Space Boundary Value Problems and Orthogonal Polynomials*. Birkhauser Verlag, Basel, 2002.

[6] Y. W. Lee. *Statistical Theory of Communication*. John Wiley and Sons, New York, 1960.

[7] S. G. Mallat. *A Wavelet Tour of Signal Processing*. Academic Press, 1999.

[8] Alan V. Oppenheim and Donald H. Johnson. Discrete representation of signals. *Proc. of the IEEE*, 60(3):681–691, 1972.

[9] Alan V. Oppenheim, Ronald W. Schafer, and John R. Buck. *Discrete-Time Signal Processing*. Prentice Hall, Upper Saddle River, 1999.

[10] Alan V. Oppenheim and George C. Verghese. Signals, systems and inference, 2006.

[11] Alan V. Oppenheim and Alan S. Willsky with S. Hamid Nawab. *Signals and Systems*. Prentice Hall Signal Processing Series, Upper Saddle River, 1997.

[12] Kenneth Steiglitz. *The General Theory of Digital Filters with Applications to Spectral Analysis.* PhD thesis, New York University, 1963.

[13] Sundaram Thangavelu. *Lectures on Hermite and Laguerre Expansions.* Princeton University Press, 1993.

[14] George L. Turin. An introduction to matched filters. *IRE Transactions on Information Theory*, pages 311–329, 1960.

[15] Martin Vetterli. Wavelets, approximation and compression. *IEEE Signal Processing Magazine*, pages 53–73, 2001.